ORNL/TM-2022/1839

Oxidation Behavior and Property Degradation of Nuclear Graphites

Cristian I. Contescu
Ryan M. Paul

March 2022

OAK RIDGE National Laboratory

ORNL IS MANAGED BY UT-BATTELLE LLC FOR THE US DEPARTMENT OF ENERGY

ORNL/TM-2022/1839

Qualification Level Irradiation Program
Department of Energy (DOE) Field Work Proposal RC Reactor Concepts
RES/DEV/DEMO Program (NERC124)

OXIDATION BEHAVIOR AND PROPERTY DEGRADATION OF NUCLEAR GRAPHITES

Cristian I. Contescu
Ryan M. Paul

March 2022

Prepared by
OAK RIDGE NATIONAL LABORATORY
Oak Ridge, TN 37831-6283
managed by
UT-BATTELLE LLC
for the
US DEPARTMENT OF ENERGY
under contract DE-AC05-00OR22725

CONTENTS

LIST OF FIGURES

LIST OF TABLES

ABBREVIATIONS

AE	anticipated event
AGR	advanced gas reactor
ASA	active surface area
ASTM	American Society for Testing and Materials
BDBE	beyond design-based event
BET	Brunauer-Emmett-Teller
BLH	Boltzmann-enhanced Langmuir-Hinshelwood
BLMR	boundary-layer mass rate
BPA	basal plane area
CFD	computational fluid dynamics
CTE	coefficient of thermal expansion
DBE	design-based event
DLOFC	depressurized loss of forced cooling
dpa	displacements per atom
EGCR	experimental gas-cooled reactor
FTIR	Fourier-transform infrared
GC	gas chromatography
HTR	high temperature reactor
HTGR	high temperature gas-cooled reactor
HTR-PM	high temperature reactor–pebble bed modular (reactor)
INL	Idaho National Laboratory
IPDR	in-pore diffusion rate
JAERI	Japan Atomic Energy Research Institute
KAERI	Korea Atomic Energy Research Institute
KAIST	Korea Advanced Institute of Science and Technology
LH	Langmuir-Hinshelwood
LOCA	loss of coolant accident
MHTGR	modular high temperature gas-cooled reactor
MS	mass spectrometry
MSR	molten salt reactor
ORNL	Oak Ridge National Laboratory
OTM	oxygen transfer model
ppm	parts per million
RPM	random pores model
RSA	reactive surface area
S/V	surface / volume
TGA	thermogravimetric analysis
TRISO	three-structural isotropic (fuel particle)
TSA	total surface area
VHTR	very high temperature gas-cooled reactor
VF	vertical furnace
XCT	x-ray computerized tomography
XRD	x-ray diffraction

FOREWORD

In writing this review on nuclear graphite oxidation behavior and effects on graphite, the authors have consulted a vast library of more than 250 published documents, more than 170 of which were selected as directly cited references included in this review. However, given the possibility that the authors missed or overlooked information that might be regarded as significant for the subject analyzed, the authors apologize in advance for any involuntary omissions.

Furthermore, the authors have extensive and well-documented personal participation in graphite oxidation research and model development works. Although their perspectives may have influenced the literature selection and presentation of this writing, they aimed to keep a neutral and objective position.

ACKNOWLEDGMENT

Support for this work was provided by the U.S. Department of Energy, Office of Nuclear Energy via the X Energy, LLC. Advanced Reactor Concepts (ARC) 15 Award. Oak Ridge National Laboratory is managed by UT-Battelle, LLC, under contract No. DE-AC05-00OR22725for the U. S. Department of Energy.

ABSTRACT

This report is an attempt to summarize the vast number of publications, research reports, and official documents related to environmental effects on nuclear graphite components in high-temperature gas-cooled reactors (HTGRs). This task is monumental given the fact that the synthetic graphite industry is at a least a century and half old, that synthetic graphite has been used as a moderator (and more recently, as a structural element) from the first nuclear reactor build by Fermi, and that environmental factors in gas-cooled reactors introduce significant changes in graphite's structure and properties, which could have severe consequences on a reactor's operating capacity, its structural integrity and lifetime, and the environment and community's health.

During their multidecade operation in the core of nuclear reactors, graphite components are subjected to aggressive and continuous exposure to a high field of ionizing and neutron irradiation, high temperature, and various types of present and postulated chemical attacks. High-density, high-crystallinity polygranular synthetic graphite is unique among other materials for its extraordinary capacity of resisting and adapting to the aggression inflicted by high-temperature, high-energy neutron bombardment and ionizing gamma radiation. However, as a carbonaceous material, even though it has very high purity, graphite is reactive toward common oxidizing agents, such as oxygen, carbon dioxide, and water. Safe operation of HTGRs relies in part on engineered safeguard systems to protect graphite components efficiently and continuously against oxidation. Graphite oxidation behavior is an important direction of theoretical and experimental research, engineering analyses, models and simulations, and design and safety regulations. The massive quantity of publications, reports, experimental data, computer codes, and regulatory documents related to oxidation behavior of nuclear graphite is now accelerating to new levels, prompted by the increased interest in nuclear energy as a clean, carbon-free energy source. Although generation II and III nuclear reactor accidents might still negatively affect perceptions of nuclear energy advantages, generation IV nuclear reactors are designed at very high safety standards that have been improved through great advances of scientific knowledge and technological progress. One focus of these recent advances is directed at better understanding graphite oxidation behavior, its relationship with graphite manufacturing and microstructural properties, and the effects of various environmental factors and process variables. The recent progress in manufacturing, properties characterization, and modeling of intricate physical and chemical processes that determine graphite's oxidation behavior led to the development of powerful simulation codes that can analyze various scenarios of normal operations and hypothetical off-normal events, and thus clearly specify the allowable parameters envelopes for the designers, constructors, and operators of current and future modular HTGRs.

This review begins with an introduction on manufacturing methods, structure, and properties of nuclear graphite, including basic requirements that this specialty graphite type must satisfy for nuclear use. It then summarizes the environmental effects on nuclear graphite, with an emphasis on oxidation phenomena, their safety implications, and the basic traits of chronic and acute oxidation by air (oxygen) and water (humidity, steam). Particular attention is placed on the three graphite grades of interest for this review, IG-110, NBG-18, and PCEA. Next, a section describes the degradation of properties induced by oxidation, focusing on density, dimensional, and mechanical properties changes. The next section briefly reviews various approaches used for modeling of graphite oxidation behavior. It summarizes the progress of oxidation models from the early attempts to complex computational approaches interfaced with specialized computer codes designed for nuclear reactor simulations. Finally, knowledge gaps where more research is needed are presented, followed by a short summary that concludes the review.

1. INTRODUCTION

The class of materials commonly referred to as *nuclear graphites* includes numerous types of polygranular manufactured (synthetic) graphites with high purity and isotropic or near-isotropic structure that are suitable for use in high-temperature gas-cooled reactors (HTGRs) and molten salt reactors (MSRs).[1] In these applications, the primary role of graphite is to slow down (i.e., moderate or thermalize) fast neutrons resulting from fission of nuclei of heavy fissile actinide elements (e.g., ^{233}U and ^{235}U). The low-energy, slow-moving neutrons have a greater probability of being absorbed by another fissile nucleus. The latter nucleus is split and releases another two or three high-energy neutrons, thus continuing the nuclear chain reaction that releases energy. Graphite in HTGRs also acts as a conduit for thermal energy to the heat exchanging elements of steam generators, and controls oxidation, protects the fuel, and contains the spread of fission byproducts in an unlikely off-normal event scenario.[2]

The main properties that make graphite an ideal component of high-temperature reactors (HTRs) are its low neutron absorption cross-section and high neutron-moderating effectiveness. Other important properties are graphite's high thermal and electric conductivity, resistance to neutron damage, high chemical stability (in a nonoxidizing atmosphere), high inertness versus metals and molten salts, low thermal expansion coefficient and consequently high thermal shock resistance, high melting point and high strength at temperature, and low density. However, because of the electron structure of carbon atoms, nuclear graphite has reducing properties, which means that it can be easily oxidized and requires protection against oxidants.

Nuclear graphite and charcoal are both carbon-based materials, but there are many significant differences that make charcoal flammable and provide nuclear graphite with high resistance toward ignition. Charcoal has a high content of volatile and flammable hydrocarbons impregnated in its extended and easily accessible porosity, whereas graphite has a very low area of internal pores and a highly ordered structure at the atomic level. The compact crystalline structure of graphite precludes oxygen access to most of the reactive sites of its crystallites edge sites. Moreover, charcoal has numerous metallic impurities that favor oxidation by catalytic action (and leave behind large amounts of ash), while the maximum ash content allowable in high-purity nuclear graphite is strictly regulated to no more than 300 ppm.[3] In addition, graphite's high thermal conductibility quickly dissipates the heat and interrupts self-sustained chain reactions characteristic to open flame burning of charcoal. Similar properties allow massive graphite electrodes used in steel making to withstand temperatures of up to 1600 °C in open air, thus being an essential component of electric arc furnaces for steel refining. In contrast, the best charcoal burning furnaces normally operate below 260 °C. However, red-hot glowing graphite electrodes are consumed by fast oxidation reactions above 1000 °C, which corrode their surface until they must be replaced.

Even though "graphite does not burn,"[2] graphite is oxidizable. A quick calculation shows that the rates of C–H_2O and C–O_2 reactions are 3 times and 100,000 times *faster* than the rate of C–CO_2 reaction at 800 °C in 0.1 atm pressure, while the rate of C–H_2 reaction is 3,000 times *slower*.[4] This ranking is provided here only for comparation (and should not be used for other purposes) and reflects the much higher reactivity of O_2 versus that of CO_2 and H_2O, and the extremely low reactivity of H_2.

The main safety concerns for HTGRs operation are accidental air ingress or steam ingress over the hot HTGR core. Of these two scenarios, steam ingress is more damaging because it may generate explosive gas mixtures containing hydrogen and carbon monoxide. These off-normal transient events are classified in three broad categories based on their occurrence probability. Anticipated events (AEs) with 10^{-2} probability per plant-year (once per 100 years) are scenarios of either a small steam generator leak or a small breach in the helium pressure boundary. Design basis events (DBEs) are the most serious accident conditions for which the designers must plan. They have a very low probability (10^{-2}–10^{-4} per plant-year) but potential serious (radiologic) consequences. Examples include a steam generator leak lasting for several

hours or a small break in helium pressure boundary for more than 40 days. Last, beyond design basis events (BDBEs) are extremely unlikely events (10^{-4}–5×10^{-7} per plant-year) that are nevertheless included in safety analysis studies of system performance. More information and case examples DBE are available elsewhere.[2]

Even though anticipated and design-based events are low probability and may occur, at most, once in a plant's fleet service life, the magnitude of the damage to the graphite components must be evaluated. The recent progress in modeling graphite oxidation during air or steam ingress is the result of increased accuracy of computational fluid dynamics (CFD) tools used to predict gas flow and temperature distribution in HTGRs. An impressive volume of experimental results on graphite oxidation by either air of water also became available in the recent years, stimulated by the interest in high temperature reactors (HTRs), either gas-cooled (HTGRs) or molten salt-cooled reactors (MSRs). These data provide the input information for various models of oxidation behavior under various scenario conditions within the design parameters envelope.

The purpose of this document is to review information available in the public domain regarding oxidation behavior and the effects of oxidation on degradation of properties. The focus is on three nuclear graphite grades: one superfine grained graphite (IG-110), one medium-fine grained grade (PCEA), and one medium grained graphite (NBG-18). Of these grades, NBG-18 is manufactured from coal tar pitch, and IG-110 and PCEA are made from petroleum-based subproducts. They come from different vendors: Toyo Tanso, Japan (IG-110); GrafTech (now Amsted Graphite Materials), USA (PCEA); and SGL Carbon, Germany (NBG-18). The forming methods are also different: isostatic molding (IG-110), vibrational molding (NBG-18), and extrusion (PCEA). This large variation of raw materials and forming techniques leads to distinctive properties of each graphite grade.

2. NUCLEAR GRAPHITE MANUFACTURE

Synthetic graphite materials are highly engineered products manufactured by combining and compacting carbonaceous particles and binder, followed by heat treating.[5,6,7] Based on their structure, they are best thought of as polygranular graphite–graphite composites. Porosity in the product is unavoidable, but it does provide several beneficial characteristics. The overall quality and variety of manufactured graphite has improved significantly over time from advances in raw materials, optimization of process steps, and demand from new applications.[8,9,10] Figure 1 shows a schematic illustration of the operational chain that transforms raw carbonaceous materials into manufactured polycrystalline graphite.

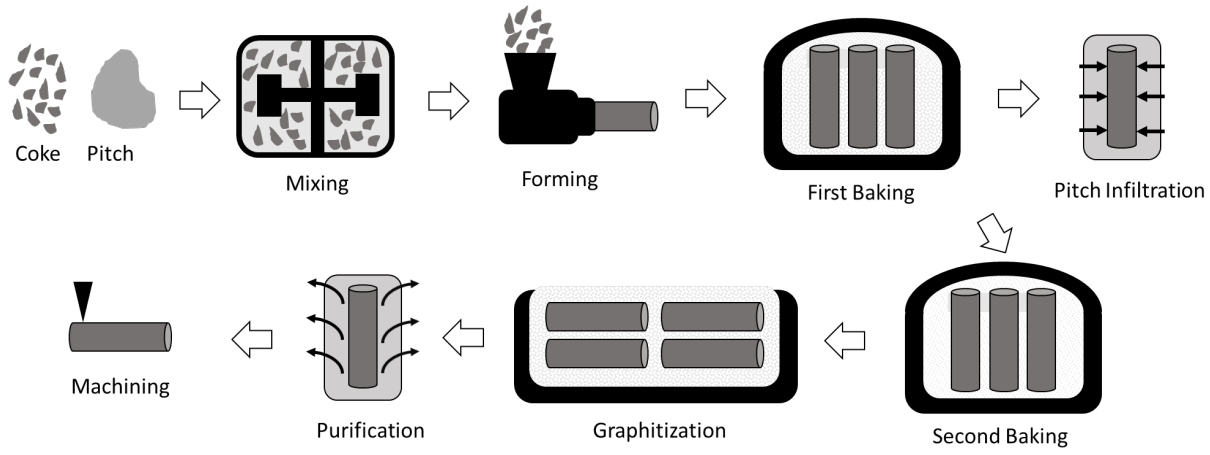

Figure 1. Schematic illustration for manufacturing of synthetic polycrystalline graphite. (Authors' design)

2.1 OPERATIONS SEQUENCE

2.1.1 Raw Materials

Manufacturing graphite materials begins with the selection of suitable raw materials. First, a source of carbonaceous particle is selected (i.e., coke), which is a by-product of petroleum or coal tar refining. The exact coke characteristics depend on the source. One category is needle coke, a highly oriented elongated carbonaceous particle with high levels of purity. Needle coke is desired for applications that require long-range crystallinity in the final product. Second is sponge coke or regular coke, which is used in large amounts to make carbon anodes for aluminum manufacturing. These cokes are harder than needle cokes and more round in shape. Regular cokes lead to more isotropic properties than needle coke. Calcination of coke is usually performed in a kiln at the same location as the coking. Most graphite products begin with calcined coke. Pitch is a binder used to hold the carbonaceous particles together during the forming process. Most binder pitches are coal tar pitches, although petroleum pitches are also available for use as a binder.

2.1.2 Mixing and Forming

Before mixing, the calcined coke will be crushed or milled and sized/sieved. Proportions of sized particles of different dimensions are weighed and mixed to create the desired particle size distribution. Creating the desired particle size distribution in graphite products is sometimes regarded as an "art" by manufacturers. Particle packing needs to be tight enough to enable high density, but also must be mixable to produce a homogeneous product. Mixing is typically carried out as a batch process, followed by a forming operation. A portion of coal tar pitch will be mixed into the calcined coke as the binding agent. Various types of mixers are available, which use different mixing actions.

Extrusion is fairly straightforward in design and can produce large diameters and long lengths. Extrusion can also be semi-continuous based on the feed supply. One trade-off is that extrusion will align any elongated particles in the mix. Another longstanding forming operation is molding. Molding a shape will not cause the same alignment and orientation of elongated particles in the mix as extrusion, although some alignment will be present anyway. Iso-molding is a type of molding in which pressure is uniformly applied around the piece.

2.1.3 Carbonization (Baking)

After the forming operation, the product is composed of calcined coke held together with coal tar pitch. The pitch has wetted the surface of the coke and infiltrated in the open pores of the coke particles. Carbonization (baking) is the process of thermally transforming the coal tar pitch into solid coke to create a rigid carbon article. Baking is performed in a non-oxidizing atmosphere to prevent oxidation of the pitch because baking may be performed up to 1000 °C. The duration of baking required is strongly dependent on the sizes of the products and the design of the baking furnaces. Temperature differentials within the furnace and within the product must be carefully monitored. After baking, the carbon article has lower density because of the carbon yield of the pitch. Components in the pitch that did not polymerize to form coke will volatilize. These volatile gases must be transported out of the structure during baking.

2.1.4 Pitch Infiltration

To increase the density of the formed articles, pitch infiltration is performed after baking. Pitch infiltration of baked products is performed in an autoclave, during which heat and pressure are used to force pitch into the open pores. Pitch that is used for pitch infiltration has different properties than the one used for binder. The duration of pitch infiltration depends on the size and permeability of the baked product. Following pitch infiltration, the material is again carbonized (baked).

2.1.5 Graphitization

The goal of graphitization is to convert carbon to some degree of graphite. Graphite is a relatively soft product, which is not desired for most applications. However, the journey of carbon becoming graphite has already begun with calcination of the coke, and then the carbonization process. As the temperature is increased, the structure continuously changes. Layer planes are condensing, other layers are rotating, and significant changes are observed to electrical resistivity and thermal conductivity. During graphitization, the material must be protected from oxidation.

From an equipment perspective, the product is graphitized in two primary ways in industry. Acheson furnaces have been in use since the 1890s, in which the product is buried in a mound of carbonaceous particles. Electric current is applied to the mound, which increases in temperature because of Joule resistive heating. The other method is longitudinal graphitization, in which electricity is applied directly to the product.

The graphitization process brings the product to a high temperature, perhaps up to 3000 °C, but very commonly up to 2800 °C. Graphitization is also a thermal purification process. However, the impurities are not sufficiently removed for all applications. A separate purification step can be performed, and a common process is thermal purification in the presence of a halogen gas.

2.1.6 Machining

The processing of graphite products yields finished generic shapes such as cylinders and blocks. However, graphite is machinable to a wide range of shapes. In machining, graphite dust must be controlled. Graphite can be machined and polished to a fine finish if desired, but porosity can contribute to surface roughness.

2.2 SPECIFIC REQUIREMENTS FOR NUCLEAR GRAPHITES

To be qualified for use in nuclear reactors, polycrystalline manufactured graphite must satisfy a few specific conditions, outlined as follows:[1,3,10]

- High purity, required by neutronic considerations and decommissioning needs (boron content less than 2 ppm, total ash content less than 100 ppm).
- High density, because the greater the density, the more efficient is neutron flux moderation.
- High crystallinity and high stability under neutron irradiation. Dimensional changes and defect multiplication can be minimized by selecting the source of pitch, the coke, and the manufacturing process.
- High thermal conductivity for efficient dissipation of the heat generated by fission processes
- High strength
- High oxidation resistance
- High coefficient of thermal expansion (CTE), about 4×10^{-6} K^{-1} (20–120°C), to ensure high dimensional stability upon irradiation
- Low anisotropy (< 1.1), defined as ratio of CTEs in orthogonal directions
- Low elastic modulus
- Low cost

Typical properties of nuclear graphite are as follows:[10,11]

- Density: 1.75 to 1.85 g/cm^3
- Tensile strength: 20 to 30 MPa
- Bend strength: 30 to 45 MPa
- Compressive strength: 70 to 90 MPa
- Young's modulus: 9 to 12 GPa
- CTE: 3.5 to 4.5 (10^{-6} K^{-1})
- Thermal conductivity: 120 to 150 W/mK
- High degree of graphitization (≥ 95%, based on x-ray diffraction analysis)

Table 1 shows general properties of the three graphite grades in the focus of this literature review, based on data measured at the US Department of Energy's Oak Ridge National Laboratory (ORNL).[12]

Table 1. General properties of graphite grades of interest [12]

	IG-110	PCEA		NBG-18	
	Isotropic	WG	AG	WG	AG
Manufacturer	Toyo Tanso, LTD	GrafTech (now Amsted Graphite Materials)		SGL Carbon GmbH	
Coke type	Petroleum	Petroleum		Pitch	
Forming method	Isostatically pressed	Extruded		Vibrationally molded	
Grain size (μm)	20 (average)	800 (maximum)		1600 (maximum)	
Ash content (ppm)	<10	<10		<10	
Crystal lattice constant, <c> (Å)	3.3658	3.3665		3.3695	
Crystal lattice constant, <a> (Å)	1.231	1.2311		1.2315	
Coherent domain size, L_c (Å)	190	238		191	
Coherent domain size, L_a (Å)	256	250		294	
Bulk density (mensuration) (g/cm^3)	1.761	1.794	1.791	1.871	1.867
Skeletal density (Hg porosimetry) (g/cm^3)	2.007	2.216		2.162	
Tensile strength (MPa)	14.9	18.46	17.04	18.27	19.16
Compressive strength (MPa)	73.44	57.94	61.56	80.54	79.28
Dynamic young's modulus (GPa)	8.767	10.234	9.396	11.648	12.108
Sonic velocity, longitudinal (m/s)	2,324	2,619	2,469	2,817	2,889
Sonic velocity, shear (m/s)	1,482	1,384	1,370	1,458	1,479
Modulus (GPa)	8.96	8.96	8.59	10.48	10.8
Shear modulus (GPa)	3.87	3.44	3.37	3.98	4.08
Poisson ratio	0.157	0.306	0.277	0.317	0.323

Note: WG = with grains; AG = against grains

3. STRUCTURE AND PROPERTIES

Nuclear graphite is a composite with three main components: filler, binder, and pores (Figure 2). Its structure is highly dependent on the raw materials (filler and binder's precursors), the type of forming process, and the details of the baking, impregnation, and graphitization sequences of manufacturing. Small variations in any of these manufacturing steps, or variations in the nature and properties of the raw materials, may significantly affect the properties (mechanical, thermal, oxidation resistance and neutron irradiation behavior) of the final product. Although the structure and properties of graphite are difficult to control, this multiplicity of available process parameters allows manufacturers to finely tune the product with the best combination of properties for a given application. All specific information on the manufacturing process remains confidential and proprietary to the graphite vendor.

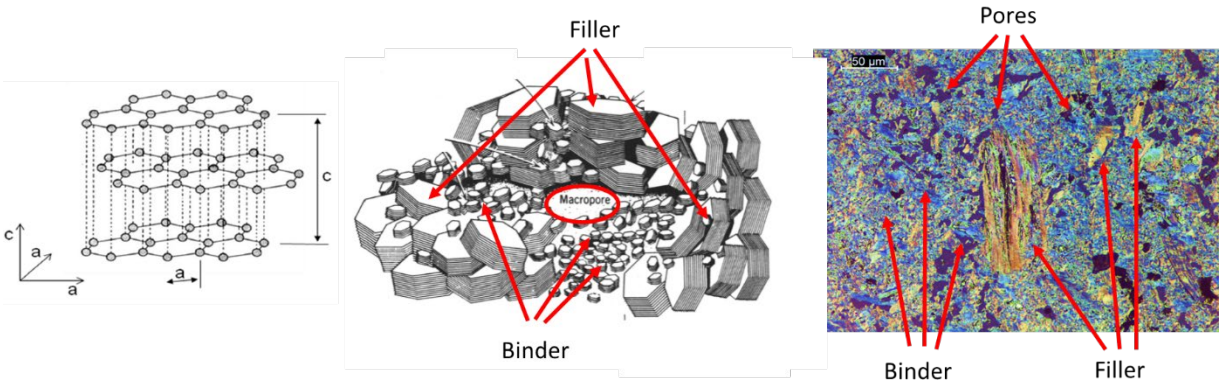

Figure 2. Length scale–dependent views of nuclear graphite structure. Left: graphite crystal structure; Center: schematic view of graphite crystallites forming the filler grains, binder mosaic, and pores of various sizes (modified from reference[13]); Right: optical microscopy image with polarized light as an illustration for the actual structure of nuclear graphite (scale bar = 50 µm).

X-ray diffraction (XRD) shows that nuclear graphites have highly crystalline structure, with the lattice parameters along the <a> (d_{110} in the basal plane layer) and <c> directions (d_{002} normal to basal plane layers) only marginally different from those of ideal graphite crystals. The crystallite dimensions along basal planes (L_a) and in the perpendicular direction (L_c) reach several hundred Ångstroms.[14] Crystallites are very often joined to form grains of various shapes, which originate from graphitized filler particles. Some grains may show adjoined crystallites in a parallel orientation, as discovered by optical microscopy with polarized light.[15] The grain size is an important differentiator of nuclear graphite types because many properties depend on the size of filler particles in the original mix. Nuclear graphites are classified in 8 classes based on their grain size, which can vary across three orders of magnitude between coarse grains (< 2 mm) and microfine grains (< 2 µm).[1] The shape of filer particles depends on the type of raw materials: graphite obtained from petroleum products (IG-110, PCEA) usually have elongated acicular grains, whereas those based on coal tar pitch (NBG-18, G347) tend to have oblate or spherical grains.[16]

Although the graphitization degree of nuclear graphites calculated from XRD parameters is very high (about 95–97 %), the apparent densities are lower (1.75–1.85 g/cm^3) than the density of perfect graphite crystals (2.24 g/cm^3). The difference is caused by the volume of various pores in graphite, which are usually 20–25 % of the volume. Pores are created by incomplete densification in the manufacturing process, by gas evolution and trapping during thermal processes, and by anisotropic shrinkage differences between filler grains and the surrounding binder phase (Mrozowksi cracks). Micropores (diameter < 2 nm) are absent from synthetic graphites, but larger pores, classified as mesopores (2–50 nm) and macropores (> 50 nm) are present in many shapes and sizes.

Figure 3 shows optical microscopy images under polarized light collected at ORNL for IG-110, PCEA, and NBG-18. There are clear differences between these grades. The fine grains in IG-110 are visible as distinct blue and yellow spots under the polarized light, depending on the crystallite orientation versus the plane of polarized light, and the pores are barely visible as dark spots. In medium-grained PCEA, the crystallites and the pores are larger, and apparently not interconnected. NBG-18, with the largest grain sizes, also has the largest (and most of them isolated) pores.

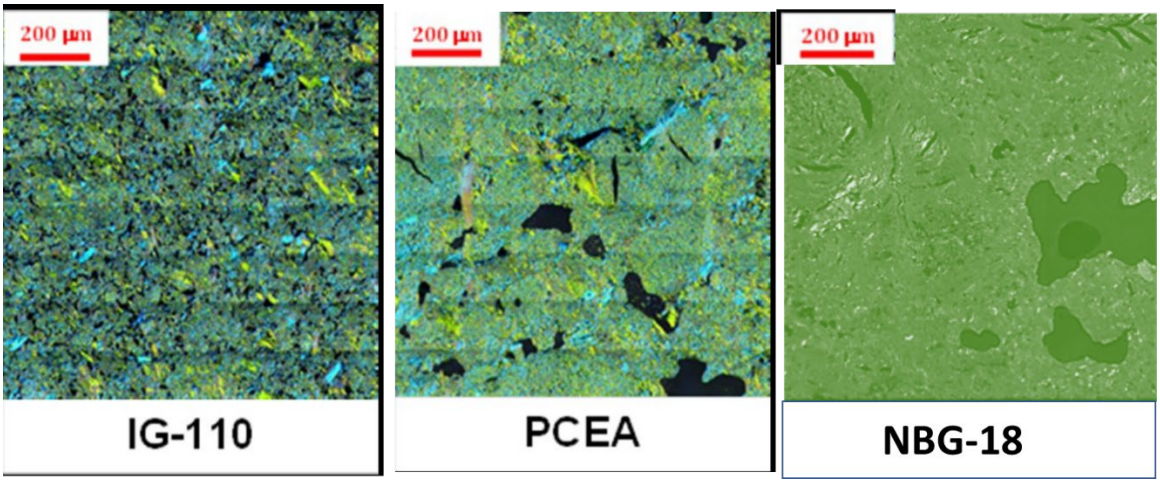

Figure 3. Porous structure of graphites IG-110, PCEA, and NBG-18 revealed by optical microscopy. Images were collected with polarized light. (Authors' images)

Figure 4 shows electron microscopy images of fractured surfaces in the same three grades of graphite. The disordered, chaotic structures of multiple stacked layers expose reactive carbon atoms at their broken edges. Along with the numerous broken structures, these are the sites (most likely in the binder) where oxidation starts. On the other hand, IG-110 shows large flat regions, likely cleavage planes of graphite crystallites, which are more resistant to oxidation.

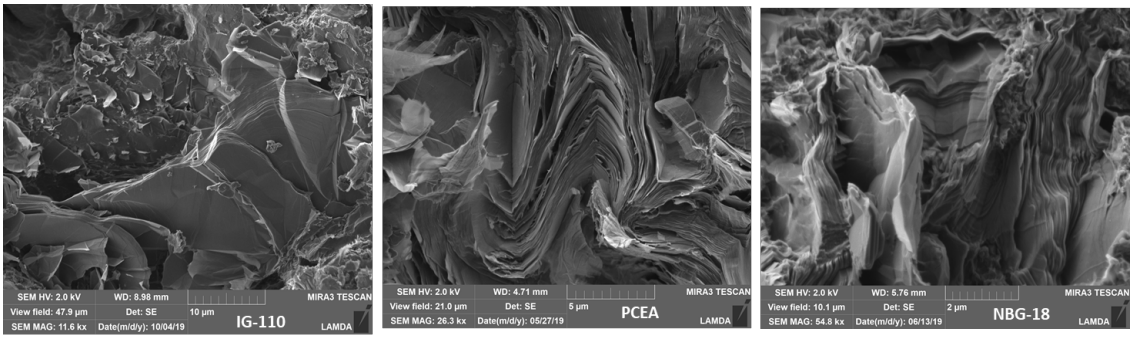

Figure 4. Scanning electron microscopy images of fractured surfaces of graphites IG-110, PCEA, and NBG-18. (Authors' images)

Figure 5 shows porosity data on the same graphites measured at ORNL by nitrogen adsorption and pressurized mercury intrusion. Gas adsorption explores the range of nanometer-sized pores (1 nm = 10 Å). Nuclear graphites are free of micropores (diameter <20 Å) but have developed mesopores volumes (20–500 Å) and substantially large macropores (> 500 Å) with a broad range of sizes. In this range of small pore diameters, IG-110 and PCEA have comparable distributions of pore volumes, exceeding that of NBG-18 (Figure 5a). In the range of micron-sized pores, mercury intrusion data (Figure 5b) show that IG-110 has

larger pores volume within a narrow distribution open macropores (average diameter 3.9 μm), whereas PCEA and NBG-18 have smaller pore volumes with diameters in a broad range of sizes.

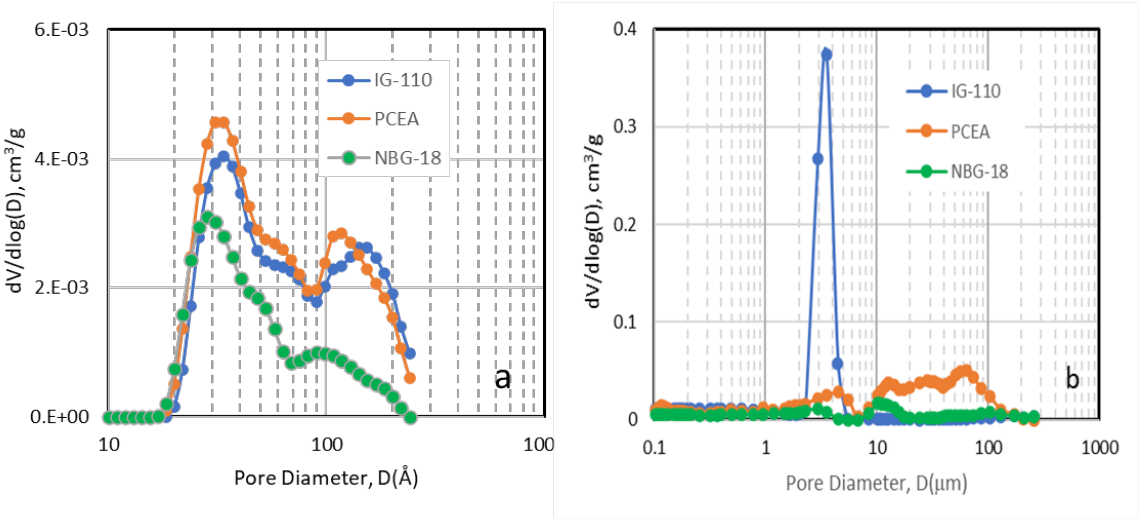

Figure 5. Pore size distributions measured by (a) gas adsorption and (b) mercury intrusion porosimetry. (Authors' data)

Table 2 (based on authors' data) illustrates the differences in surface area, density, and porosity among the graphite grades of interest. Fine-grained IG-110 has small size pores, but their cumulative volume is greater than the pores of PCEA and NBG-18. The latter has pores of much larger size (Figure 3) which appear to have no communication to the exposed surfaces (Figure 5b). This conclusion agrees with observations made elsewhere.[16,17]

Table 2. Surface area, density, and porosity of graphite grades of interest

Graphite grade	Surface area[a]			Density[b]		Pore volume[c]			Total porosity fraction (%)	Average pore diameter[d] (μm)	Grain size (μm)
	TSA (m^2/g)	BPA (m^2/g)	ASA (m^2/g)	Bulk (g/cm^3)	Skeleton (g/cm^3)	Open (cm^3/g)	Closed (cm^3/g)	Total (cm^3/g)			
IG-110	1.38	0.27	1.11	1.76	2.05	0.079	0.041	0.120	21	3.9	10
PCEA	1.55	0.25	1.30	1.77	2.00	0.065	0.054	0.119	21	64	600
NBG-18	1.09	0.07	1.02	1.86	2.02	0.044	0.048	0.092	17	12	1800

[a] Gas adsorption method: TSA = total surface area by BET method; BPA = basal plane area; ASA = active surface area[17]
[b] Bulk density according to ASTM C559;[18] skeleton density according to ASTM B923.[19]
[c] Open and pore volumes calculated from bulk, skeleton, and theoretical graphite densities.
[d] Average pore diameter according to ASTM 4284.[20]

4. ENVIRONMENTAL EFFECTS ON NUCLEAR GRAPHITE

Graphite components in HTGRs are exposed to high temperatures, neutrons, and gamma irradiation. Furthermore, they are continuously exposed to very low concentrations of oxidizing impurities in the He coolant. In an unlikely accidental occurrence, classified either as anticipated or design-based event (AE or DBE), graphite may be exposed to variable amounts of either air or steam over short periods of time. Each of these challenges has different effects on the graphite structure, density, dimensions, mechanical and thermal properties. They are examined in this section in the order of increasing consequences on graphite component integrity.

4.1 IRRADIATION

4.1.1 Ionizing Radiation

Exposure to ionizing (gamma) radiation in inert gas appears to have insignificant (and sometimes contradictory) effects on nuclear graphite. Exposure of graphite in advanced gas reactors that are cooled by CO_2 (currently operational in the United Kingdom) causes radiolytic graphite oxidation and mass loss. In this environment, gamma radiation splits CO_2 molecules and creates activated ions or radicals, which attack (oxidize) graphite at the reactor temperature (radiolytic oxidation). On the other hand, high-energy gamma irradiation in air at ambient temperature was shown to cause localized damage to the crystalline structure of nuclear graphite from nanometers to microns.[21] According to another report, gamma irradiation in nitrogen at ambient temperature had the opposite effect on graphite (grade not specified), slightly improving the crystalline structure.[22] Finally, another source reported that gamma irradiation in air or moist He of several nuclear grades (including IG-110 and PCEA) did not have any measurable chemical effects, other than reversible superficial oxidation (within about 10 nm from the surface), which disappeared at higher doses.[23]

In conclusion, although graphite components in HTGRs will undergo gamma irradiation during operation in the He coolant at high temperature, the chemical and structural effects are expected to be minor in comparison with other challenges from the reactor's environment.

4.1.2 Neutron Irradiation

The vast subject of graphite irradiation by high-energy neutrons is beyond the scope of this review. Multiple comprehensive reviews and well-informed research reports are available.[24,25] As is well known, the primary effect of neutron irradiation is the dimensional changes. After initial shrinking, which could be up to 10%, the expansion after the turnaround point restores (or may even go beyond) the original dimensions. These changes are accompanied by severe structural damage at the atomic and crystal scales: development of local defects (vacancy loops, aggregated interstitials), roughening of graphite layers (graphenes), crystallite fragmentation, and loss of coherent order, which eventually may cause graphite amorphization. Structural changes induce variation of many other properties: porosity, density, thermal conductivity, mechanical strength and elastic properties, and creep.[26,27,28] The structural defects induced by irradiation may lower the oxidation resistance of irradiated graphite. However, because of self-healing at high temperatures, neutron irradiation at HTGR operating temperatures is expected to have much less influence on oxidation compared with irradiation effects at the lower temperature of CO_2-cooled reactors in the United Kingdom.[29]

4.2 OXIDATION

4.2.1 General Behavior

All carbon materials are susceptible of being oxidized by oxygen, water, or carbon dioxide:

$C_{solid} + O_{2\ gas} = CO_{2\ (gas)}$	ΔH = - 393.7 kJ/mol	(exothermic)
$C_{solid} + ½\ O_{2\ gas} = CO_{(gas)}$	ΔH = - 111.4 kJ/mol	(exothermic)
$C_{solid} + H_2O_{\ gas} = CO_{\ gas} + H_{2\ (gas)}$	ΔH = + 130.4 kJ/mol	(endothermic)
$C_{solid} + CO_{2\ gas} = 2\ CO_{\ gas}$	ΔH = + 170.8 kJ/mol	(endothermic)

The heats of reaction at standard conditions, ΔH, are also provided. While thermodynamics characterizes the energetic probability of these reactions. At ordinary temperatures, thermodynamic equilibrium conditions favor formation of gaseous products (CO, CO_2) from the reaction between carbon and oxygen. However, carbon materials are stable in ambient conditions do not go spontaneously to CO and CO_2. This is because the extent by which these reactions go to completion depends on kinetics, as it will be discussed in this review. Similarly, the reactions of carbon dioxide and water with carbon do not form large amounts of products until temperatures exceed some 700 °C.

Nuclear graphite is strictly controlled to contain very low metal impurities, which might catalyze oxidation processes. Standard specifications of isotropic and near-isotropic nuclear graphite limit the ash content to a maximum of 300 ppm for the high-purity grade and a maximum of 1000 ppm for the low-purity grade.[1] In reality, the ash content in typical nuclear graphites is much lower, precluding activation of graphite oxidation by catalytic impurities.

In the absence of catalyzed processes, graphite oxidation follows the following typical sequence:

1. Transport of the oxidant from the gas phase to the graphite surface
2. Adsorption (physisorption) of the oxidant to the graphite surface
3. Formation of carbon–oxygen chemical bonds (chemisorption)
4. Breaking of carbon–carbon bonds
5. Desorption of carbon–containing oxidation products (carbon oxides)
6. Transport of oxidation products to the graphite surface and release to the gas phase

While the rate of chemical reactions varies exponentially with temperature, the rate of diffusional transport varies as T^q ($1.5 < q < 1.75$). The competition between chemical kinetics and transport rates determines a specific variation of global oxidation rates on temperature. Depending on which of the previous steps is the slowest (i.e., rate controlling), the regimes of graphite oxidation are usually classified as follows:[4]

a. Regime 1 (chemical kinetics control) occurs at low temperatures, where chemical rate is slower than the rate of oxidant diffusion into the graphite body. When diffusion is unrestricted, the oxidant concentration is (theoretically) uniform throughout the bulk of graphite; in ideal conditions, oxidation occurs uniformly in all volume of the graphite component. In this regime, chemical rates

depend largely on the intrinsic reactivity of graphite, which depends on concentration and distribution of active sites on graphite's internal pores surface. Edge carbon atoms on graphite crystallites are much more reactive than carbon atoms on basal planes. Therefore, graphite grades with fine particles, exposing a large concentration of edge carbon atoms at broken graphite sheets in crystallites, are more reactive than the grades with larger graphite grains.

b. Regime 2 (in-pore controlled diffusion) occurs in the temperature range in which chemical reactions are fast enough as to compete with oxidant diffusion rates. In this regime, oxidation becomes gradually restricted to regions close to the surface of graphite components, where short diffusion paths ensure sufficient oxidant concentration for the chemical reaction. The gradual depletion of the oxidant with the distance from the surface slows down chemical rates and gradually reduces the oxidant attack on the graphite core. The inward diffusion of the oxidant depends on the effective gas diffusivity in the graphite structure; the graphite structure increasingly changes as more porosity is created through oxidation.

c. Regime 3 (boundary layer control) occurs at high temperatures, where chemical rates are so fast that oxidant species are consumed as they reach the exposed surface. At these temperatures, the limiting factor is slow mass transfer through the stagnant boundary layer at the gas/solid interface. Oxidation causes rapid surface corrosion and dimensional reduction. The rate depends strongly on the oxidant partial pressure in the gas phase, flow conditions, and the conditions (roughness) of the graphite surface.

The described categories are generic situations, defined by temperature ranges in the assumption of unlimited oxidant supply. In reality, the oxidant availability and supply rate, in combination with the temperature regime, cause more variation in the graphite oxidation behavior. Two subset cases may be distinguished:[30]

d. Oxidant supply control occurs when oxidation is limited by the low supply rate of oxidant in the gas phase (for example, in the case of an extremely low concentration of water or oxygen impurities in the helium coolant during normal operation). Whether the oxidant penetrates deep under the surface (at low temperatures) or is consumed near the surface (at high temperatures), the chemical reaction rate is extremely slow because it is limited by the extremely low concentration of oxidant species in the gas phase.

e. Oxidant-starving control may occur in conditions when the total amount of oxidant is limited (for example, after a limited air or steam ingress for a short period of time, before being repaired). In this case, oxidation slows down and ends when the oxidant is depleted.

Figure 6 schematically represents the three main oxidation regimes. The top plot shows the variation of oxidation rate versus the reciprocal absolute temperature over a broad range. At low temperature (T) (Regime 1), the variation of ln (*rate*) vs. $1/T$ is linear, as expected for chemical reaction rates (Arrhenius equation). The slope of linear range is used to calculate the apparent oxidation activation energy (E_{app}) in the chemical control regime. As the temperature rises, the plots in Figure 6 show lower slope indicating the transition to Regime 2 (in-pore diffusion control). At even higher temperatures, the slope approaches zero, showing that in Regime 3 (boundary layer control), the effect of temperature on oxidation rates is almost null.

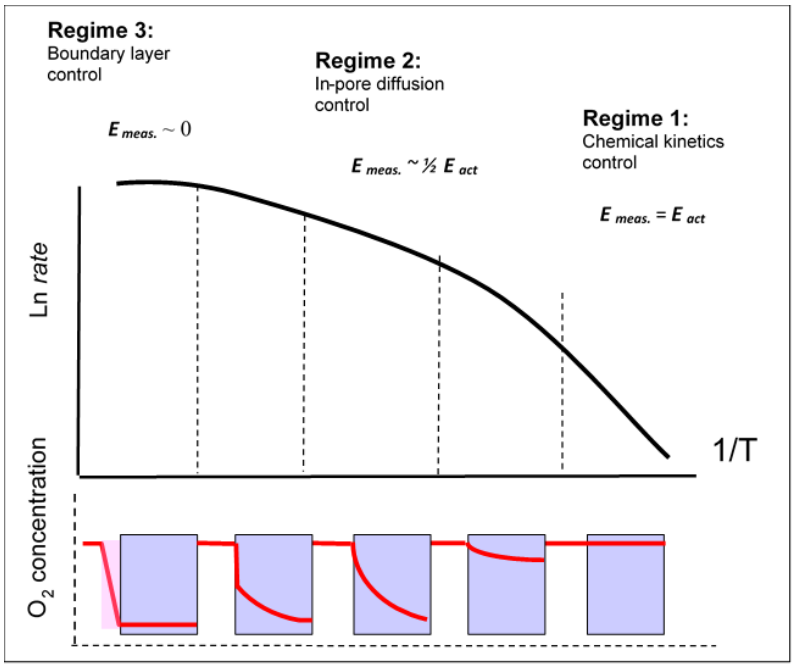

Figure 6. Schematic representation of main graphite oxidation regimes. Top: Arrhenius plot; Bottom: O_2 concentration profiles.

The bottom drawing in Figure 6 depict oxidant concentration in the gas phase and inside the graphite bulk. This illustration suggests that there is no sharp transition between the oxidation regimes. The rate of oxidant supply and the size/shape of the graphite component play an important role in determining how much of the graphite body is accessed by the oxidant. In turn, this determines the temperature range in which diffusion gradually becomes the limiting factor of the overall oxidation process (transition from Regime 1 to Regime 2).

4.2.2 Empirical Observations on Oxidation-Controlling Factors

Graphite oxidation is a heterogeneous gas–solid chemical reaction in which most of the reacting surface is located inside the pores of the solid. Therefore, the overall oxidation rate is controlled by the balance between (1) transport rates of oxidant species (from exposed surface inward through the pore system) and of gaseous oxidation products (from the pore system outward to the free surface), and (2) rates of chemical processes, including adsorption of the oxidant, formation of carbon–oxygen bonds, and desorption of gasification products.

Transport processes (e.g., in-pore diffusion, Knudsen diffusion) determine the profile of concentration distribution of oxidant throughout the mass of the porous solid. Transport-limited chemical reactions are frequently encountered in heterogeneous catalysis. What is particular to graphite oxidation in that the structure of the porous solid itself is being modified by the development of porosity during the progress of reaction. Pores are created, enlarged, and then collapsed as the graphite material is being gradually oxidized. This continuous evolution of the structure is a serious complicating factor for all modeling attempts.

4.2.2.1 Effects of temperature

An empirical (phenomenological) equation for oxidation rates in Regime 1 is provided in Eq. (1):

$$Rate = A_{app} \exp\left(-\frac{E_{app}}{RT}\right), \quad (1)$$

where E_{app} and A_{app} are the apparent (i.e., condition-dependent) activation energy and pre-exponential factor, respectively. In a more elaborated form, the overall oxidation rate in Regime 1 should include explicitly the local concentration (or pressure) of oxidant in pores (P_{ox}) and the transient function (F_b) accounting for variation of oxidation rate as the graphite microstructure changes with the progress of oxidation:

$$Rate_1 = K_1 (P_{ox})^n F_b = k_0 \exp\left(\frac{-E_{app}}{RT}\right) (P_{ox})^n F_b \, . \quad (2)$$

Here, n is the order of reaction for the oxidant, and K_1 is the reaction rate constant, which depends on temperature according to the Arrhenius equation:

$$K_1 = k_0 \exp\left(-\frac{E_{app}}{RT}\right), \quad (3)$$

where the pre-exponential factor k_0 is proportional with the number of surface sites participating in oxidation and the frequency of individual chemical events. An approximation often used for oxidation in Regime 1 is to assume that the oxidant concentration in graphite pores is uniformly distributed through the bulk and equal to the external concentration in the gas phase. At low temperatures, when oxidation is slow, this assumption is approximately correct. Equation (3) can be used to analyze oxidation kinetics in Regime 1.

In Regime 2, oxidation rates increase with temperature and become comparable with the rate of in-pore diffusion of the oxidant. In this case, the local oxidant concentrations (P_{ox}) are determined by the balance between the rate of inward diffusion of oxidant species (according to Ficks' second law) and the rate of their consumption in chemical reactions. The rate of in-pore diffusion is controlled by an effective gas diffusion coefficient in the pore structure, D_{eff}, which is a certain fraction of D_0, the molecular diffusion coefficient in the gas phase: $D_{eff} = \beta D_0$. In general, it is assumed that $0.001 < \beta < 0.01$ and strongly depends on the pore structure (porosity fraction, ε, and tortuosity factor, τ), which evolves with the progress of oxidation. Unfortunately, the definition of $\beta = \beta(\varepsilon, \tau)$ is not unique in the literature, which is a strong impediment for accurately accounting for variation of D_{eff} with the progress of oxidation. However, its variation with temperature is the same as of D_0, which follows the power law $D_0 \sim T^q$ where $1.5 < q < 1.75$. On the other hand, the rate of chemical reaction increases exponentially as $\exp(-E_{app}/RT)$. The imbalance of these temperature trends determines the prevalence of chemical reaction control at low temperatures (Regime 1) and the transition to in-pore diffusion control (Regime 2) when the rate of chemical reaction increases faster with temperature than the diffusion rate (Figure 6).

Modeling oxidation kinetics in Regime 2 is the most challenging out of all three regimes. A two-terms equation for local oxidation rates was proposed[31,32] as follows:

$$Rate_2 = \varepsilon \frac{\partial C_{ox}}{\partial t} = D_{eff} \frac{\partial^2 C_{ox}}{\partial x^2} - Rate_{pore}(C_{ox}, T)\nu \, . \quad (4)$$

Here, C_{ox} is the local concentration (partial pressure) of the oxidant in pores, ε is the fraction of transport porosity, x is the distance from external surface, D_{eff} is the effective diffusivity of oxidant in the pore system, ν is a stoichiometric factor that accounts for the balance between CO and CO_2 as reaction products, and $Rate_{pore}$ is the rate of chemical reaction in pores. $Rate_{pore}$ may be introduced by an equation, similar to $Rate_1$ for Regime 1, or by more complex equations according to Langmuir–Hinshelwood (LH)[32] or the Boltzmann-enhanced Langmuir–Hinshelwood (BLH) models.[33] The BLH model is appropriate for simulation of processes limited by the oxidant supply (such as chronic oxidation by traces of impurities in the coolant) where oxidation products may block reaction sites.[34,35] The LH model was used for simulation of high-pressure steam ingress accidents.[36]

At very high temperatures (Regime 3), the limiting factor is the mass transfer rate between gas and solid phases through the stagnant boundary layer at the interface. In these boundary layer–controlled conditions, the effect of temperature is absent or very weak. Oxidation rates are controlled by the local concentration difference between oxidant species in the bulk gas phase and at the solid surface:

$$Rate_3 = K_m(C_{ox,b} - C_{ox,s}) \,, \tag{5}$$

where the mass transfer constant K_m depends on the gas flow conditions (laminar or turbulent) near the surface.

In simulations, gas phase conditions and flow parameters are modeled by computational fluid dynamics (CFD), and K_m is typically estimated using analogies between heat and mass transfer. Oxidation is restricted to the external surface, where graphite corrosion is accompanied by grain flaking and intense gasification rates. Together, these conditions quickly contribute to geometry changes and fast shrinking of graphite specimens.

The extent of temperature control on the overall oxidation process is formally expressed by the activation energy, which is an element of the Arrhenius model. High activation energies indicate that the gasification follows a high energy path, and therefore, only large changes in temperature can influence the kinetic process. This is encountered in Regime 1 (kinetic, or chemical control). However, although the Arrhenius model is convenient for comparison purposes, it is not fully justified theoretically for gas–solid reactions because the energy distribution functions in solids (either Bose–Einstein or Fermi–Dirac) are different from the Maxwell–Boltzmann distribution of energy levels in gases. Although the differences are minimal at high temperatures, rigorous application of the Arrhenius model (although successful for reactions in homogeneous phase) is negated by the complexity of physical and chemical processes in solid–gas reactions and by the inherent heterogeneity of solid surfaces.[37] Consequently, the slope of Arrhenius plots provides an apparent, or conditionally dependent, activation energy and must not be interpreted as a true, kinetic parameter. Practically, that means that the experimental activation energies reported for the same graphite grade by various investigators may vary substantially with details of the experimental conditions. This is largely illustrated in a subsequent Section 4.3 with examples for oxidation of IG-110 by air.

4.2.2.2 Rate variation with mass loss at constant temperature

Isothermal oxidation rates also vary with the progress of the oxidation process. This behavior is represented by the transient factor F_b in Eq. (2) for Regime 1. Ample evidence shows that isothermal oxidation rates increase gradually with the mass loss, reach a maximum near 30–35% mass loss, and then decrease. This variation reflects the pore development and later collapse with the progress of oxidation. During the initiation stage of oxidation, the active surface increases and reaches a maximum at steady-state conditions, which is followed by a rapid decrease after large amounts of graphite have been consumed. Figure 7 shows oxidation rate data measured at ORNL for NBG-18 and IG-110.[14,38] The plots on a linear scale help visualize how fast oxidation rates increase with every 50°C increment in temperature. With the same data plotted on a semilogarithmic scale, the trends at various temperatures appear to be similar with the increase of mass loss, only shifted on the vertical axis. The behavior is specific to each graphite grade.

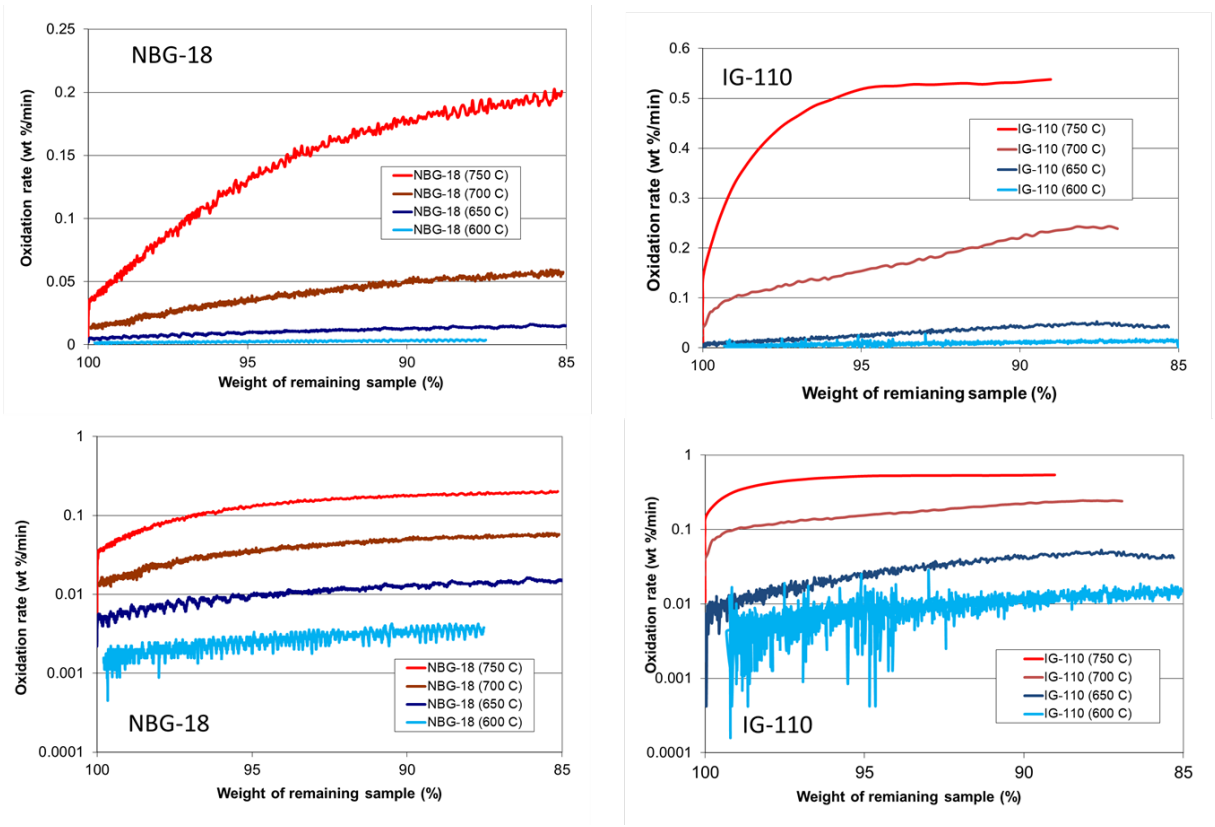

Figure 7. Variation of isothermal oxidation rates with weight loss. Raw data measurements are plotted on linear and logarithmic scales. (Authors' data; more information available in refs.[14,38])

The behavior shown in Figure 7 is commonly observed in porous materials undergoing reactions in corrosive environments (such as graphite oxidation in air). Porous materials react at both their external (geometric) surface and internal (in pores) surface. In-pore reactions cause pore enlargement, development of new pores (or opening of closed ones), and eventually, structural collapse.

Most of the graphite oxidation data were modeled by the 2D random pore model (2D-RPM) developed by Bhatia and Perlmutter.[39] It was assumed that all pores have cylindrical shape and are arranged parallel with the openings at the exposed surface. The reaction rate is assumed constant on all internal pore surfaces. With the development of porosity in the process, the degree of conversion increases with time:

$$X(\tau) = 1 - \exp\left[-\tau\left(1 + \frac{\Psi\tau}{4}\right)\right]. \tag{6}$$

Here, τ is a reduced time and Ψ is a structural parameter. The dimensionless conversion degree is defined as the ratio between the time-dependent mass loss and the initial mass of the unoxidized specimen. The increase of the dimensionless reaction rate as a function of conversion (X) degree is represented by the transient function F_b from Eq. (2), which has the following expression:

$$F_b = \frac{dX}{d\tau} = (1 - X)\sqrt{1 - \Psi \ln(1 - X)}\,. \tag{7}$$

In the original work by Bhatia and Perlmutter,[39,40] Ψ was given a significance based on structural properties of the porous body (dimensionless porosity, pore length, and surface area per geometric body volume). However, other researchers[41,42,43,44,45] who used this model for oxidation of nuclear graphite preferred

finding Ψ by data fitting and did not agree on a common value even for the same graphite grade oxidized in various conditions.

An improved 3D model was recently proposed by Paul.[46,47,48,49] In this 3D-RPM, pores are assumed to be spherical in shape, randomly distributed, and either open or closed. Oxidation is possible only in open pores, which grow and eventually discover and join with neighboring closed pores, which thus become open and oxidizable. The progress of gasification is controlled by two parameters: the intrinsic reactivity (which depends on temperature but not on the graphite grade) and the rate of pore discovery (which is a material property related to graphite microstructure). To apply this model, users need the initial dimension, shape, and density of specimens, the temperature (to evaluate the dependence of intrinsic reactivity), and the pore discovery rate. The pore discovery rate is available from a database built for multiple nuclear graphite grades.[46] The 3D-RPM model separates the intrinsic reactivity from the graphite microstructure and specimens' dimension, which is a major step toward rational oxidation modeling. In principle, after the basic parameters are found by experiments for the graphite grade of interest, they could be further used to estimate the progress of isothermal oxidation with time (or mass loss) over a broad conversion range. Thus formulated, the 3D-RPM model promises to be useful for modeling the progress of oxidation of various size and shape graphite bodies. Figure 8 demonstrates the model's flexibility in reproducing the effects of intrinsic graphite properties (density, reactivity) and particular conditions (diameter) on oxidation rates and transient mass variation with time. However, more work is needed to support the model. Fortunately, experimental data for the initial part of oxidation transient, up to about 5 % mass loss, is available from multiple experiments following the conditions of ASTM D7542[50] and can be used for verification. More development work is needed to explore the effect of nonstandard shape and size, and to expand the conversion range with data beyond the 10–15 % mass loss recommended by this standard test method.

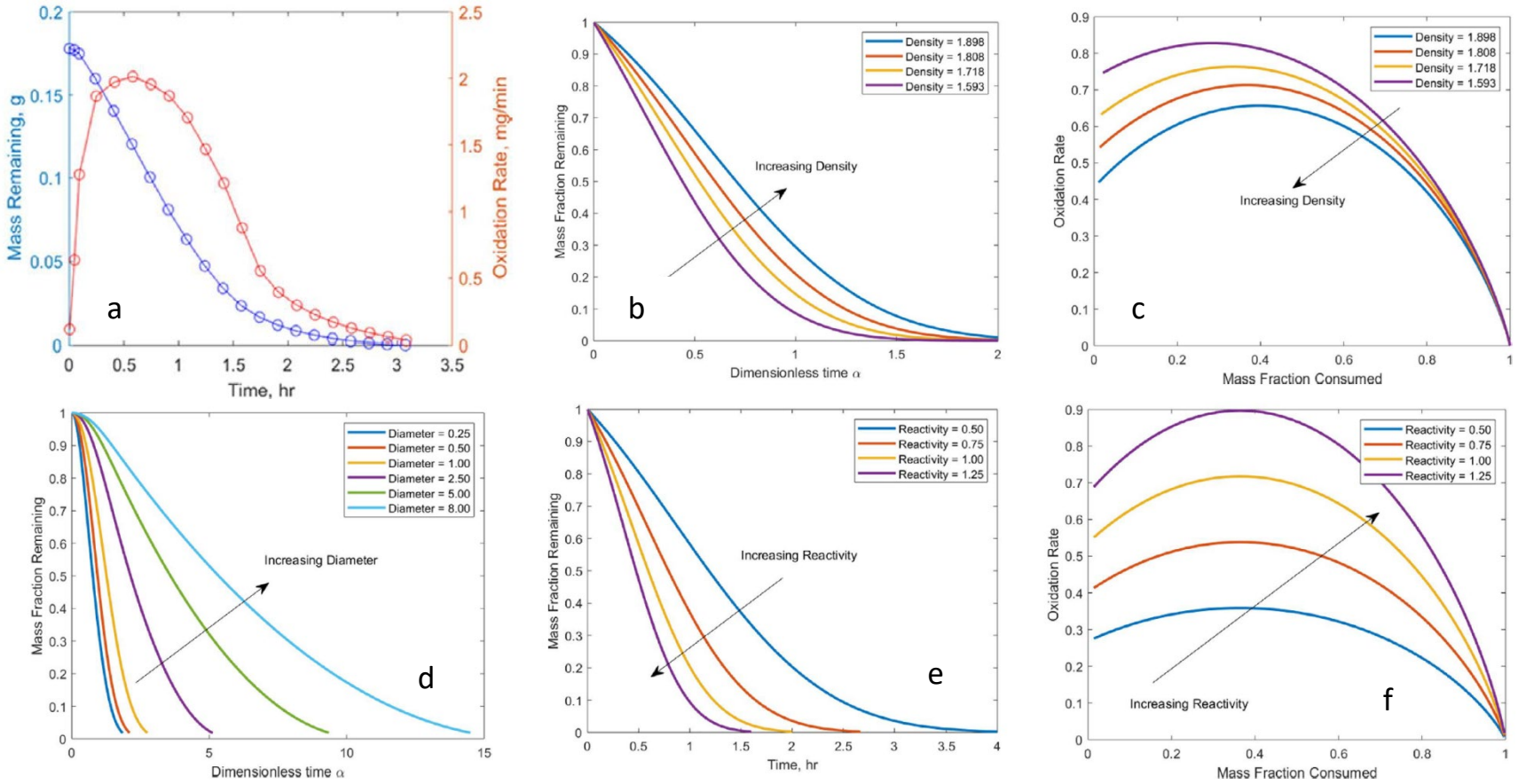

Figure 8. Multiple simulation capabilities of 3D random pore model (3D-RPM). The plots show (a) experimental variation of mass and oxidation rate versus oxidation time; effects of graphite density on (b) mass variation and (c) oxidation rate; (d) effects of specimen diameter on mass fraction remaining; and effects of intrinsic reactivity on (e) mass fraction remaining and (f) oxidation rate. (Authors' data; more information available in ref.[46])

4.2.2.3 Effects of sample size, shape, and flow conditions

In Regime 1, where oxidation is assumed to occur uniformly through all graphite volume, it is expected that oxidation rates do not depend on the graphite sample size. However, this has not been observed. Empirical evidence shows that the smaller the graphite sample, the faster it is oxidized, even at low temperatures. As an example, Figure 9 shows the mass loss variation versus time for oxidation in air of two small (0.2 g) and two large (10 g) specimens of graphite NBG-10 at 450 °C.[31] Furthermore, oxidation rates (at 600 °C) normalized by the geometrical area of exposed surface increased with the surface to volume (S/V) ratio in a series of IG-110 specimens of various shapes and sizes (Figure 10).[51] However, because the flow rate was not reported, the results shown in Figure 10 might have been affected by uncontrolled lows in the ratio between oxygen supply rate and carbon gasification rate.

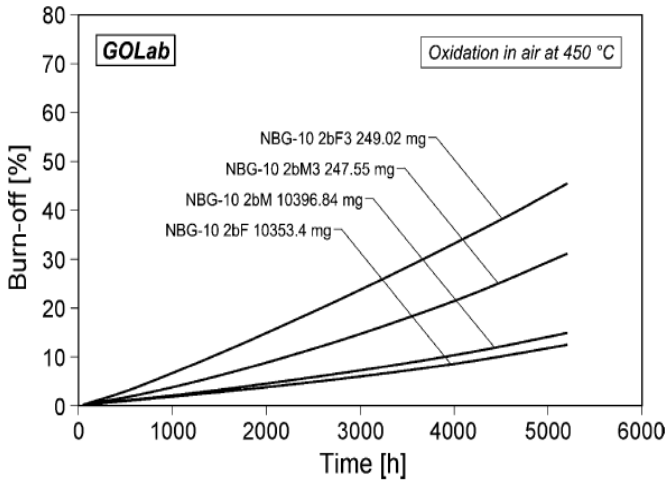

Figure 9. Effect of sample size (or initial mass) on very slow oxidation rates in air at 450 °C.[31]

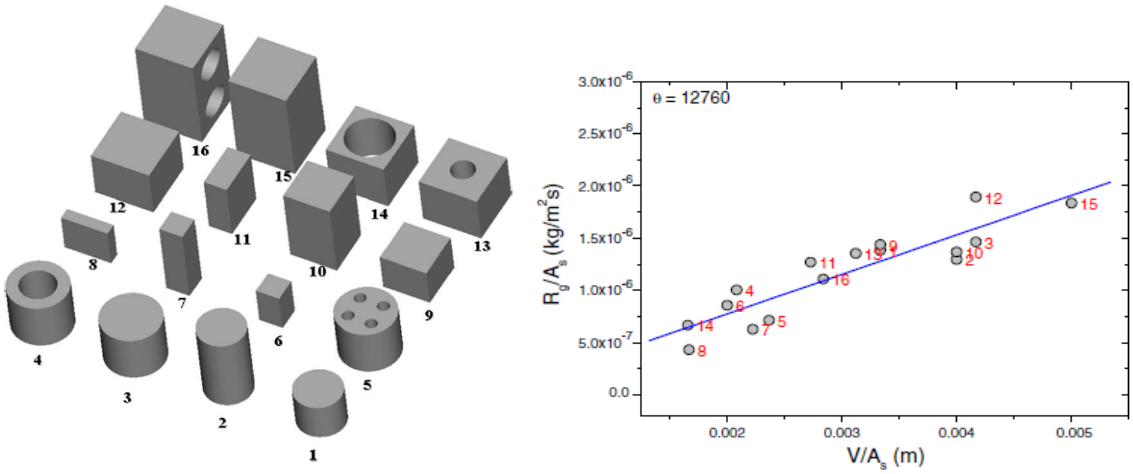

Figure 10. Geometrical effects on IG-110 oxidation rates in air at 600°C. The plot shows the dependence of oxidation rate on the specimen's volume, both being normalized by the geometrical external area.[51]

The effects of sample size and flow conditions have been compared in an attempt to find equivalent oxidation conditions for small samples in commercial thermogravimetric analyzers (TGAs) and large samples in vertical furnaces (VFs) according to ASTM D7542.[50] Experiments at ORNL[52] used a

commercial TGA that accepts samples not larger than 0.3 g. In parallel, measurements were done in a VF built for large specimens (23 g) as recommended by ASTM D7542.[50] Specimens were machined as right cylinders with equal diameter and length (6 mm for small samples, 25.4 mm for large samples). Figure 11 shows that the oxidation rates increased with the air flow rate, more noticeably for the 6 mm samples, which have a larger S/V ratio. The sensitivity to the air flow rate indicates that oxidation was (partially) in the diffusion-controlled regime (Regime 2). However, the Arrhenius plots were linear, and the activation energy calculated between 600°C and 750°C did not vary more than 5% between the VF and the TGA setup.

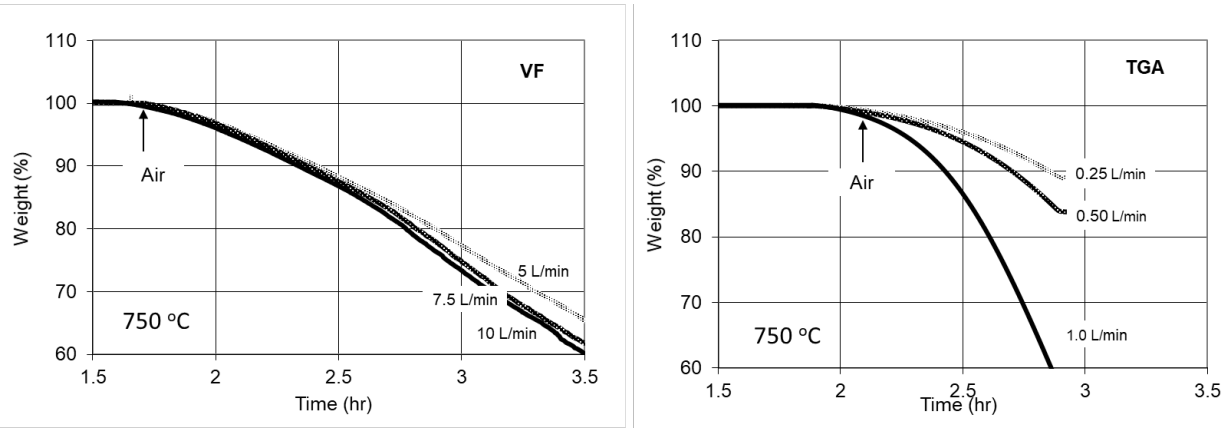

Figure 11. Effect of air flow rate on oxidation rates. Data were measured (left) in a VF using large (23 g, 25.4 mm) specimens and (right) in a commercial TGA using small (0.3 g, 6 mm) graphite samples. Temperature was 750°C in both cases. (Authors' data; more information available in ref.[52])

Another study[53] used the VF setup recommended by ASTM D7542 [50] but varied the air flow rate between 10 L/min (recommended by D7542) and 1 L/min. The results for NBG-17 and NBG-25 (Figure 12) demonstrate the positive effect of flow rate at constant temperature. At low temperatures (Regime 1 at 600 °C) oxidation rates do not vary with air flow rate. At intermediate temperatures (Regime 2, 700–800 °C) oxidation rates become insensitive to air flow rates higher than above some threshold, whereas at very high temperatures (Regime 3, 900–1100 °C) flow rates up to 10 L/min are not sufficient to produce a plateau of oxidation rates.

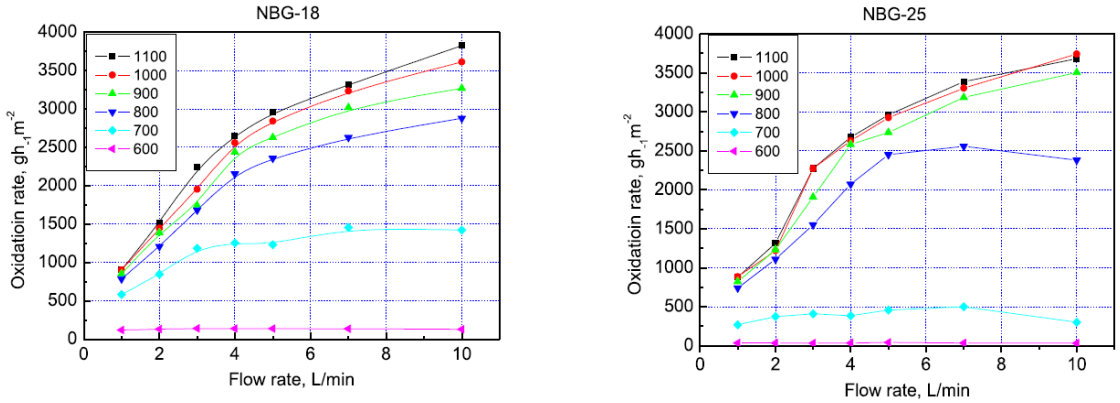

(a) (b)

Figure 12. Effects of air flow rate and temperature on oxidation rates of graphite NBG-18 and NBG-25. Specimens had the standard size and shape recommended by ASTM D7542.[53]

More evidence on the effect of air flow rate on transition temperatures between Regime 1 (chemical control) and Regime 2 (in-pore diffusion control) is provided in Figure 13**.** Oxidation rate data for graphite IG-110 provided by different authors[42,54,55,56] are compared in Arrhenius coordinates. The measurements were made on laboratory-sized specimens, about 3–4 g each, with one exception[56] with larger samples (11 g). At the lowest air flow rate (0.02 L/min), the transition temperature between Regimes 1 and 2 is 600 °C.[54] With slightly larger air flow rate (0.05 L/min), the transition is observed at 700–750 °C.[55] At an even higher flow rate (0.5 L/min), oxidation continues in the chemically controlled regime well above 750 °C.[42] With a much higher air flow supply (40 L/min), transition to Regime 2 occurs at 900 °C.[56] The factor that differentiates these experiments is the ratio between the oxygen supply rate (mmol O_2/min) and carbon gasification rate at the transition temperature (mmol C/min). An empirical analysis shows that the transition occurred when that ratio became lower than a threshold value (approximately 10 ± 5).[52]

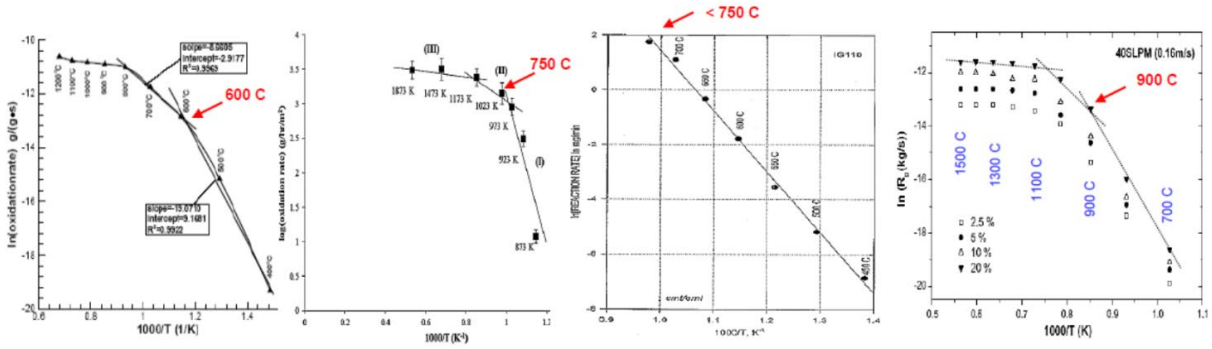

Air flow rate:	0.02 L/min	0.05 L/min	0.5 L/min	40 L/min
Ratio O_2/C oxides:	9.8	13.9	7.6	11.9
Sample size:	1 cm *D* × 1 cm *H*	1.2 cm × 1.2 cm × 1.2 cm	0.8 cm *D* × 1.9 cm *H*	2.1 cm *D* × 3.0 cm *H*
Reference:	54	55	42	56

Figure 13. Effect of air flow rate on the transition temperature between Regimes 1 and 2. Oxidation rates of IG-110 by air are plotted in Arrhenius coordinates. The plots were extracted from references.[42,54,55,56] The ratios of oxygen supply to carbon gasification rates calculated by present authors at the respective transition temperatures of each data set are indicated. The specimens were either cylinders (with diameter *D* and height *H*) or cubes.

4.2.3 Experimental Techniques for Characterization of Graphite Oxidation Behavior

Oxidation behavior can be studied by direct or indirect measurements. If reaction rates are fast enough to allow data collection in a reasonable amount of time, direct rate measurements may be performed in conditions that mimic acute oxidation by air (oxygen) or by steam (water). These measurements would provide information for modeling of unlikely events of air or steam ingress accidents. Measurements of extremely slow rates at very low concentrations of H_2O and CO_2 are more difficult. These experiments are relevant for chronic oxidation behavior during normal operation conditions. Real-time measurements in conditions of chronic oxidation are extremely challenging because mass changes are so very slow. For these processes, kinetic measurements must use accelerated oxidation conditions at higher oxidant concentrations, higher temperatures, or both.[35]

The main types of oxidation rate measurements that can be used when oxidation is sufficiently fast (conditions simulating acute oxidation) are listed as follows. Only the continuous gravimetric method provides reproducible and repeatable results between various workers and different experimental setups.

- The continuous gravimetric method in the VF recommended by ASTM D7542[50] uses cylindrical specimens with standard size (*D* = *H* = 25.4 mm; about 23–25 g) hanging in a vertical tube furnace from the under-scale measuring port of an analytical balance placed on top of the furnace and thermally insulated. A constant flow of dry air from the bottom (10 L/min) must ensure that the

oxygen supply rate much higher than the carbon gasification rates, even at the highest test temperatures. After raising the temperature in a flow of inert gas (dry nitrogen) and stabilization at the desired test temperature, the inert gas is switched to dry air, and mass changes at constant temperature are recorded continuously. During isothermal oxidation, the rate of mass change increases gradually (during the so-called transient, or onset period) and remain approximatively constant between about 5 % and 10 % (and beyond) overall mass loss (the so-called steady state oxidation period).[57] The mass change rate between 5 % and 10 % mass loss is used to calculate the oxidation rate at the selected times the rates may continue to increase very slowly up to a maximum at 35–40 % mass loss and then would drop until all material is consumed.[42,31] Stable rates between 5 % and 10 % mass loss measured at different temperatures are used to the calculate apparent kinetic parameters by plotting the data in the coordinates of the Arrhenius equation:

$$Rate = A \exp\left(-\frac{E_a}{RT}\right) = k_0 \exp\left(-\frac{E_a}{RT}\right) {P_{O2}}^n \,. \tag{8}$$

Semilogarithmic plots of ln (*Rate*) versus 1/*T* should be linear if the selected temperatures are appropriate for the chemically controlled regime. The apparent activation energy E_a and the pre-exponential factor *A* are calculated from the slope and intercept of Eq. (8). The apparent pre-factor *A* includes the oxygen pressure and the frequency factor k_0,

$$A = k_0 {P_{O2}}^n \,. \tag{9}$$

The reaction order, *n*, may be determined by replacing air with synthetic O_2–N_2 mixtures with variable O_2 partial pressures. However, that is not necessary if the only purpose of experiments is comparing and selecting various graphite grades based on their oxidation resistance, as recommended by ASTM D7542.[50] This standard test method is also recommended for evaluation of graphite-specific kinetic parameters characterizing oxidation in Regime 1 (chemical control). The values of *A* and k_0 (but not of E_a) depend on the method used for oxidation rates normalization. Practice has shown that oxidation is mainly uniform in the kinetic regime (although scrutiny may occasionally discover slightly nonuniform density profiles in specimens oxidized at the upper end of the temperature range selected for the kinetic regime).

- The discontinuous gravimetric method supported by ASTM C1179[58] uses cylindrical specimens with standard size (*D* = *H* = 25.4 mm, about 23–25 g) placed in a muffle furnace for 100 hours. No provisions are made to ensure consistent air flow supply in the furnace. Every 25 h, the specimens are removed, cooled in a desiccator, and weighed. Oxidation rates at the designated temperature are calculated from the percent mass loss at 25, 50, 75, and 100 h. The method is recommended for samples that yield less than 10 % mass loss in 100 h by slow oxidation at low temperatures (recommended range 371–377 °C). Because the air flow rate is not controlled, the results can be affected by large errors (including operator errors).

- The continuous method using commercial thermogravimetric (TGA) equipment is limited to small size specimens that can fit the available TGA system. Another limitation comes from the fact that the air flow rate in commercial TGAs is usually not higher than 0.2–0.5 L/min, which is not sufficient for ensuring a large enough air supply rate needed to sustain fast oxidation rates at high temperatures. Most of these studies using commercial TGA equipment could not avoid oxidation-starving conditions at high temperatures or with synthetic gas mixtures with less than 21 % O_2. The TGA results so obtained may "simulate" oxidant starving conditions that may occur during limited air ingress accidents, but their use as a basis for development of design-specific engineering models requires additional justification.

- The continuous gasification method uses indirect gas analysis measurements to calculate oxidation rates, rather than direct measurements from mass changes. These measurements rely on effluent gas analysis (CO and CO_2 for oxidation by air; CO, H_2O, and H_2 for oxidation by moisture) and calculate oxidation rates indirectly using flow rate values and mass balance equations. Gas analysis can be performed either by gas chromatography (GC), mass spectrometry (MS), or infrared spectroscopy (FTIR). The accuracy of results in each technique depends on preliminary quantitative calibrations with standard compounds. One complicating factor is that the hot exhaust gas from the furnace must be cooled to near room temperature before analysis by GC. In the cooling segment, the gas composition is expected to change from that in the hot furnace as dictated by minimization of Gibbs free energy of gas mixture (containing CO, CO_2, H_2O, and H_2) with the drop in temperature. Thus, the gas composition measured by the analyzer (GC, MS, FTIR etc.) does not necessarily correspond to the gas composition near the oxidizing graphite specimen. This is a source of potential errors in mass-balance calculated oxidation rates and misinterpretation of reaction mechanisms, which may have been the case with a recent report in which the effluent gas composition measured by GC was clearly different from that in the reaction space.[59] Similarly, GC analysis of effluent gas from oxidation by moisture may be affected by homogeneous gas phase oxidation by H_2O of CO to CO_2 and may lead to misinterpretation of reaction rates and mechanisms.[60]

4.2.4 Graphite Oxidation Behavior and Safety Implications

Graphite oxidation is a *local process*. It proceeds from the external graphite surface inward into the bulk. The result is a nonuniform distribution of local properties in graphite (density, porosity, mechanical and thermal properties). Weight loss caused by oxidation is a *local property*, as well. The gradient and spatial extent (penetration depth) of graphite density distribution near the exposed surface must be known for evaluation of property degradation caused by oxidation. Safety analysis of HTGRs is part of the licensing process. The effects of oxidation after an unlikely accident depend on the gravity of postulated initiating events and the boundary conditions of design parameters. The off-normal transient events are classified based on their expected occurrence frequency in three categories:[2]

- Anticipated events (AEs) with a probability of less than 10^{-2} per plant-year (maximum once in a lifetime). Examples include a small steam generator leak that introduces about 1 kmol (18 kg) water in the coolant, or a small breach (1 in^2) of the helium barrier causing about one hour of He depressurization. Both events cause minor graphite oxidation and have no radiological effects.[2]

- Design based events (DBEs) with very low frequency (10^{-2}–10^{-4} per plant-year). These are the most serious accident conditions for which the designer must plan and provide mitigation actions. Some examples include larger steam ingress over several hours, or depressurized loss of forced cooling (DLOFC) with air ingress over several days.

- Beyond design basis events (BDBEs) which are extremely unlikely (10^{-4}–5×10^{-7} per plant-year). These are still included in safety analysis to theoretically evaluate the system response to variations of event boundary conditions.[2]

Such accidents are analyzed using various computer codes that describe the reactor's behavior (neutronics, thermal-hydraulic, fluid dynamics). Additional modules should describe graphite behaviors, such as oxidant transport and chemical attack, heat generation, and consequent degradation of properties in various accident scenarios. Because oxidation behavior depends on temperature, oxidant supply rate, and graphite properties, detailed graphite oxidation analysis must be carried out to estimate the weight loss (or density) profile with distance from surface inside the graphite structures. Analysis should consider anticipated ranges (as defined by the qualification envelope) of oxidative conditions (impurity content, temperature ranges) that may cause

chronic oxidation during reactor's normal operation. Analysis should also include various scenarios of accidental water or air ingress that may trigger large-scale acute oxidation.

Although several full-scale graphite oxidation experiments[31,61,62] have been conducted to reproduce (as close as possible) acute oxidation conditions, it is difficult to extrapolate their findings to all postulated situations that would involve air or steam ingress. Developing complex computer codes that integrate graphite corrosion models, air flow, and temperature distribution for experimental situations is more productive and efficient. Experiment-to-code validation and code-to-code comparisons have been generally successful, although more research is still needed.[63] Along with CFD calculations, graphite oxidation and corrosion models are main components of these codes. To provide reliable information, graphite oxidation models must rely on accurate information on graphite behavior, obtained from carefully planned oxidation experiments. The simulation of oxidation behavior should be followed by assessment of degradation of material properties. It should never be lost from sight that graphite oxidation and its effects (weight loss, density changes, various thermal and mechanical properties) are *local*. The models must indicate **when**, **where**, and **how much** *local* graphite damage would be caused by oxidation under various initially postulated scenarios.

Anticipating the information provided in the following chapters, it is appropriate to disclose that most acute oxidation simulations indicate that graphite damage would be more severe for the graphite elements at the reactor bottom during a postulated air or water ingress.[2] Simulations also show that chronic oxidation will have extremely limited effects and will not be a cause of concern.[33]

4.2.5 Chronic Oxidation during Normal Operation

4.2.5.1 Oxidation by water traces in the helium coolant

Although the chemistry of the He coolant in HTGRs will be very well controlled during normal operation conditions, small amounts (i.e., traces) of oxidizing impurities may still be present.[64] Water (moisture) is ubiquitous and the most difficult impurity to remove; it may be introduced during reactor's revisions or refueling. Most sources estimate that the H_2O concentration under normal circumstances will be less than 1 ppm for a total pressure of maximum 7–9 MPa (or about 1.1–1.4 Pa in absolute pressure values).[65] During several decades of service life, graphite components in the reactor (fuel elements, moderator, reflector, support posts) will certainly undergo an extremely slow but continuous (chronic) oxidation:

$$C_{\text{graphite}} + H_2O_{\text{vapor}} = CO_{\text{gas}} + H_{2\ \text{gas}}$$

Several excellent reviews on the kinetics and mechanism of this reaction are available.[4,66] Oxidation becomes observable starting from approximately 800 °C. The overall reaction rate increases exponentially with the temperature (a trend often described by the Arrhenius equation) and with the partial pressure of water vapor (P_{H2O}) and decreases with the partial pressure of hydrogen (P_{H2}), which is a reaction product. This behavior indicates that the mechanism of the overall reaction consists of several elementary steps (of which there is currently no general agreement), which, in combination, lead to the following formal rate equation:

$$Rate_{LH}(P_{H2O}, P_{H2}, T) = \frac{k_1 P_{H2O}}{1 + k_2 (P_{H2})^n + k_3 P_{H2O}}, \tag{10}$$

which characterizes the Langmuir–Hinshelwood (LH) reaction mechanism.[67] The dependence of individual kinetic constants k_i on temperature is formally described by the classical Arrhenius equation,

$$k_i = k_{i0} \exp\left(-\frac{E_i}{RT}\right), \tag{11}$$

where E_i are apparent (model- and circumstances-dependent) activation energies. The pre-exponential factors A_i are identified with frequencies of elementary events (also dependent on circumstantial factors). The exact mechanistic signification of individual parameters is not clear because the composite constants k_i depend on the assumed formal elementary steps mechanism. A probabilistic treatment of these elementary kinetic parameters (devoid of any association with elementary reaction steps) was proposed as a convenient tool for engineering simulations.[65]

Chronic oxidation by trace impurities in the helium coolant is unavoidable during a reactor's multidecade service time. It will have two predictable effects: (1) gases such as CO (toxic) and H_2 (flammable) will be generated in the coolant, but these impurities will be continuously removed as the coolant's chemistry is continuously controlled; and (2) slowly but surely, oxidation will corrode the surface of fuel elements and other core graphite components, locally weakening their mechanical strength. The questions are how deep this corrosion will penetrate, and whether that might jeopardize the reactor's integrity.

Numerous simulations[34,45,68,69,70,] show that chronic oxidation is not a real concern for reactor's safety because it will be very localized, and its effects will be spatially limited. Using General Atomics data[32] on moisture oxidation kinetics of graphite H-451, Richards calculated[68] that chronic oxidation by moisture will affect only a thin layer (1–2 mm) below graphite's surface, on the condition that water concentration in the coolant does not exceed 0.1 ppm at a total pressure of 6.3 MPa (or 0.6 Pa partial pressure). This calculation favorably compared with density profile measurements near the surface of graphite 2020 oxidized by water.[68] Simulations were performed for various water pressures at temperatures above 500 °C and 5 MPa total helium pressure. The results showed that most of the oxidation will occur at the bottom of the reactor. The local mass loss in the bottom three blocks may reach up to 8 % within a thickness not greater than 0.8 mm for the most oxidized blocks. The graphite microstructure is expected to play a significant role by affecting the diffusion of oxidant. The oxidation rates increase with service time because of the development of porosity. These changes may affect the lifetime of components, especially of those irreplaceable components in the reactor's basement, which are designed to last the reactor's entire lifetime.[68]

To provide information on specific graphite grades, a research program was recently carried out at ORNL to investigate oxidation behavior of four nuclear graphites (including PCEA and IG-110) in He with various amounts of H_2O and H_2.[33, 35,65,71,72] Through accelerated oxidation tests, this program obtained oxidation rate information and monitored the effect of temperature ($850 < T$ (°C) < 1100) and partial pressures of water and hydrogen ($3 < P_{H2O}$ (Pa) < 1000; $0 < P_{H2}$ (Pa) < 100) on oxidation rates. In addition, the penetration depth of the oxidized layer was characterized for specimens oxidized at various conditions. The rates generally followed the classical Langmuir–Hinshelwood (LH) kinetic mechanism at low pressures and temperatures but deviated from that model at higher temperatures and moisture concentrations. This is illustrated in left side panel of Figure 14, where the experimentally measured oxidation rates for four graphite grades at various temperatures and water partial pressures are compared against the best fit using the LH model. An improved kinetic model (Boltzmann-enhanced Langmuir–Hinshelwood, or BLH) was proposed,[71] which more accurately simulates experimental results, especially at the high end of T and P_{H2O} parameters. This shown in the right-side panel of Figure 14 where the same data are compared against the best fitting using the BLH model. In essence, the modified BLH model allows for the temperature dependence of the apparent reaction order for H_2O in the reactions with carbon:

$$M\,C_{(s)} + m\,H_2O_{(g)} = m\,CO + m\,H_2 + (M - m)\,C_{(s)}$$

where $M >> m$, and $m = m(T)$ represents the reactive surface sites able to react with H_2O at various experimental conditions (a temperature-dependent function).[33] With this modification, the BLH rate equation becomes

$$Rate_{BLH}(P_{H2O}, P_{H2}, T) = \frac{k_1(P_{H2O})^{m(T)}}{1+k_2(P_{H2})^{0.5}+k_3(P_{H2O})^{m(T)}}\,, \tag{12}$$

where kinetic constants have the Arrhenius dependence of Eq. (11), and the kinetic order $m(T)$ is described by a sigmoid function:

$$m(T) = m_{max} - \frac{m_{max}-m_{min}}{1+exp\left(\frac{T-T_0}{\theta}\right)}\,. \tag{13}$$

In addition, by corroborating kinetic data with graphite-specific effective diffusivity parameters,[73] the Wichner model[74,75] for transient chronic oxidation evolution was validated for each of the four examined grades of graphite.[76] The main conclusions of this research campaign are as follows:

- Maximum penetration depth of oxidant decays exponentially with the increase of oxidation temperature; the rate of decay depends on the effective diffusivity of water from H_2O/He mixtures, which is determined by graphite microstructure.
- Hydrogen slows down (inhibits) oxidation by water by blocking reactive carbon sites on graphite.
- The LH model can adequately describe oxidation by low-pressure moisture in accelerated tests relevant to normal operation conditions.
- A subsequent experiment showed that the BLH model can simulate steam ingress conditions up to 1600 °C and 50 kPa H_2O.[77]

These ORNL results[76] were used in a full-scale multiphysics simulation of chronic oxidation by moisture of graphite channels in fuel elements during normal operations in HTGR.[60,78] The LH model was preferred over the BLH model for analysis of continuous chronic oxidation for 36 months. Information on the multiphysics model is provided in Section 6.2.9.

Specific information on oxidation of graphites IG-110 and NBG-18 by steam are available in subsection 4.2.6.2. However, chronic oxidation by parts per million concentrations of moisture that might be present in the helium coolant is not considered a safety concern for HTGRs, as long as the actual operating conditions (e.g., concentration of oxidizing impurities, temperature) are within the design parameters envelope for normal operation conditions.

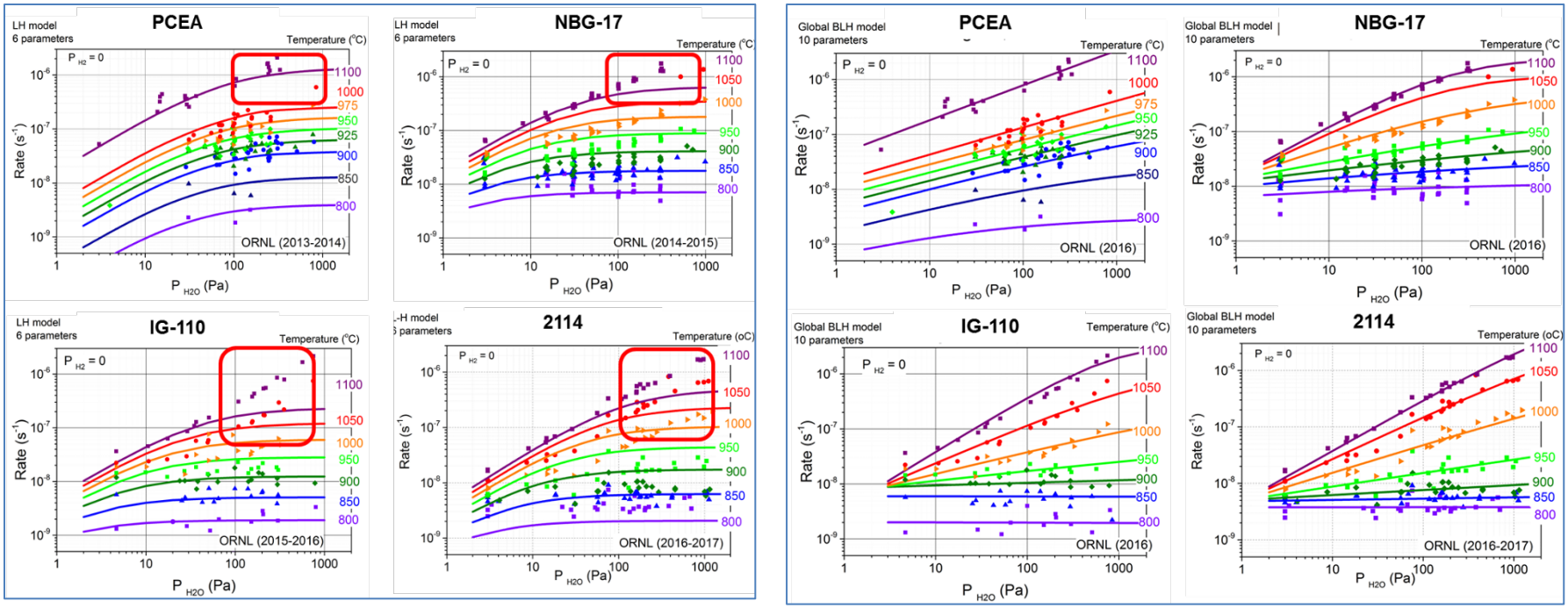

Figure 14. Accelerated oxidation test results of oxidation by moisture of four graphite grades. Best fits of authors' experimental data with (left) the LH model and (right) the BLH model are shown for each graphite grade. (Authors' data; more information available in ref.[76])

4.2.5.2 Oxidation by carbon dioxide traces in the helium coolant

Carbon dioxide oxidizes graphite only three times slower than water at 800°C and at comparable pressure conditions.[4]

$C_{\text{graphite}} + CO_{2\ \text{gas}} = 2\ CO_{\text{gas}}$

This reaction's kinetics obeys the LH mechanism,[79] and the formal rate equation is similar to that for oxidation by water:

$$Rate_{LH}(P_{CO2}, P_{CO}, T) = \frac{k_1 P_{CO2}}{1+k_2(P_{CO})^n+k_3 P_{CO2}}\,. \quad (14)$$

The individual kinetic constants k_i are formally described by Eq. (11) introduced above.

In the absence of ionizing radiation, oxidation by CO_2 becomes measurable from about 650 °C.[66] This reactivity sets the limit for the maximum temperature of the graphite core in CO_2-cooled advanced gas reactors operating in the United Kingdom. In addition to thermal oxidation by CO_2, AGRs also face a complicated gas phase chemistry derived from CO_2 radiolysis and ionization by gamma radiation. The ensuing radiolytic graphite oxidation develops porosity and reduces the strength of in-core graphite components.[80]

These complications will not arise in HTGRs because the coolant is high-purity He. Removing CO_2 from helium is easier (because of CO_2 chemical properties) than removing H_2O traces. Despite formal kinetic similarities with oxidation by moisture, graphite chronic oxidation by CO_2 during normal operation is not considered a factor of safety concern for HTGRs and VHTRs.

4.2.6 Acute Oxidation during Off-Normal Transient Events

4.2.6.1 Acute oxidation by air

Oxidation of graphite by air becomes measurable from about 450–500 °C, and the rate increases quickly with temperature. As mentioned in the Introduction, at 800 °C and 10 kPa O_2 partial pressure (0.1 atm), the rate of carbon reaction with O_2 is about 100,000 times faster than the reaction with CO_2 in the same conditions.[4] Several reactions are possible between carbon and oxygen, as shown below:

$C_{\text{graphite}} + O_{2\ \text{gas}} = CO_{2\ \text{gas}}$

$C_{\text{graphite}} + \frac{1}{2}\ O_{2\ \text{gas}} = CO_{\text{gas}}$

$CO_{\text{gas}} + \frac{1}{2}\ O_{2\ \text{gas}} = CO_{2\ \text{gas}}$

The composition of gasification products changes with temperature and total pressure, as determined by the chemical equilibrium of the global reaction:

$2\ C_{\text{graphite}} + CO_{2\ \text{gas}} = 2\ CO_{\text{gas}}$

Below approximately 700 °C, CO_2 prevails, whereas CO is the major product at higher temperatures.

At room temperature, the graphite surface (and of most carbon materials) contains chemisorbed oxygen and hydrogen that satisfy dangling bonds of edge C atoms of graphene sheets or at other defective C atoms configurations exposed to gas access. At room temperature, they form either stable >C–H bonds or

oxygenated functions, such as phenols (>C–OH), ketones (>C=O), and carboxyls (–COOH). The terminal and defective carbon atoms holding these chemical functions are the active sites that may participate in oxidation reactions. Together, they form the active surface area (ASA) of carbonaceous materials. ASA is a subset of total surface area (TSA), which is usually calculated from N_2 adsorption at 77 K using the Brunauer–Emmett–Teller (BET) method.[81] The other subset of TSA is the basal plane area (BPA) representing the totality of carbon atoms packed in hexagonally ordered basal plane surfaces exposed to gas access. Basal planes are the most stable surfaces in graphite; they do not (initially) participate in oxygen chemisorption and gasification reactions and can be quantified by high-resolution gas adsorption measurements.[82] With the increase of temperature, the oxygenated functional groups are broken and release H_2O, CO_2, or H_2 (in that order) in temperature-programmed desorption (TPD) experiments. The newly formed dangling bonds at the remaining terminal carbon atoms may be reactive enough to reoxidize and continue graphite gasification. They form the reactive surface area (RSA), which is the temperature-dependent reactive subset of ASA.[83,84]

Graphite oxidation is a heterogeneous gas–solid reaction in which the (re)active sites are in internal porosity, and their access by oxygen is retarded by transport limitations. Transport-limited reactions are frequent in heterogeneous catalysis and in chemical engineering. However, in graphite oxidation, the structure of the porous solid itself changes during the reaction progress. Pores are created, enlarged, and then collapsed as the graphite material is being gradually oxidized. This continuous evolution of the structure is a serious complicating factor for all modeling attempts.

Figure 15 shows an example of oxidation rate data of electrode-type graphite plotted in Arrhenius coordinates over a broad range of temperatures.[85] The plots are linear at low temperatures (Regime 1), but on increased temperature, they deviate from linearity (Regime 2), go through a flat "saddle" between about 900 and 1200°C (Regime 3), and then accelerate again at extremely high temperatures. The range of extremely high temperatures (from about 1200 to 1500 °C) where oxidation rates continue to increase before they apparently stabilize again (above 1500 °C) is noteworthy because temperatures in this range may occur in the reactor core in the case of a loss of cooling accident, which is a DBE.[86,87] Unfortunately, information on graphite behavior in the extremely high-temperature regime is currently limited.[88,89]

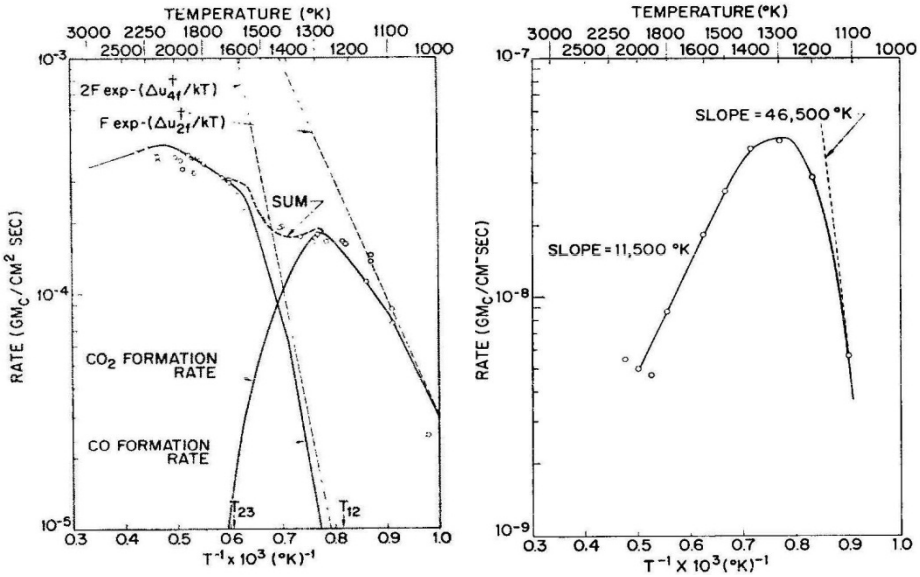

Figure 15. Experimental rate data on oxidation of electrode-type graphite by air. Data at 0.21 bar O_2 (left) and at 10^{-6} bar O_2 (right) are plotted in Arrhenius coordinates.[85]

4.2.6.2 Acute oxidation by steam

There is an acute lack of information on kinetics of nuclear graphite oxidation by steam at conditions relevant to steam ingress accidents. In the 1960s, when the experimental gas-cooled reactor (EGCR) project was conducted at ORNL, a specially designed facility for graphite-steam reactions was built (Figure 16) and used for oxidation studies of two graphite grades designed for fuel elements and moderator.[90] The steam pressures (3.5 to 20.6 bar) and temperatures (700 to 870 °C) of the experiments did not match the steam ingress scenario in the HTGR,[91] but the information is still useful. For example, Figure 16 shows that at these high steam pressures, oxidation rates at various temperatures continue to follow the Arrhenius equation. Furthermore, the linear plots shift upward with the increase of the burn-off, but with different slopes for each graphite. This suggests that the oxidation mechanism in high-pressure steam is similar with oxidation by air: the rates increase with the development of porosity as the reaction progresses, whereas the apparent activation energy is relatively constant; however, the temperature regimes are different.[90]

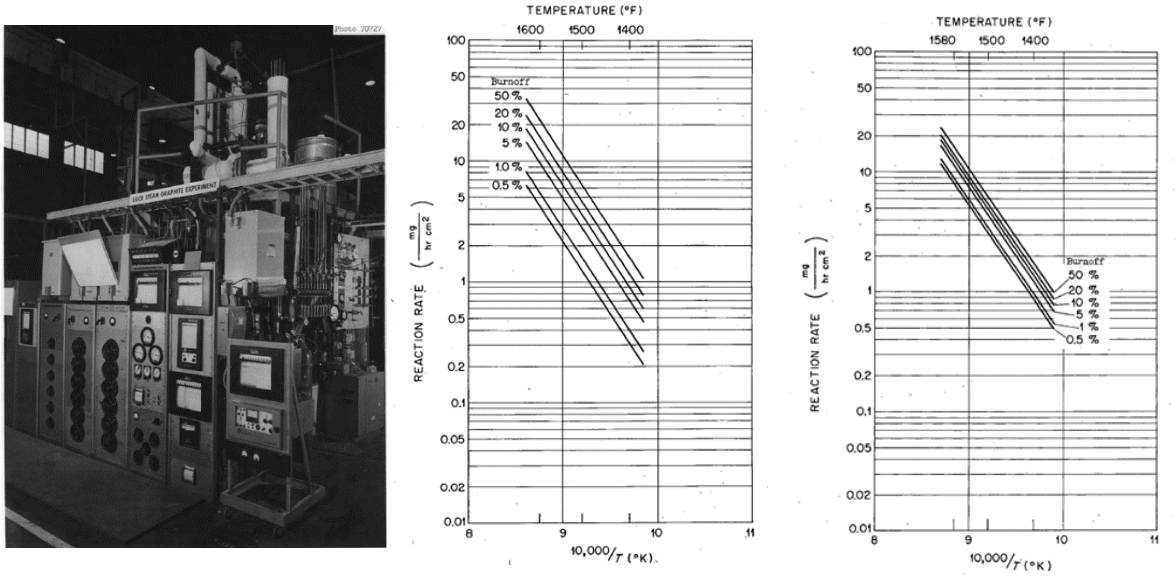

Figure 16. Historic steam-graphite facility at ORNL and early experimental results. Experimental station (left) and temperature variation of oxidation rates with steam of graphite materials selected for fuel elements (center) and moderator (right).[90]

Unfortunately, very little new information was subsequently published on graphite acute oxidation by high-pressure steam. Most of the experimental investigation of graphite oxidation by moisture explored conditions relevant to normal reactor operation, namely low water partial pressure and low temperatures. However, safety analysis based on high-pressure steam ingress continued, prompted by the development of a 200 MWe high-temperature reactor–pebble bed modular (HTR-PM) in China. Because of the lack of experimental data on graphite oxidation by high-pressure steam, the results of such analyzes missed detailed information regarding possible accident consequences. For example,[92] water ingress analysis following two accident scenarios (double-ended guillotine break of a steam generator heating tube, and a large break of the main steam collection plate) concluded that, in the first 100 hours, the amount of graphite reacted would be 23 kg in the first case and 76 kg in the second case. Because these amounts are minor compared with the total amount of graphite present in the reactor (83 t in fuel elements and 330 t in the graphite reflector), it was concluded that the steam ingress would have no significant consequences.[92] This global analysis did not consider the fact that oxidation is localized. If the tens of kilograms of graphite removed by oxidation were all concentrated in a sensible spot of reactor's structure, the reactor's physical integrity might have been affected.

This example emphasizes again the need for detailed oxidation analysis based on oxidation kinetics, oxidant transport, and reactor configuration. Such an analysis was performed by Richards,[69] who used the REACT-COMPACT computer code to model graphite corrosion in steam-ingress accidents. The model used the quasi-steady form of the conservation equation for water vapor (steam) in graphite pores[68] and the LH kinetic constants for graphite H-451 reaction with water.[32] A corrosion experiment of graphite 2020 in H_2O (9090 ppm)/H_2 (445 ppm)/He (balance) at 5.5 MPa was used for validation of calculated density profiles in oxidized graphite against experimental values.[68] Figure 17 shows the temperature dependence of graphite mass loss (< 1 wt % at 1000 °C) and the radial penetration distance (a few millimeters) of water vapors in the fuel compact and in the web of fuel element channels at 700 °C.[69] However, these simulations were based on the hypothesis that the LH kinetic parameters characterized for graphite H-451 can be properly transferred to oxidation of graphite 2020 by moisture.

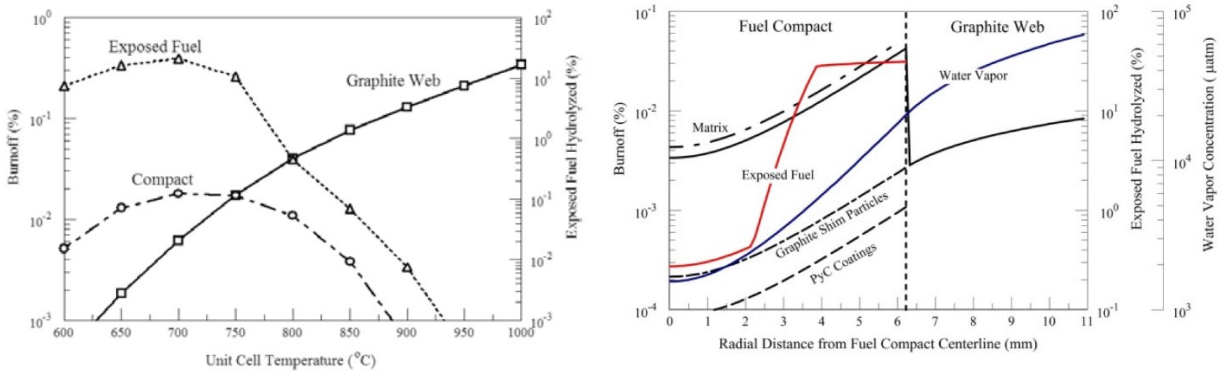

Figure 17. Modeling results using REACT-COMPACT code for steam ingress in an HTGR. Left: Temperature dependence of graphite mass loss in the graphite web after exposure to 7 kPa H_2O and 7 kPa H_2 for 20 h. Right: Penetration depth of H_2O vapor in the fuel compact and in the graphite web exposed for 20 h at 700°C.[69]

Significant progress was made in recent years, when new experimental results and model simulations for oxidation of IG-110 by steam (20 kPa H_2O in argon) were published.[36] Rate measurements at temperatures between 900 and 1400 °C and 1 bar total pressure (100 kPa) showed that oxidation shifted from Regime 1 to Regime 2 at 1100°C. Using the respective rate equations and the Wichner model[74,77] for reactions coupled with diffusion enabled new predictions of water penetration profiles as a function of oxidation temperatures (Figure 18). As expected, oxidation depth was greater at 900°C (4.5 mm) and dropped to < 1 mm above 1000 °C. These predictions were confirmed by direct observations of the oxidized layer.[36]

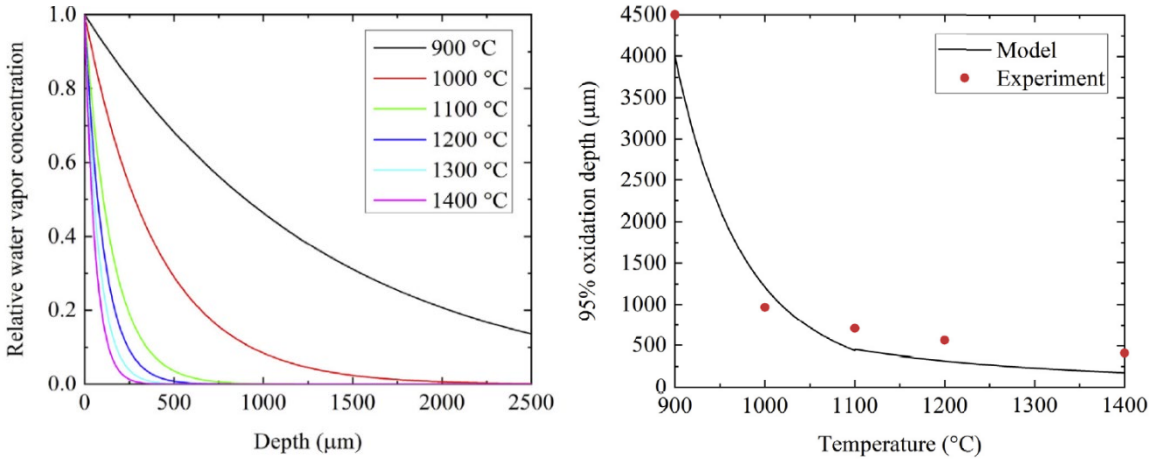

Figure 18. Model predictions for acute oxidation of IG-110 by steam (20 kPa) at 1 bar total pressure.
Left: Effect of temperature on H_2O concentration profiles under graphite surface. Right: Predicted and measured maximum oxidation penetration depth.[36]

4.3 ACUTE OXIDATION BY AIR OF GRAPHITES IG-110, NBG-18, AND PCEA

4.3.1 General Observations

Numerous literature reports are available on oxidation kinetics of nuclear graphites by air. Graphite IG-110 was by far the most studied grade, followed by NBG-18. However, in comparing reports from different laboratories, where different methods were used (see Section 4.2.2 above), it is immediately clear that only a few reports agree with each other. A closer look shows that the concurring results were all measured by the continuous gravimetric method based on ASTM D7542.[50] The discontinuous gravimetric method returned results in partial agreement with the continuous gravimetric method. The other two methods provided divergent results that were in disagreement with the ASTM-based continuous gravimetric method.

In this section, oxidation rates reported by various sources plotted in Arrhenius coordinates will be compared for grades IG-110, NBG-18 and PCEA. Data were extracted from original publications and recalculated for uniform normalization, either by the exposed geometric area of graphite specimens (units of kg h^{-1} m^{-2}) or by the initial graphite mass (units of s^{-1}) in the first two panels of Figures 19–22 and 24. A third plot in the same figures characterizes oxygen supply conditions. The results will be discussed individually for each graphite grade in subsections 4.3.2, 4.3.3, and 4.3.4.

The goal of these studies was to compare kinetic parameters characteristic for oxidation of each graphite grade, and to determine which parameters can reliably be used for oxidation modeling. The basic assumption is that kinetic parameters should be measured in conditions in which oxidation is not perturbed by transport limitations (Regime 1) and is not limited by insufficient oxidant supply. Then, the models could be expanded to incorporate in-pore diffusion (Regime 2) or boundary layer transfer (Regime 3) with the variations caused by size, shape, air flow conditions, and limited oxidant supply. It was empirically found that oxidant-starving conditions can be avoided if the molar ratio of oxygen supply rate (mmol/min) is approximately 10–15 times greater than the carbon gasification rate (mmol/min).[52] The third panel in the Figures 19–22 and 24 shows the evolution of the molar rates ratio as a function of temperature. At constant air flow rate, oxidation rates increase exponentially with temperature, and consequently, the ratio of air supply rate to gasification rate decreases quickly. The process can easily become oxidant-starved with the increase in temperature, in which case oxidation may have already shifted to Regime 3 (boundary layer control).

To separate transport processes (in-pore diffusion and interfacial mass transfer) from chemical effects (oxidation kinetics), the rate parameters must be obtained at conditions in which other perturbations are absent. This is possible by monitoring slow oxidation rates at low temperatures (Regime 1). Only a few research groups have taken the pain of measuring slow oxidation rates at temperature close to 450–500°C in conditions of large rates of oxidant supply. Many more investigated the effects of temperature without ensuring sufficient O_2 supply at high temperatures. In particular, commercial TGAs are limited by their design construction to limited air rate supply. As a result, numerous oxidation rate measurements reached starving conditions, and the results cannot be used for modeling. Some other researchers intentionally reduced the O_2 supply (using synthetic O_2–N_2 mixtures with less than 21 vol % O_2). The goal was to simulate the early stage of air ingress events, where laminar flow conditions (air in and He out) are predicted to last for some time. According to this model, an air ingress accident would never reach 21% O_2 in air. These experiments showed, as expected, that oxidation rates decreased with increasingly starving conditions. The raw data thus obtained may serve as examples for comparison with simulations and validation of complex graphite oxidation models.

Besides air flow rates and temperature, the size and shape of graphite specimens is another influencing factor. Empirical evidence shows that small changes in the surface to volume (S/V) ratio of graphite samples being oxidized do not alter the general behavior, so that data can still be compared between various sources. This is the case for specimens with the standard shape and size recommended by ASTM D7542[50] (25.4 mm *D* and 25.4 mm *H*; S/V = 2.4 cm^{-1}). Small deviations of S/V ratio (e.g., between 2.0 and 2.8 cm^{-1}) seem to have minimal effects on consistency of results from various sources. In general, the smaller is one dimension (diameter for cylindrical rods, thickness for oblate plates), the faster is oxidation in isothermal conditions. A series of tests with S/V ratios in the range of 11.6–11.7 cm^{-1} showed high oxidation rates at temperatures about 200 °C lower than the temperature range recommended by ASTM D7542. Evidently, accounting for size and shape effects is still an open issue for complex oxidation modeling.

4.3.2 Graphite IG-110

The next three figures show oxidation rate data of IG-110 graphite in air, plotted in Arrhenius coordinates. Data were selectively extracted after examination of numerous reports available in the open literature. Each report was analyzed to determine the method used for measurements and the conditions selected, including the size and shape of the graphite specimens. The plots show rate data normalized by either geometric surface or initial mass, along with the ratio of oxidant supply rate to carbon gasification rate.

Figure 19 shows data measured by the continuous gravimetric method according to the conditions of ASTM D7542,[50] including the use of standardized size and shape specimens. Most data were collected with a large excess of O_2 supply to avoid oxidant-starving conditions. The tests performed at Idaho National Laboratory (INL) (Smith 2020),[93] ORNL (Contescu 2011),[94] and the Korea Atomic Energy Research Institute (KAERI) (Chi 2008)[95] followed the ASTM standard method exactly and show very good reproducibility. The results also agree for two other tests performed by the direct mass measurement method using commercial TGAs (Fuller 1997)[42] and (Lee 2014).[55] Two more tests by the discontinuous mass measurement method are in good agreement with the others and provide data over a broader temperature range (Lo 2018)[88] and (Lo 2020).[89] As expected, mass-normalized data (rates expressed in s^{1}) are better overlapped than area-normalized ones, at least in the kinetic regime. Together, these results span a broad temperature range, from 450 °C to 1600 °C, where oxidation changes from Regime 1 to Regime 2 and finally to Regime 3. Except for data collected in Regime 3 with limited air flow in a TGA system (where oxidation was limited by oxidant starvation),[55] the remaining data represent unimpeded oxidation rates and can trustfully be used for calculation of apparent activation energy and pre-exponential factor.

Figure 20 shows all the data from Figure 19**,** along with more data from tests using the gasification method: (Kim 2006)[56] and (Lu 2020).[96] These authors investigated oxidation in Regimes 2 and 3 at high and very

high temperatures, where gasification rates depend primarily on oxygen supply rates and less on temperature. The O_2 supply rates were varied by changing the air flow rate or by using synthetic mixtures with variable O_2 compositions. Take as an example the experiments with He/O_2 mixtures and O_2 content from 20 to 2.5 % at a total flow rate of 40 L/min (the highest rate of all tests with IG-110).[56] All high-temperature data points in Regimes 2 and 3 are shifted upward with the increase of O_2 content in the mixture, as expected. However, data in Regime 1 are systematically shifted with respect to data measured by gravimetric methods. Two sources of errors might explain the deviation. First, temperatures were not measured by thermocouples placed near the sample in the furnace, but by external infrared thermometers. If actual sample temperatures were lower by 60–70 °C, all runs reported[56] by the gasification method would align very well with the results from direct mass and temperature measurements. Second, even though the temperatures were correct, the rates were measured at very low mass loss levels (close to zero).[56] It has been long documented[31,42,57] that transient oxidation rates increase during the initiation period, where ASA increases in parallel with the development of new porosity. Although the apparent activation energy does not vary much with the degree of mass loss, the initial oxidation rates reported by (Kim 2006)[56] were expected to be lower (by at least one order of magnitude) than the rates at steady oxidation conditions (between 5 and 10% mass loss) recommended by ASTM D7542 [50] and reported by others in the kinetic regime.[42,93,94,95] Moreover, these tests by the gasification method may have been perturbed by gas phase reactions (such as CO oxidation to CO_2) in the line between the hot oxidation reactor and the room temperature gas analyzer.[96]

Figure 21 contains the same data as Figure 20, along with additional results from an experiment with an unspecified method (Huang 2014)[97] and two more tests, (Sun 2017)[98] and (Yan 2017),[99] with very thin plate-like graphite specimens (see legend for dimensions). Because of very high S/V ratio (11.7 cm^{-1}), plate-like specimens were oxidized much faster than all other graphite samples with S/V ratios between 2 and 4 cm^{-1}. The thin graphite plates became oxidized at remarkably low temperatures (from 400 °C) if sufficient O_2 supply was provided, but the oxidation drifted soon into starving conditions with the increase of temperature, and the Arrhenius plots became irregular.[98] In these tests not conforming to the standard method, estimation of apparent activation energy from only two data points produced anomalously high values.[55]

In summary, when all data available for IG-110 were plotted together on the same graph (Figure 21**)**, the results were divergent. Only a few independent experimental results support each other, as shown in Figure 19. The divergence of the remaining data (Figure 21) from the narrow cluster of congruent results (Figure 19) can be attributed to two main reasons. First, some of the indirect rate measurements by the gasification method are prone to more sources of experimental errors than direct rate measurements by the gravimetric method. Second, the divergence between results reflects the dependence of oxidation rates on often-overlooked experimental factors, such as shape and size of specimens, the overall flow rate, oxidant partial pressure, and the competition between reaction and transport processes, which are differently influenced by temperature.

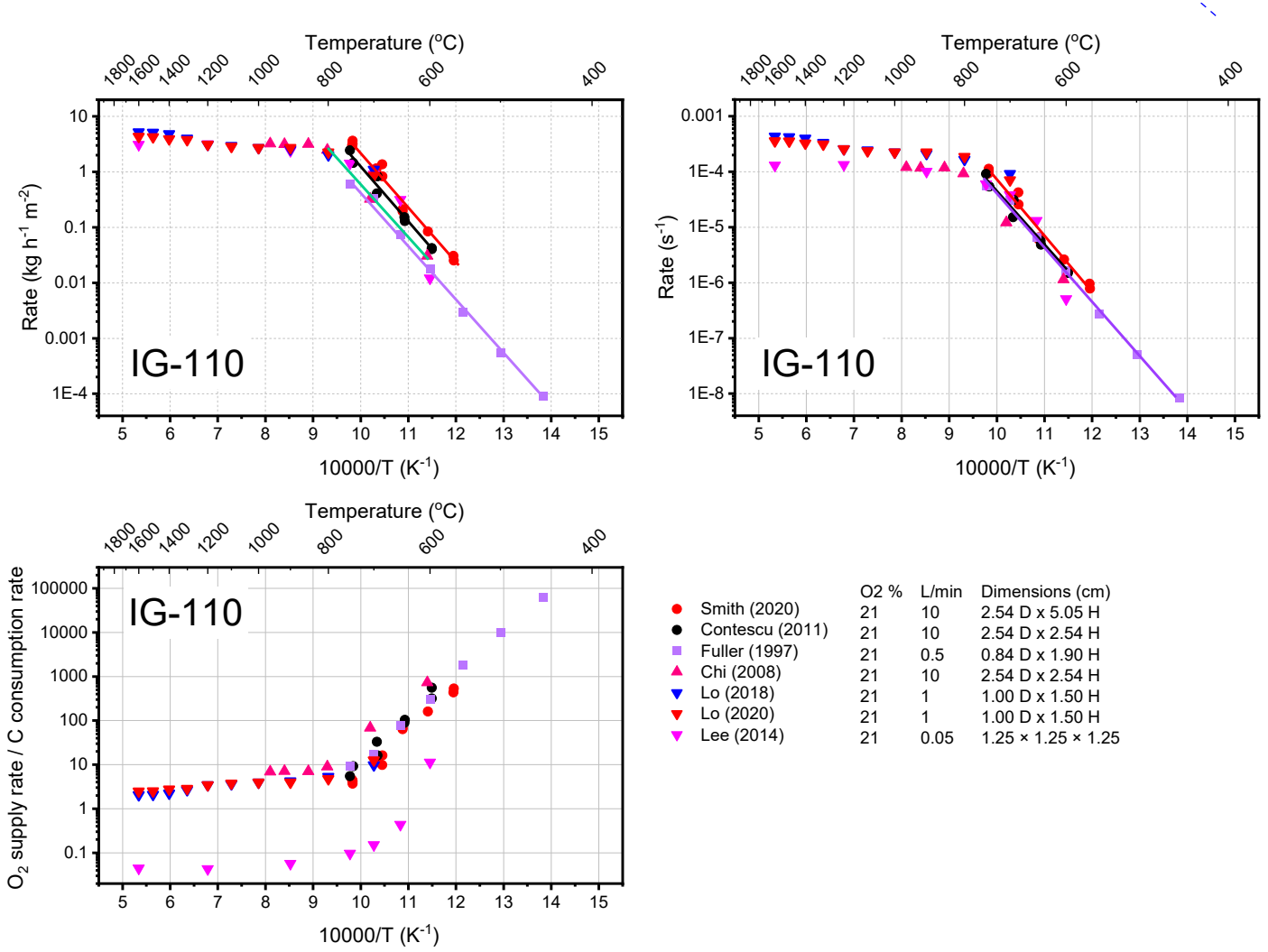

Figure 19. Selected rate data for oxidation of IG-110 by air. Data were measured by continuous gravimetric methods, either in a VF according to ASTM D7542 or in commercial TGA equipment.

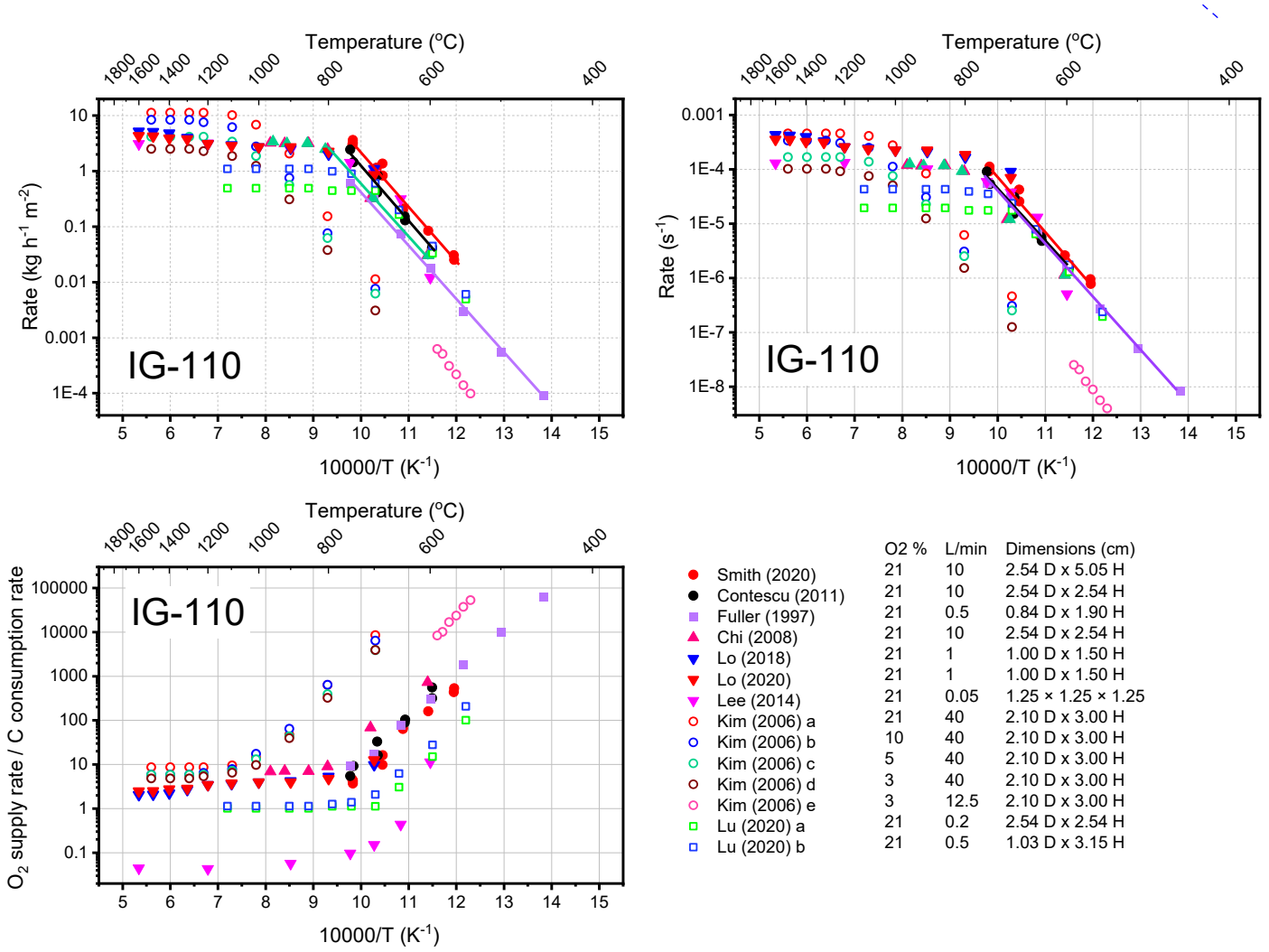

Figure 20. Additional rate data for oxidation of IG-110 by air. Data measured by the gasification method were added to data from Figure 19 (continuous gravimetric methods either in a VF according to ASTM D7542 or in commercial TGA equipment).

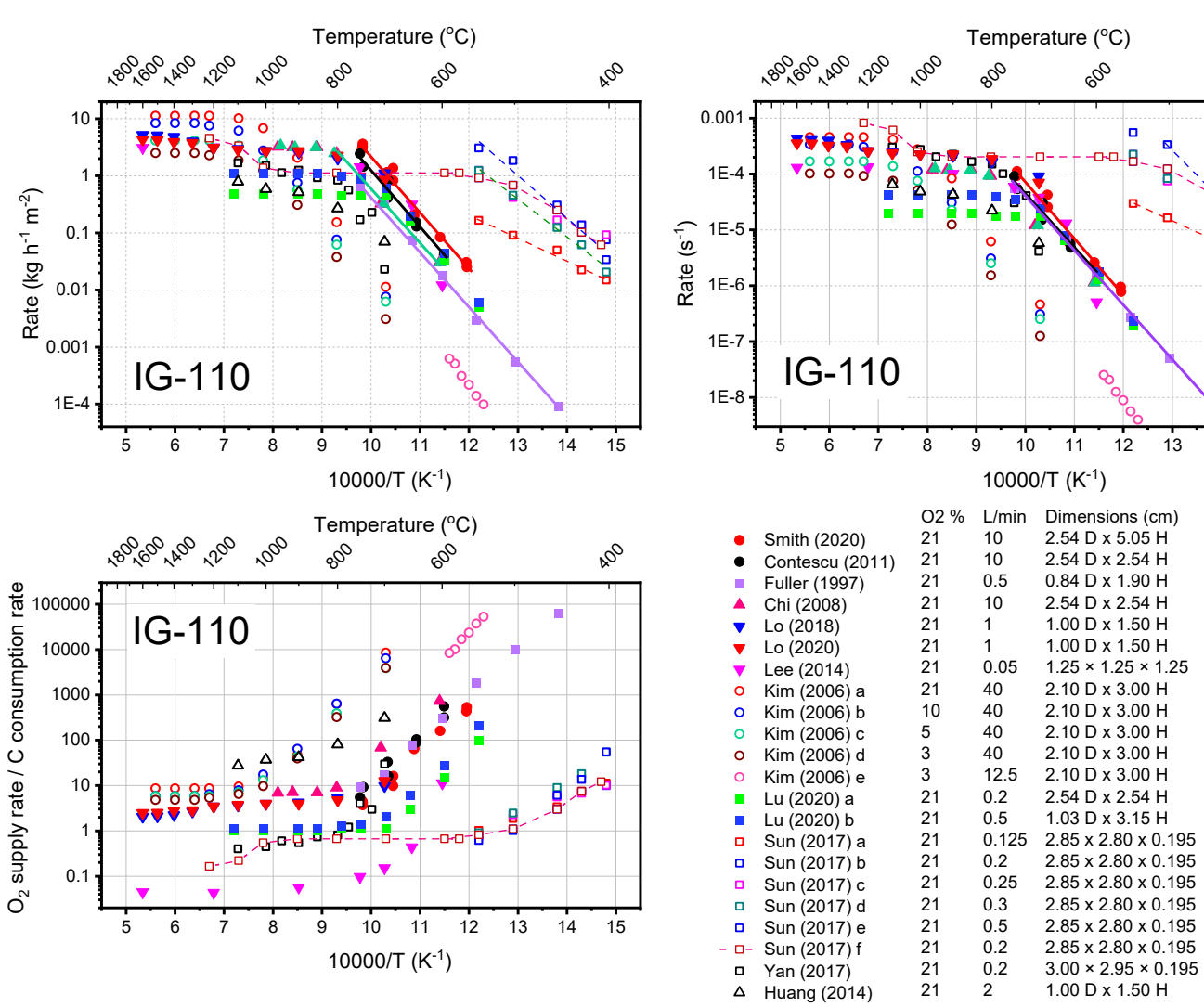

Figure 21. All rate data for oxidation of IG-110 by air. More data for plate-like specimens and oxidant-starving conditions were added to data from Figure 20 (gasification method and continuous gravimetric methods either in a VF according to ASTM D7542 or in commercial TGA equipment).

Table 3 presents a summary of kinetic parameters reported by various sources for oxidation of IG-110 by air. Kinetic parameters were recalculated from explicit numerical collections when available or from the digitized images in Figure 19, but only those data meeting some ad-hoc quality standards were selected for this table. The main purpose of this selection was elimination of results measured in oxidant-starving conditions. Only those data points with an O_2 supply rate at least 10 times higher than the rate of carbon gasification at the respective temperature were considered. A second selection condition was that no calculation of an Arrhenius slope and intercept with fewer than three data points was accepted as meaningful. With these strict selection conditions, some results reported in the literature (present in Figure 19) were not considered reliable and had to be disregarded. This way, the compilation of IG-110 results presented in Table 3 is different from what can be found in other literature sources.[55,101]

Table 3. Selected kinetic parameters oxidation of IG-110 by air

Author	Ref.	Activation energy (kJ/mol)	Preexponent factor ln[A(s^{-1})]	Data points	Temp. range (°C)	Dimensions (cm)	S/V	Flow rate (L/min)	O_2 (%)
Smith (2020)	[93]	195	13.9	9	536–695	2.54 *D* × 5.08 *H*	2	10	21
Contescu (2011)	[94]	191	13.0	6	597–694	2.54 *D* × 2.54 *H*	2.4	10	21
Fuller (1997)	[42]	187	12.5	7	450–750	0.84 *D* × 1.90 *H*	5.8	0.5	21
Chi (2011)	[95]	169	9.5	3	603–808	2.54 *D* × 2.54 *H*	2.4	10	21

Note: For cylindrical specimens, *D* = diameter; *H* = height

4.3.3 Graphite NBG-18

Only a few reports have examined the kinetics of NBG-18 oxidation by air. Most of the data plotted in Figure 22 were measured by the direct gravimetric method according to ASTM D7542[50] at INL (Smith 2020),[93] ORNL (Contescu 2008),[14] and KAERI (Chi 2008),[95] and (Chi 2017).[53] Other data were measured by the gravimetric method using TGA equipment (Lee 2013)[100,101] and by an unspecified method (Huang 2014).[97]

Analysis of data for NBG-18 oxidation rates reaches the same conclusion as for IG-110: the only measurements that agree with one another are those that adhered to the standard method of ASTM D7542,[50] regardless of where the research was conducted.[14,53,93,95] The thermogravimetric analysis results[100,101] are also consistent with the data from the standardized method, except when the low air flow rate became limiting at high temperatures.

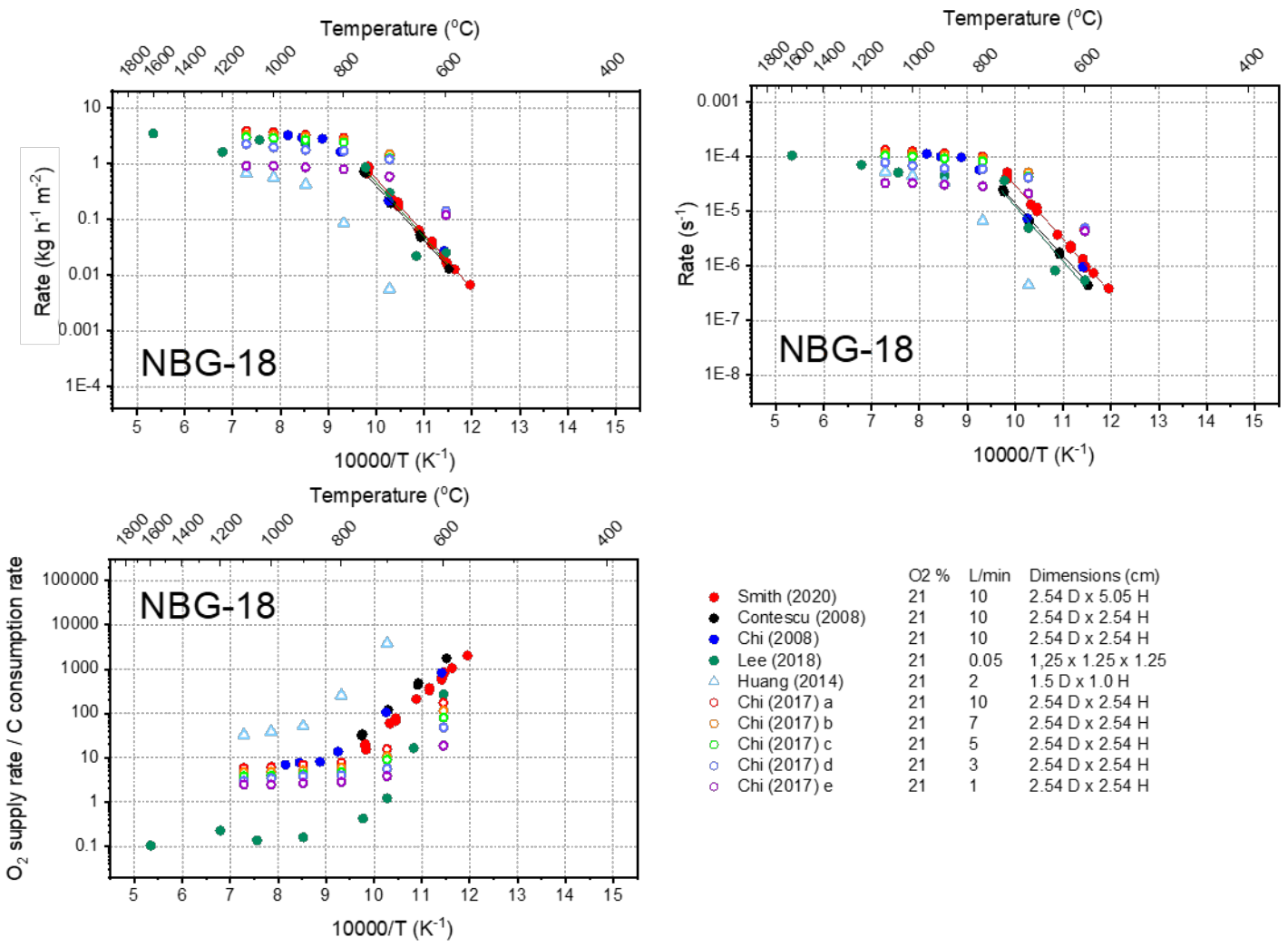

Figure 22. All rate data for oxidation of NBG-18 by air. Data were measured by continuous gravimetric methods either in a VF according to ASTM D7542 or in commercial TGA equipment.

Table 4 presents a summary of kinetic parameters reported by various sources for oxidation of NBG-18 by air. Kinetic parameters were recalculated from explicit numerical collections when available or from the digitized images in Figure 22, but only those data meeting some ad-hoc quality standards were selected for this table. The most important purpose of this selection was to eliminate results measured in oxidant-starving conditions. Only those data points with an oxygen supply rate at least 10 times higher than the rate of carbon gasification at the respective temperature were considered. A second selection condition was that no calculation of an Arrhenius slope and intercept with fewer than three data points was accepted as meaningful. With these strict selection conditions, some results reported in the literature (present in Figure 22) were not considered reliable and had to be disregarded. This way, the compilation of NBG-18 results presented in Table 4 is different from what can be found in other literature sources.[101]

Table 4. Selected kinetic parameters oxidation of NBG-18 by air

Author	Ref.	Activation energy (kJ/mol)	Preexponent factor ln[A (s^{-1})]	Data points	Temp. range (°C)	Dimensions (cm)	S/V	Flow rate (L/min)	O_2 (%)
Smith (2020)	[93]	190	12.4	20	563–745	2.54 *D* × 5.08 *H*	2	10	21
Contescu (2008)	[14]	187	11.3	8	595–793	2.54 *D* × 2.54 H	2.4	10	21
Chi (2008)	[42]	157	7.7	3	603–808	2.54 *D* × 2.54 *H*	2.4	10	21
Huang (2014)	[97]	206	11.0	3	700–900	1.00 *D* × 1.50 *H*	5.3	2	21
Lee (2013)	[100]	211	11.0	4	600–750	1.25 × 1.25 x 1.25	4.8	0.05	21

Note: For cylindrical specimens, *D* = diameter; *H* = height

4.3.4 Graphite PCEA

Only two sources were found for oxidation kinetics of graphite PCEA by air. Initially, ORNL and INL used direct gravimetric measurement adhering to ASTM D7542[50] to measure oxidation rates of specimens extracted from the as-received (unpurified) PCEA billet. Later, the measurements were repeated on specimens machined from slices of the original billet that were purified by halogen treatment. Purification greatly reduced the total concentration of metal impurities from approximately 600 ppm to approximately 1 ppm (Table 5).[102]

The high concentration of impurities in the unpurified PCEA had a visible effect on oxidation rates. Figure 23 shows unpublished data from an ORNL internal report.[103] The Arrhenius plots of purified PCEA are linear (as expected) between approximately 570 and 775 °C and perfectly overlapped between two parallel runs. In contrast, rate data for as-received PCEA (impure) are shifted to higher values, have lower slope (lower activation energy), bend down above about 715 °C, and do not overlap between parallel runs. Because metal impurities act as oxidation catalysts, oxidation of as-received PCEA is faster, and the transition between chemical control (Regime 1) and in-pore diffusion control (Regime 2) occurs at a lower temperature (about 715 °C).

Table 5. Metal impurity content in as-received and halogen-purified PCEA graphite.[102]

Element	PCEA	
	As received	Purified
	Concentration (ppm wt)	
Aluminum	35	0.06
Calcium	35	0.19
Titanium	11	0.04
Vanadium	350	0.28
Manganese	0.3	< 0.05
Iron	150	0.06
Cobalt	2	< 0.05
Nickel	70	< 0.1
Strontium	0.5	< 0.05
Yttrium	0.4	< 0.05
Zirconium	0.3	< 0.05
Molybdenum	2.5	0.35

Authors' data from ref.[102]

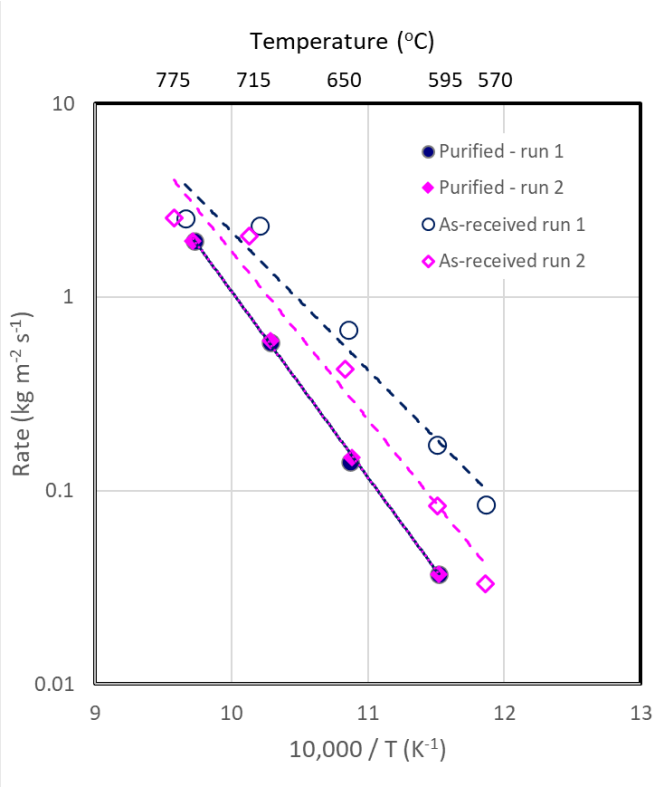

Figure 23. Arrhenius representation of oxidation rate data by air of as-received and purified PCEA graphites. (Authors' data; more information available in ref. [103])

Data obtained at ORNL[38,94] and INL[93] on oxidation of purified PCEA are compared in Figure 24, using a similar template as for IG-110 and NBG-18. Note that INL used PCEA rods with the diameter recommended by ASTM D7542 (D = 2.54 cm) but twice the recommended height (H = 5.08 cm). Because the diameter was the same in the INL and ORNL tests, the results compare very well.

Table 6 presents kinetic parameters for oxidation of halogen-purified graphite PCEA by air. All data were measured according to ASTM D7542 in conditions remote from oxygen starving. Kinetic parameters were calculated by linearization of Arrhenius plots based on statistically significant data.

Table 6. Selected kinetic parameters oxidation of purified graphite PCEA by air.

Author	Ref.	Activation energy (kJ/mol)	Preexponent factor ln(A) (s^{-1})	Data points	Temp. range (°C)	Dimensions (cm)	S/V	Flow rate (L/min)	O_2 (%)
Smith (2020)	93	188	12.1	6	595–695	2.54 D × 5.08 H	2	10	21
Contescu (2008)	94	185	12.1	8	595–756	2.54 D × 2.54 H	2.4	10	21

Note: For cylindrical specimens, D = diameter; H = height

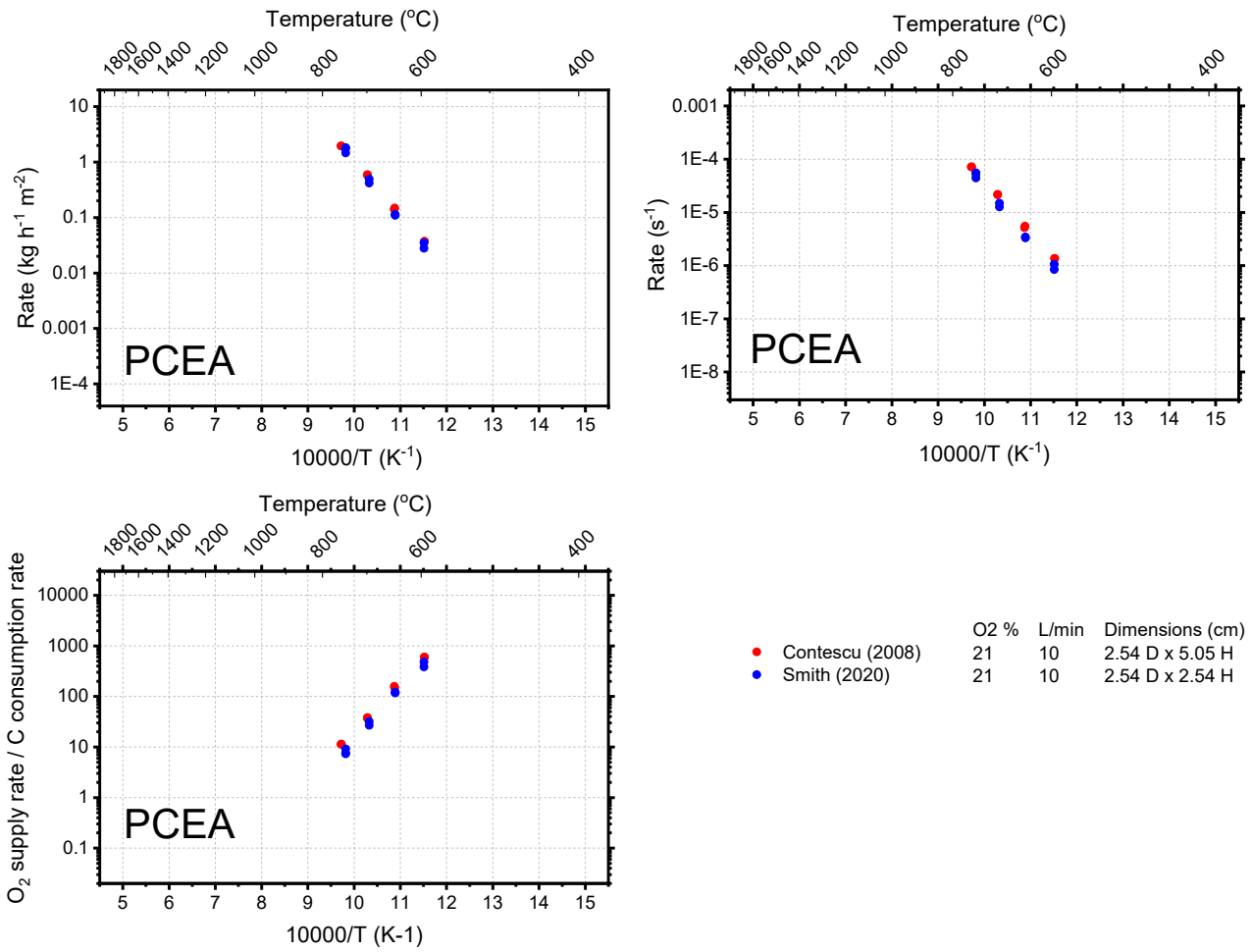

Figure 24. All rate data for oxidation of PCEA by air. Data were measured by the continuous gravimetric method according to ASTM D7542.

4.3.5 Conclusions on Acute Oxidation Tests

Examination of the data presented leads to several conclusions, listed as follows:

- All data collected by researchers who used experimental setups adhering to ASTM D7542 (by the continuous gravimetric method in the kinetic regime) agree well with one another. The reproducibility factor between sources is within the values reported after the original interlaboratory study of ASTM D7542.[50]

- In contrast, data collected by other methods, or at other conditions than those recommended by ASTM D7542, show large deviations between laboratories and workers, even for the same graphite type. These data may be a good source of exploratory information, which is useful for verification of oxidation models but cannot be recommended for modeling purposes.

- The range in which Arrhenius plots are linear (i.e., the kinetic regime) is approximately between 500 and 750 °C for specimens with shape and size conforming to ASTM D7542, provided excess air supply is available to avoid starving conditions. When specimens with nonstandard shape or smaller size are used, or in oxidant-starving conditions, the range of linear Arrhenius plots shifts toward lower temperatures.

- The apparent activation energies reported by various researchers for oxidation rates in Regime 1 (chemical control) are grouped in a relatively narrow interval. Although apparent differences between graphite grades have been reported, when they are analyzed statistically, it appears that such differences are minor and of similar magnitude to the scatter of reported values of individual graphite grades.

- The pre-exponential factor of the Arrhenius equation is not so well defined as the activation energy. It depends not only on the units (normalization by geometric area or by mass), but also on specimen shape and size, and flow conditions (development of starving conditions at insufficient oxidant supply rates).

- Pre-exponential factors increase with the weight loss degree during the transient conditions before about 5% weight loss, when the steady-state oxidation regime is reached.

- Metal impurities that may act as oxidation catalysts may accelerate oxidation rates in an uncontrollable way.

4.3.6 Comparison of Oxidation Behavior of IG-110, NBG-18, and PCEA

Several sources[14,95,101,103] agree on the observation that the air oxidation resistance of the three graphite grades discussed here increases in the order IG-110 << PCEA < NBG-18. An example is shown in Figure 25**,** which compares the oxidation rates in air at four temperatures (600, 650, 700, and 750 °C). At these temperatures, oxidation is in the kinetic regime and the resultant density profiles are (almost) uniform. The plots show the transient increase of oxidation rates with time during the onset period, when the weight loss increases to about 15 %. At every temperature, IG-110 shows the fastest oxidation rates, NBG-18 shows the slowest rates, and PCEA shows rates in between these extremes. These differences reflect the microstructural differences between grades.[14]

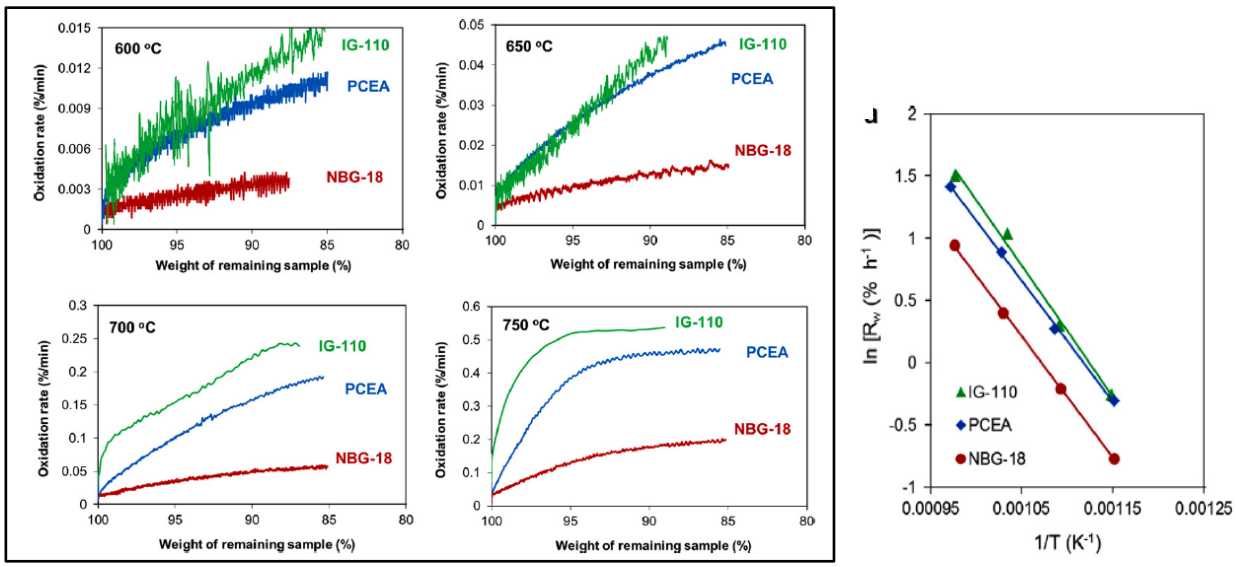

Figure 25. Oxidation rates in the kinetic regime of graphites IG-110, PCEA and NBG-18 up to about 15 % weight loss. (a) Oxidation rate variation versus weight loss at various temperatures; (b) Arrhenius plots (R_w = oxidation rate normalized to initial mass). (Authors' data; more information available in ref.[14])

The three graphite grades discussed have significant microstructural differences, as discussed in Section 3. The grain size is one important property because it is related to the pore structure, which determines oxidation behavior. Intuitively, the smaller the grain size, the larger the exposed surface area available for the oxidant attack. This may be a possible explanation for the faster oxidation rates of superfine-grained IG-110 (average grain size 20 μm) compared with medium-fine–grained PCEA (800 μm) and medium-grained NBG-18 (maximum 1600 μm).

However, a second factor is the fraction of open pores and their interconnectivity in the internal pore systems. According to porosity data of these three grades (Figure 5), IG-110 has unimodal pore distribution with uniform diameters (about 3.9 μm), whereas the other two grades have a combination of fine and large pores that span dimensions from single digits to tens of microns. The volumes of open and closed pores of these three grades (Table 2) provide more information. In the total pore volume (0.12 cm^3/g) of graphite IG-110, a significant fraction (0.08 cm^3/g) is open to gas access. In contrast, NBG-18 has a smaller total pore volume (0.09 cm^3/g), of which only a small fraction (0.04 cm^3/g) is open to gas access. PCEA is in between the other two, with a total pore volume equal to that of IG-110 (0.12 cm^3/g), and a volume of open pores (0.06 cm^3/g) that is smaller than that of IG-110 but larger than that of NBG-18. This ranking matches well with the order of increasing resistance to oxidation by air.

A third structural factor might also be considered in relation with the oxidation kinetic parameters.[14] Figure 25b shows Arrhenius plots for oxidation by air of the three graphite grades. As discussed previously, the slope of these plots characterizes the apparent activation energy, and the intercept can be used to calculate the frequency k_0 of oxidation events (see Eq. (2)). Although some variability may be found between kinetic parameters measured by various researchers or by various methods, as shown earlier, consistent conclusions can be obtained by comparing critically selected parameters (Table 3, Table 4, Table 6). Considering only ORNL and INL results for the three grades, it is apparent that the grade with the highest reactivity (IG-110) has the largest apparent activation energy (191–195 kJ/mol) in air (21 % O_2) and the largest pre-exponential factor (13.0–13.1) in the Arrhenius equation expressed as ln (A) using rates normalized in units of s^{-1}. The other two grades have lower and quite similar activation energies (185–188 kJ/mol for PCEA; 187–190 kJ/mol for NNBG-18) and pre-exponential factors (12.1 for PCEA; 11.3–12.4 for NBG-18). Interestingly,

the pre-exponential (i.e., frequency) factors correlate with the ASA, which includes C atoms at edge sites or defect positions in graphite sheets. The ASA can be estimated from crystallographic analysis[14] or obtained directly from N_2 adsorption measurements after subtracting the basal plane area (BPA) from the total surface area (TSA) determined by the BET method.[17]

Similar conclusions were reached by Kane et al.[104] who compared the change in RSA and morphology during slow oxidation by air of tinny NBG-18, PCEA, and IG-110 specimens. The faster bulk oxidation of IG-110 was attributed to its highly interconnected pore structure, which favored faster O_2 diffusion compared with NBG-18 and PCEA. Because a larger internal pore surface was exposed to air by IG-110 than by the other graphites, the corresponding RSA was assumed the largest for this graphite. On similar grounds, PCEA was oxidized faster than NBG-18, despite their similar effective diffusivity for O_2, because of the larger exposure of internal pore surface, equivalent to a larger RSA within the exposed volume.[104]

4.4 ACUTE OXIDATION BY STEAM OF GRAPHITE IG-110

4.4.1 General Observations

The design of modular HTGRs – in particular, the position of the primary heat exchanger circuit – determines the level of concern for water/steam ingress accidents. For designs in which an intermediate heat exchanger is placed between the primary circuit in the core and the balance of the plant, the probability of significant water/steam ingress accidents is minimal. Ingress probabilities are much higher for designs with in-line steam generators.[87] Water or steam ingress in the hot core may cause positive reactivity insertion (because of the neutron-moderating effect of water) and may chemically attack and damage graphite structures. Chemical oxidation of graphite may cause corrosion of graphite core components and (if exposed) of coated fuel particles. In the case of long-lasting ingress events, graphite corrosion may challenge the integrity of fuel elements and structural components. The gases formed in the water reaction with graphite (CO and H_2) present additional safety concerns. Moreover, the graphite reaction with steam is endothermic at high temperatures.

However, significant water ingress accidents are considered to be very unlikely, except in the case of in-line steam generators. Even so, positioning the steam generator below the reactor core may eliminate the possibility of direct steam ingress and restrict the consequences of water ingress events to controllable levels, as shown by the analysis of HTR-PM reactor safety features.[105] Depending on the amount of water intruded and the temperature conditions, these events may be categorized as AEs with low probability or DBEs with extremely low probability.[87]

4.4.2 Graphite IG-110

Experimental results for temperature effects on the reaction rates between historic graphite grades and water were presented in Figure 16. The Arrhenius plots of that figure show the evolution of reaction rates with both the temperature and the level of weight loss for two graphite grades that were planned for fuel elements and the moderator. The limited amount of direct experimental data available on oxidation kinetics by water of historical graphite grade H-451[32] has been used for safety analyses of newly designed HTRs, such as the HTR-PM in China.[34,45,69,] Because of the lack of data at high steam pressure, some of these analyses needed to extrapolate kinetic results measured at low H_2O partial pressures to the presumed conditions of a high steam ingress accident. Details are discussed in Section 6.2.8.

At the time of this writing, only one report was found in the open literature with experimental kinetic data for high-pressure steam (0.2 bar) oxidation of graphite IG-110.[36] The results are presented in Figure 26 in the Arrhenius format. Measurements were extended to temperatures higher than those explored by previous researchers. The oxidation progress was not measured continuously, and the activation energies were

estimated between pairs of neighboring data points at different temperatures, which was not highly accurate. However, the trend is clear: a break in Arrhenius plots near 1100°C signals the transition from chemical control (Regime 1) to in-pore diffusion control (Regime 2). This is accompanied by a drop in apparent activation energies, as shown in Figure 26. Significantly, activation energies for oxidation by steam are higher than those for oxidation by air, and the corresponding temperatures of Regimes 1 and 2 are also higher for oxidation by steam (compared with Figure 20). These trends indicate that oxidation by water is a much slower process than oxidation by air and requires higher temperatures to produce measurable rates.[4] No data were found in the literature for oxidation of graphites NBG-18 and PCEA by steam.

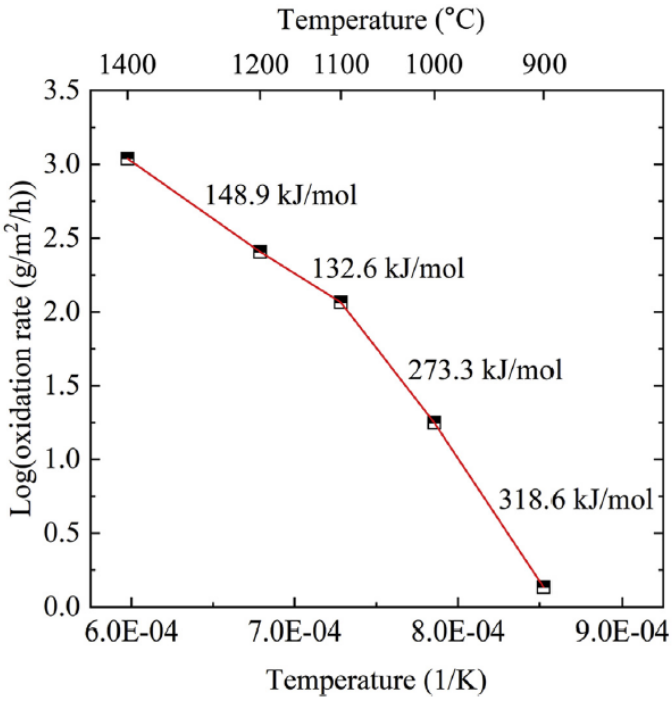

Figure 26. Effect of temperature on IG-110 oxidation rates by steam (20 kPa in Ar) at 1 bar total pressure. Apparent activation energies were calculated from the slopes of Arrhenius plots in each temperature interval. (More information in ref.[36])

5. DEGRADATION OF PROPERTIES CAUSED BY OXIDATION

5.1 DENSITY PROFILE, CORROSION, AND DIMENSIONAL CHANGES

5.1.1 Mathematical Models for Oxidant Penetration and Graphite Density Profile

The main effect of graphite oxidation is porosity development at the expense of lower density. As oxidation proceeds inward from the exposed surface, the newly developed pores and local graphite density are rarely uniformly distributed in the bulk. The depth of the oxidized subsurface zone depends on the competition between the rate of inward oxidant transport (diffusion) and the rate of oxidant consumption through graphite gasification (oxidation).[74,75] These two processes accelerate with increasing temperature, but in different ways: diffusion follows a power law, whereas chemical reactions follow the exponential (Arrhenius) law. At any given temperature, the oxidant penetration depth (i.e., the active oxidation zone[41]) is the maximum distance traveled by the oxidant before it is totally consumed by chemical reactions. As the oxidant concentration in pores drops with the distance from the surface, the graphite density follows a mirror-image profile from a minimum near the surface to the bulk density at some depth in the bulk.

Development of nonuniform oxidation profiles in graphite is of concern for reactor designers. To estimate the depth of the oxidation zone and the overall graphite oxidation rate, designers need a model that correlates kinetics (first-order rate constant, as a first approximation) with in-pore diffusivity and oxidant penetration depth profile.[106] Several models have been proposed and compared with experimental density profiles in cylindrical graphite specimens oxidized by air, moisture, or CO_2.

Wichner showed that the oxidant concentration profile can be estimated from the simplified model of reaction coupled with diffusion in porous bodies.[74,75,76] At sufficiently long times after the first attack of the oxidant, a steady-state condition is reached such that at some distance x from surface, the net oxidation rate is null because the oxidant diffusion rate equals the in-pore gasification rate. From Eq. (4), it follows that at the maximum penetration depth, the local oxidation rate in Regime 2 is zero:

$$Rate_2 = \frac{\partial C_{ox}(x)}{\partial t} = \frac{D_{eff}}{\varepsilon}\frac{\partial^2 C_{ox}(x)}{\partial x^2} - Rate_{pore}(C_{ox}, T)\nu = 0\ . \tag{15}$$

Assuming the linearized kinetics from Eq. (2), the solution is

$$\frac{C_{ox}(x)}{C_{ox}(x=0)} = \exp\left[-\sqrt{\frac{Rate_{pore}(C_{ox},T)\nu}{D_{eff}}}\ x\right] = \exp(-Bx)\ . \tag{16}$$

Equation (16) shows that the oxidant concentration profile, $C_{ox}(x)$, is described by an exponential decay function whose argument B depends on the ratio between the local in-pore gasification rate and the effective diffusion coefficient for oxidant transport:

$$B = \sqrt{\frac{Rate_{pore}(C_{ox},T)\nu}{D_{eff}}}\ . \tag{17}$$

The graphite density profile is given by an exponential growth function with the same argument, B. This approach uses two simplifying approximations, which may not be taken as granted in a real situation: first, the kinetic equation may not be linear (as is the case with LH and BLH models); second, the effective diffusion coefficient is not constant, but evolving (increasing) with the progress of oxidative pore growth.

This analysis has been verified by experimental results. For example, Figure 27 shows theoretical predictions of temperature effects on the oxidant penetration depth. The plots show predicted subsurface

distances where the concentrations O_2 and H_2O have dropped to 90 % from their free gas value. These predictions agree well with experimentally measured density profiles in the oxidized layer of a graphite electrode oxidized in air.[52,74,75]

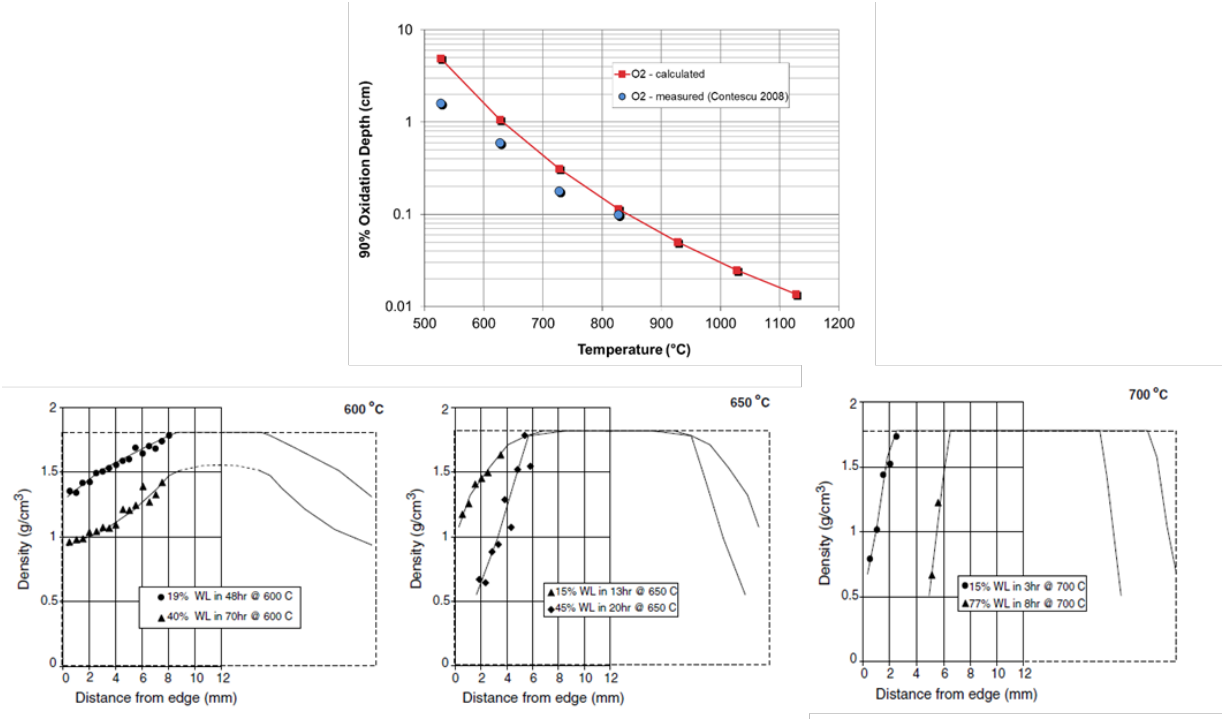

Figure 27. Temperature effects on oxidant penetration depth and thickness of oxidized layers. Predicted[74] and experimental distances from the surface where O_2 concentration drops by 90% as a function of temperature (top figure) are compared with actual measurements[52] of oxidized layer density profiles in a graphite electrode oxidized in air at three temperatures (bottom figures). (Authors' data; more information available in cited references)

It is important to emphasize that the maximum oxidant penetration depth is the long-term solution, calculated for $t \rightarrow \infty$.[74,75] If temperature is constant (and neglecting the increase of porosity), the oxidant cannot penetrate deeper because it is consumed in totality before reaching the maximum penetration depth. In the early stages of oxidation, its distribution follows the same exponential profile, but with lower amplitudes because the weight loss near the surface ($x = 0$) is still low. With time, the weight loss increases, and the amplitude of penetration depth increases, as well. However, the spatial extent (along the distance from the surface, x) does not change. This mechanism, common to chronic and acute oxidation, is illustrated in Sections 5.1.2 and 5.1.3 by optical microscopy images.

5.1.2 Oxidation by Water

The prismatic design of the graphite fuel element has parallel channels for fuel compacts and coolant circulation. They are separated by walls only a few millimeters thick. If chronic oxidation by impurities in coolant penetrates these separation walls, then the whole structure of fuel elements may be jeopardized. For safety reasons, it is important to determine how deep and how fast would develop the damage caused by chronic graphite oxidation. In addition, water (steam) ingress on the hot reactor can produce acute graphite oxidation following a low-probability accident classified as AE or DBE.

The development of oxidized layers on the surface of nuclear graphite after chronic oxidation by moisture was initially analyzed by General Atomics researchers for grade H-451, the candidate at the time for the

HTGR moderator. After the LH kinetic constants for oxidation by moisture of graphite H-451 were first time measured, [32] they were used to predict H_2O concentration profiles in the case of an unlikely water ingress accident.[68] Figure 28 compares the calculated H_2O concentration profile with the graphite density profile measured in an oxidized layer of graphite 2020 exposed to conditions simulating acute oxidation after a steam ingress event (P_{H2O} = 50 kPa; P_{H2} = 2.5 kPa; T = 1000 °C) for a total exposure time of 20 h. Although the predicted density profile was based on graphite H-451 oxidation kinetics and the actual density profile was measured for another grade (graphite 2020), they compared well. Based on experimental details from the original report,[68] the maximum penetration depth was 2 mm.

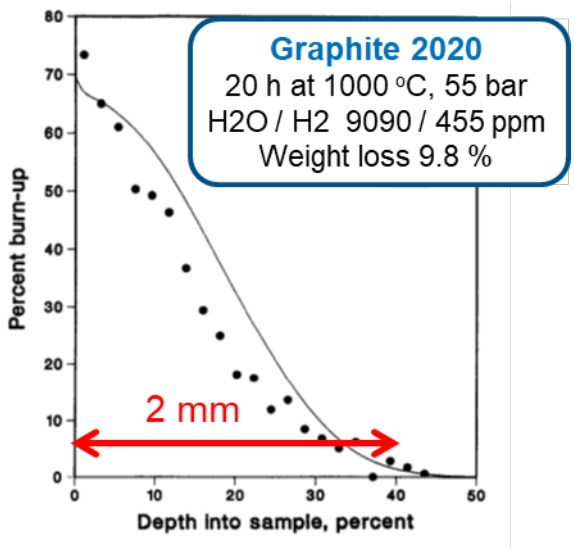

Figure 28. Predicted oxidation layer profile and measured density profile for graphite 2020 oxidized by steam. (Based on ref.[68] with additions by the authors).

More information on chronic oxidation by moisture impurities in the coolant was obtained from a systematic study at ORNL during 2012–2019.[33,35,65,71,72] Four graphite grades with different structures and properties (PCEA, NBG-17, IG-110, and 2114) were selected from the list of possible candidates for HTGR systems. The goal was to evaluate the effects of long-term chronic oxidation on graphites with various structures, including the effect of temperature on oxidation rates and oxidant penetration depth. Because the rates of oxidation by moisture are extremely slow at the parts per million concentrations expected in the HTGR coolant, the experiments have to be performed at higher H_2O concentrations and temperatures. In these accelerated oxidation conditions, it was found that the LH kinetic model can be applied for oxidation rates at low H_2O partial pressures and temperatures, but it is less adequate for higher water vapor pressures and temperatures.

Accelerated oxidation rate measurements over a broad range of partial pressures of water ($3 < P_{H2O}$ (Pa) < 1000) and hydrogen ($3 < P_{H2}$ (Pa) < 150) and wide temperature range (800 < T (°C) < 1000) were analyzed using both LH or BLH kinetic models, and the corresponding kinetic parameters were obtained by best fitting methods. Using this information along with direct measurements of effective H_2O diffusivity from H_2O/He mixtures, the concentration profiles for H_2O in the four graphite grades (PCEA, NBG-17, IG-110, and 2114) were calculated at several temperatures. The results were then compared with the porosity profiles measured by optical microscopy in specimens oxidized at the same temperatures. The results, detailed as follows, demonstrated good agreement with the Wichner model for graphite oxidation.[74,75,76]

Figure 29 shows porosity profiles in specimens of the four graphite grades after oxidation by moisture to a maximum 1.5% weight loss at various temperatures.[76] The depth of the oxidized layer is larger at low

temperatures and becomes narrower with the increase in temperature. However, the behavior of each graphite grade is different, reflecting structural differences. For example, the change of porosity profiles is more difficult to detect for IG-110, which has an extensive structure of fine interconnected pores. Conversely, PCEA and NBG-17 have large but apparently isolated pores. The most significant result is that the largest depth of oxidant penetration at 800–850 °C is between 2 mm (for PCEA) and 0.8 mm (for 2114 and NBG-17). At higher temperatures, the penetration depth becomes even narrower.

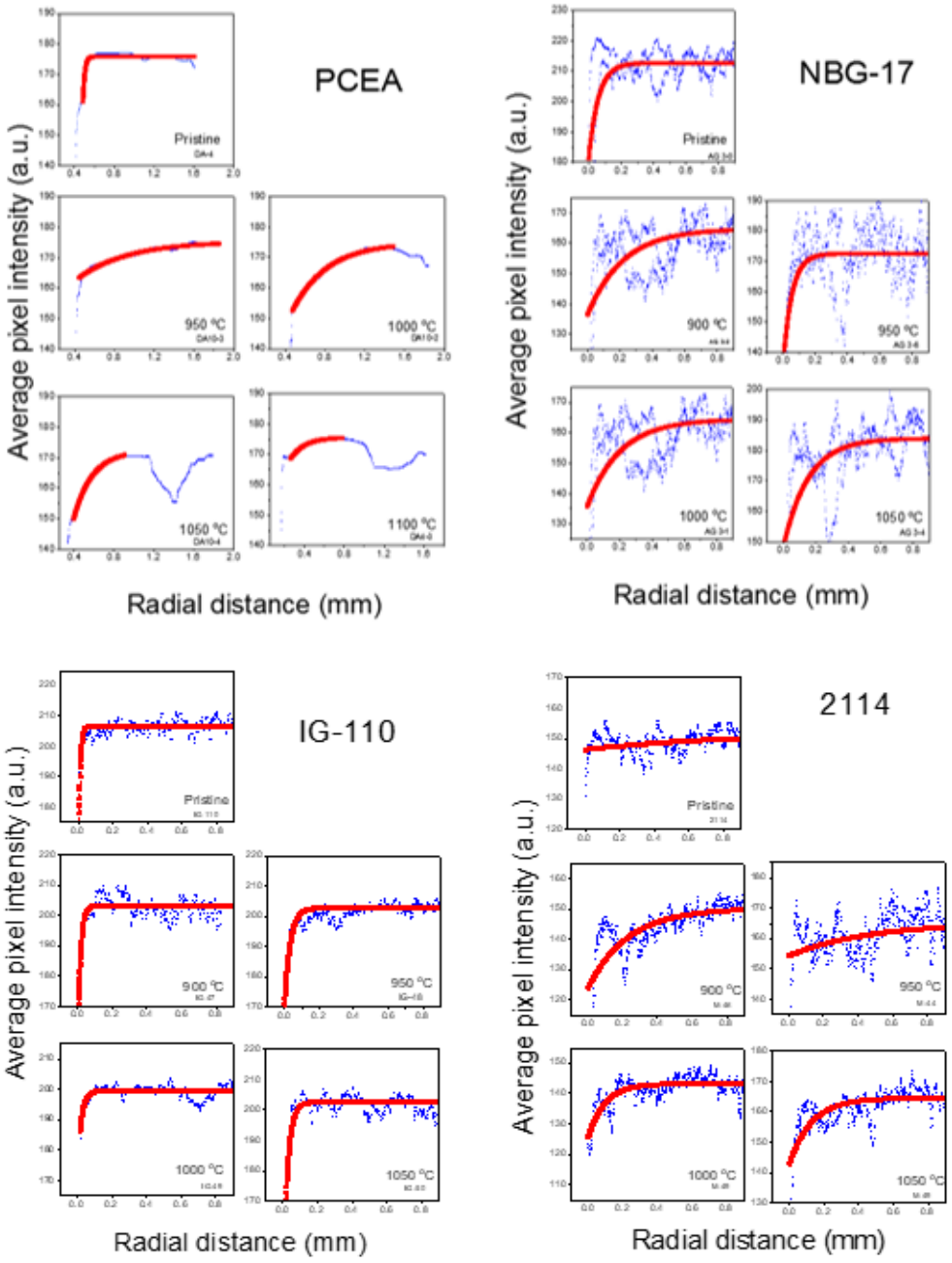

Figure 29. Effect of temperature on the porosity profiles of four graphite grades oxidized by moisture. Line scans of pixel intensities in optical micrographs are plotted against radial distance from the exposed surface. The irregular contour in some images is caused by the presence of random large pores, such as in PCEA. Note the difference in x axis scales between PCEA and the other three grades. (Authors' data; more information available in ref.[76])

Figure 30 illustrates the application of the Wichner model for chronic oxidation by moisture of two graphite grades, PCEA and IG-110, with very different structures.[74,75,76] Related to their pore structure, the two graphites have different reduction factors of H_2O effective diffusivity ($\beta = D_{eff}/D_{\text{free gas}}$). This difference leads to various behaviors of oxidation rates (in the absence of H_2) versus temperature and P_{H2O}. Using the kinetic parameters for the BLH model and the respective transport parameters (D_{eff}), the oxidant profiles were calculated for each grade as a function of temperature. The predicted penetration depths calculated from the model were in reasonably good agreement with the measured porosity profiles of specimens oxidized at each temperature. The experiments confirm the applicability of the Wichner model to chronic oxidation by moisture.

Based on the above results one concludes that chronic oxidation by oxidizing impurities (H_2O, possibly CO_2) in the coolant is not a cause of safety concern for long-term normal operation of HTGRs, on the condition that the concentration of oxidizing impurities is continuously maintained within the limits prescribed by the operation parameters envelope. The main factors that support this conclusion are as follows:

- The very low concentration of moisture impurity in helium coolant drastically limits the total amount of oxidant that may be in contact with graphite during a reactor's lifetime.

- Oxidation rates by water are roughly 10^5 slower than oxidation rates by air (oxygen).

- The maximum penetration depth of water vapor, as determined by oxidation rates and water effective diffusivity in graphite, is maximum 1–2 mm at the worst conditions (low temperatures).

- Because of the extremely low oxidation rates at normal operating temperatures, the time needed for oxidation to completely penetrated and erode the thin superficial layer of active oxidation zone is much longer than the service time of HTGRs.

The same conclusion was reached after analysis of experimental data and by model simulations by researchers at General Atomics,[32] Tsinhua University,[34] ORNL,[33,35] the University of Michigan,[60,78] and others.

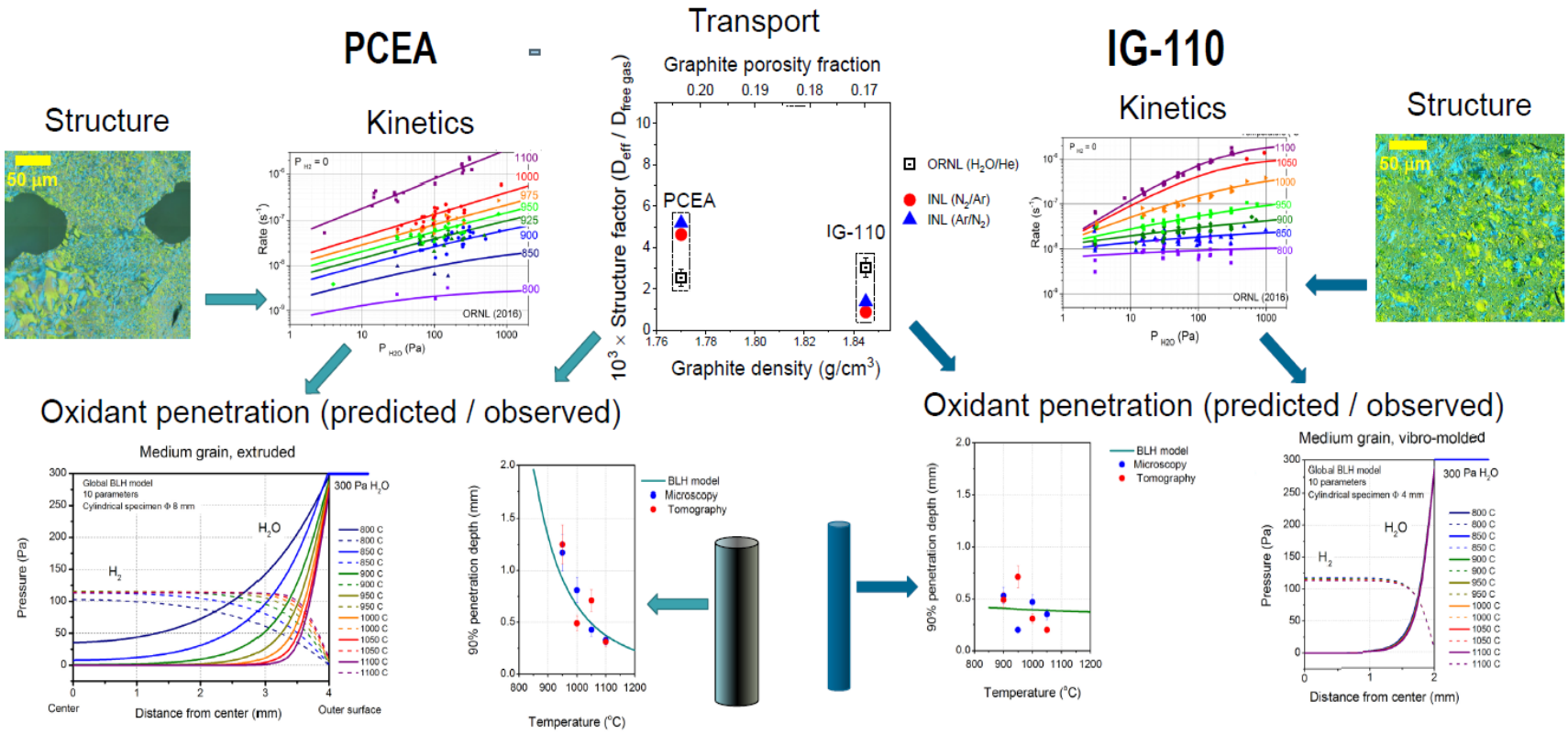

Figure 30. Validation of the Wichner model for oxidation of PCEA and IG-110 by moisture. The montage shows information on structure (optical microscopy with polarized light), kinetics (oxidation rates versus P_{H2O} at various temperatures and their fit by the BLH model), transport (structure factor $\beta = D_{eff}/D_{free\ gas}$), concentration profiles calculated for water (P_{H2O}) and hydrogen (P_{H2}), and comparison between predicted penetration depth for 90% concentration drop and measured thickness of the oxidized layers at various temperatures. (Authors' data; more information available in ref.[76])

5.1.3 Oxidation by Air

Oxidation by air is a concern in the event of accidental air ingress over the hot graphite core. The rates of chemical reactions between carbon and oxygen are much faster than those of oxidation by water. However, the effective diffusivity differences between O_2 and H_2O are minor. As a result, oxidation by air can be observed from lower temperatures and produces nonuniform density profiles at temperatures where oxidation by moisture is mostly uniform.

Figure 31 shows images of NBG-18 specimens oxidized in air at four temperatures to the same level of mass loss (15 %).[107] The cross-sections show the depth of the oxidized layer. The samples oxidized at lower temperatures (600, 650, and 700 °C) kept the initial dimensions (2.54 cm *D* × 2.54 cm *H*) before oxidation, as oxidation spread through the bulk. With the increase in temperature, the oxidized layer shrunk, but the external dimensions were still unchanged. However, at 750°C, oxidation was localized near the surface. Because of preferential binder oxidation, filler grains were detached as dust; rapid corrosion caused dimensional shrinking.

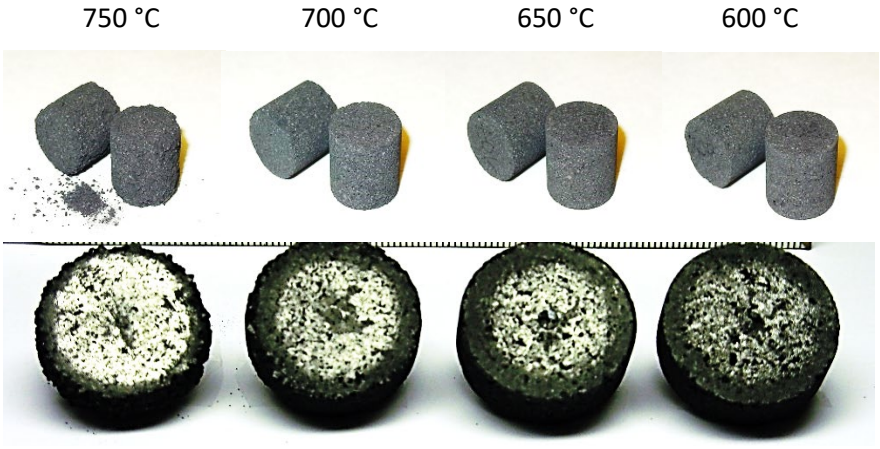

Figure 31. NBG-18 specimens oxidized in air to 15% mass loss at four temperatures. Note the evolution of the oxidized layer and surface corrosion with formation of dust at the highest temperature. (Authors' images[107])

More examples of porosity development in the oxidized layers of IG-110, NBG-18, and PCEA specimens are shown in Figure 32.[14,107,108] Oxidation was carried out in air at various temperatures (600 to 750 °C) up to 15 % mass loss. For each graphite grade, the pores were identified by image analysis of optical microscopy images and were colored according to the color code attached. Each graphite has a different microstructure: in IG-110, the pores are small and uniformly distributed; PCEA has a combination of small pores and large lenticular pores; NBG-18 has small pores along with large, quasi-spherical pores. Images show that pore densities are higher in the oxidized layers (on the left side of the micrographs). The thickness of oxidized layers is greater at low temperatures (about 4–5 mm). Upon increase in temperature, the oxidized zone becomes narrower. At the highest temperature, oxidation approaches Regime 3. The exposed surface becomes rough, and the oxidized layer penetrates only a few millimeters. Fast oxidation at 750 °C caused intense surface corrosion and rapid dimensional shrinking.

The mechanism of oxidized layer development at 600 °C by pore growth and coalescence is illustrated in Figure 32d. With the increase of mass loss, the width of the oxidation layer does not increase; only the porosity increases through multiplication of pores and growth of their sizes. Eventually, pores connect and collapse into larger pores, but the width of the oxidized regions does not change significantly.

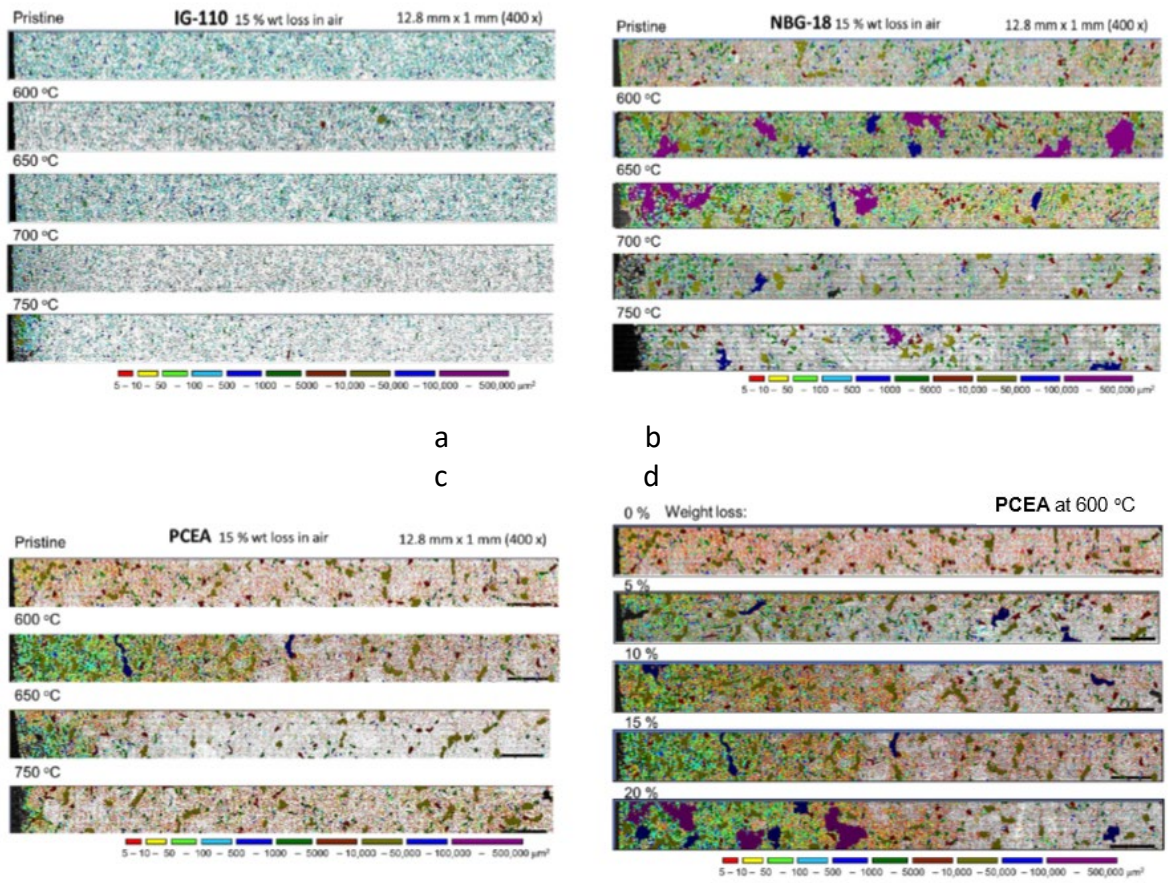

Figure 32. Optical microscopy images of subsurface porosity of IG-110, NBG-18, and PCEA oxidized in air. Graphite specimens were oxidized at different temperatures (600–750 °C) to equal mass loss (15%); also, PCEA was oxidized at a constant temperature (600°C) to different levels of mass loss (up to 20%). (Authors' data; more information available in refs.[107,108])

In Figure 33, the oxidized layers in IG-110, PCEA, and NBG-18 specimens were imaged by optical microscopy for specimens oxidized in air to 15 % mass loss at different temperatures.[108,109] The figures show line profiles of pixel intensity distribution along the distance from the exposed surface. They indicate pore density profiles, which correlate with the penetration depths visualized from optical micrographs. In these scans, high pixel intensities correspond to shiny, unoxidized regions, and low intensities indicate less reflective, rough surfaces in the oxidized region. At equal weight loss, the penetration depth is greater in specimens oxidized at lower temperatures and gradually decreases with the increase in temperature.

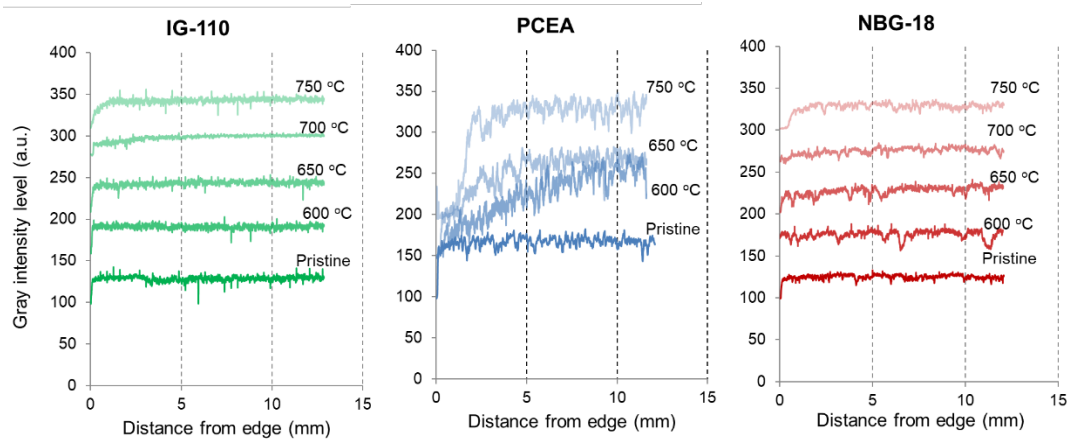

Figure 33. Optical microscopy analysis of IG-110, PCEA, and NBG-18 specimens oxidized in air to 15% mass loss. Images show line profiles of pixel intensity scans inward from the surface. Oxidized regions near the graphite edge have low pixel intensities. All curves have been shifted vertically for clarity. (Authors' data; more information available in ref.[108])

Figure 34 compares the volumes of PCEA samples before and after oxidation at three temperatures.[108] Large (25.4 mm D × 25.4 mm H) and small (12.7 mm D × 25.4 mm H) specimen sizes were used. The specimens were oxidized in similar conditions, but the effects of oxidation on the volume of oxidized samples were different. Large specimens oxidized at 600 °C and 650 °C were unchanged up to 20 % weight loss, showing that oxidation occurred uniformly in the bulk. Only after oxidation at 750 °C did large specimens show volume shrinkage, which indicates nonuniform oxidation and possibly surface corrosion. In contrast, small specimens were affected more by surface corrosion, starting from the lowest oxidation temperature (600°C).[108]

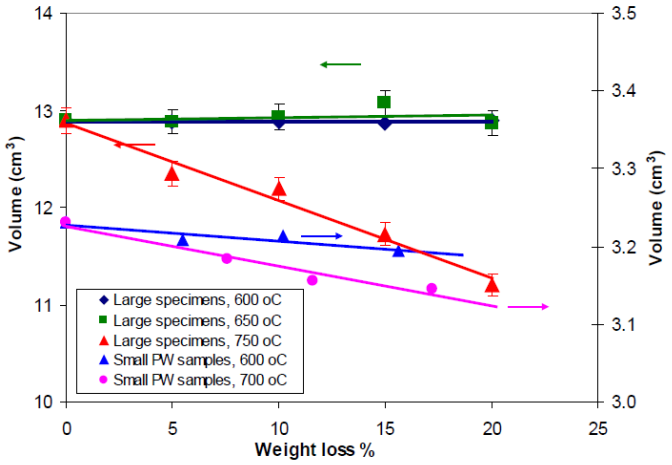

Figure 34. Volume variations of oxidized PCEA specimens as a function of weight loss. Average data for large specimens (25.4 mm D × 25.4 mm H) are plotted on the left ordinate axis. Average data for small specimens (12.7 mm D × 25.4 mm H) are plotted on the right ordinate axis. (Authors' data; more information available in ref.[108])

5.2 MECHANICAL PROPERTIES

5.2.1 General Observations

The main effects of graphite oxidation are increased porosity and decreased density. However, as shown in the previous section, porosity development is mostly nonuniform since it depends on the conditions of oxidation (temperature, duration, and oxidant nature and availability) and on the graphite properties (porosity, microstructure). Because mechanical properties (compression and tensile strength, Young's modulus) are strongly related to graphite density, oxidation also causes nonuniform distribution of local mechanical properties in the oxidized layer. The oxidant penetration depth may vary from several millimeters for oxidation in Regime 1 (low temperature) to a few microns for oxidation in Regime 2 (intermediate temperatures). In the oxidized layer, the local density, porosity, and mechanical properties are strongly correlated. Mechanical properties are weakened in the high-porosity (low-density) regions near the exposed surface and tend gradually toward the bulk values deep under the surface.

Three practical questions follow:

- How can the progress of oxidation and related degradation of properties be quantified?
- What is the effect of weaker properties in the oxidized layer on the overall properties of full-scale graphite components?
- Can the change in mechanical properties be predicted based on graphite oxidation models?

The early studies on HTGR systems demonstrated that mechanical strength degradation of oxidized graphite was somehow dependent on the oxidation temperature: at equal mass loss percentage, the loss of strength was greater after low-temperature oxidation than after high-temperature oxidation. An example is shown in Figure 35 for PCEA specimens (12.7 mm D × 25.4 mm H) oxidized at 600 °C and 700 °C. Interestingly, it appears that net strength changes depend also on specimen orientation (with/against grains) which probably reflects the effect of grain edges exposure to in-bulk oxygen diffusion.[108]

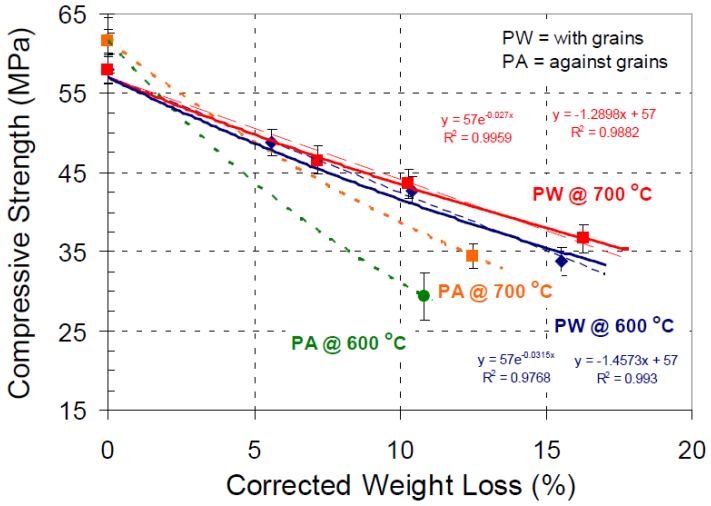

Figure 35. Average compressive strength of oxidized PCEA specimens as a function of mass loss, oxidation temperature, and grain orientation. Data shown are for small PCEA test specimens (12.7 mm D × 25.4 mm H). (Authors' data; more information available in ref.[108])

The effect of temperature has a simple explanation: uniform oxidation at low temperatures causes extensive bulk damage compared with nonuniform oxidation in a narrow band near the surface. In the latter case, the strength of the undamaged core reduces the negative effect of oxidation.[108,110] The logical way to reduce the uncontrolled effect of unwanted oxidation gradients is to produce uniformly oxidized specimens and to measure the effect tof mass weight on mechanical properties. This procedure was used at the Nuclear Research Laboratory in the United Kingdom,[111] at Brookhaven National Laboratory[112] and General Atomics[113] in the United States, and at the Japan Atomic Energy Research Institute (JAERI).[114] The goal was qualification of graphites (H-451, PGX and IG-110) for use in early HTGR models. Uniform oxidation was achieved by slow oxidation at low temperatures (air at 450–500 °C[114] or CO_2/He and H_2O/He mixtures at 750–950 °C).[114]

5.2.2 Uniformly Oxidized Specimens

5.2.2.1 Compressive strength

A 1987 JAERI report[115] contains a comprehensive summary of graphite oxidation work performed by researchers in Japan on graphite IG-110. The main conclusions regarding strength loss of oxidized graphite are summarized as follows:

- The amount of strength loss caused by oxidation is different between graphite grades, although many graphites show about 50 % strength degradation at density change levels of only 10 %. Weight loss levels can be used instead of density if the volume of oxidized graphite did not change from the initial volume, which is a proof of uniform bulk oxidation (chemically controlled oxidation in Regime 1).

- The amount of strength loss does not depend on the chemical nature or concentration of the oxidant, as long as oxidation proceeds uniformly in the chemical regime.

- The greater the strength loss, the greater the electrical resistivity increase after oxidation.

Figure 36a shows a compilation of compressive strength data versus weight loss of uniformly oxidized, fine-grained isotropic graphites IG-10 and IG-110.[110,116,117,118,119] Researchers took great care to prepare uniformly oxidized graphite specimens using different oxidants (air, 2% O_2/N_2, 2% CO_2/He, 2% H_2O/He) at the appropriate temperatures. In these conditions, the fractional strength loss was correlated only with the mass loss percentage according to a simple relationship known as the Knudsen's equation:[120,121]

$$\frac{\sigma}{\sigma_0} = \left(\frac{\rho}{\rho_0}\right)^n , \tag{18}$$

where σ and σ_0 are the strengths of oxidized and virgin graphite, respectively, and ρ and ρ_0 are the corresponding densities. For uniformly oxidized specimens, with no measurable volume changes, the density ratio can be substituted with the weight loss percentage, $X\,\% = \left(1 - \frac{w}{w_0}\right) \times 100\,\%$. Using the Taylor series development of logarithms and retaining only the first term, an equivalent expression for Eq. (18) is the following:

$$\log\left(\frac{\sigma}{\sigma_0}\right) = -0.01\,n \times \left(\frac{w_0 - w}{w_0} 100\,\%\right) = -(0.01\,n)\,X\,. \tag{19}$$

The empirical relationship proposed by Knudsen has recently found theoretical justification.[122] It shows that degradation of compressive strength is determined solely by the extent of mass loss or the density reduction. The nature of oxidizing gas did not have significant effects.

Numerous compressive strength data are available for oxidized IG-110 or IG-10. Measurements were done on cylindrical specimens with the oxidized ends removed to avoid spurious results by early failure of the soft, oxidized ends. In these conditions, n = 5.6 for purified IG-10 over a broad range of weight loss values.[110] Similar data were reported by other investigators for IG-110. More recently, a "rule of thumb" was formulated[123] according to which 10 % mass loss is accompanied by 50 % strength loss; the corresponding exponent is n = 6.8. This more conservative trend is indicated by the red dashed lines in Figure 36. The isotropic fine-grained graphites are slightly more resistant to strength degradation than what the above-described rule predicts. A different trend was recently reported for IG-110 oxidized at 550°C. Initially, the oxidized ends of cylindrical rods perturbed the measurements, but after trimming the ends, the strength values showed a more aggressive degradation trend (n = 7.6) than prior reports.[119] It was shown previously[108,124] that trimming the ends of the oxidized rods is required to obtain the shear failure mode characteristic to graphite. When the ends of oxidized specimens were not removed, the results showed a more aggressive, but erroneous, strength deterioration (e.g., n = 11.4) for IG-110.[125]

Figure 36b shows strength degradation versus mass loss percentage for graphite NBG-18 oxidized in air at 550°C. At this temperature, the oxidation was most likely uniform under chemical control (Regime 1).[119] The trend fits the same rule of thumb: 50 % strength loss at 10 % weight loss.

For comparison, Figure 36c shows compressive strength degradation data for graphites PGA and Gilsocarbon oxidized radiolytically in CO_2.[126,127,128] Radiolytic oxidation caused by ionizing irradiation is unavoidable in the UK fleet of Magnox and AGRs using CO_2 as coolant but will not occur in helium-cooled HTGRs. Interestingly, the loss of compressive strength by the radiolytic mechanism is less aggressive than the behavior after thermal oxidation by air.[126] This is shown by the lower values of n coefficients for radiolytic oxidation. A clear explanation for this behavior is not available yet.

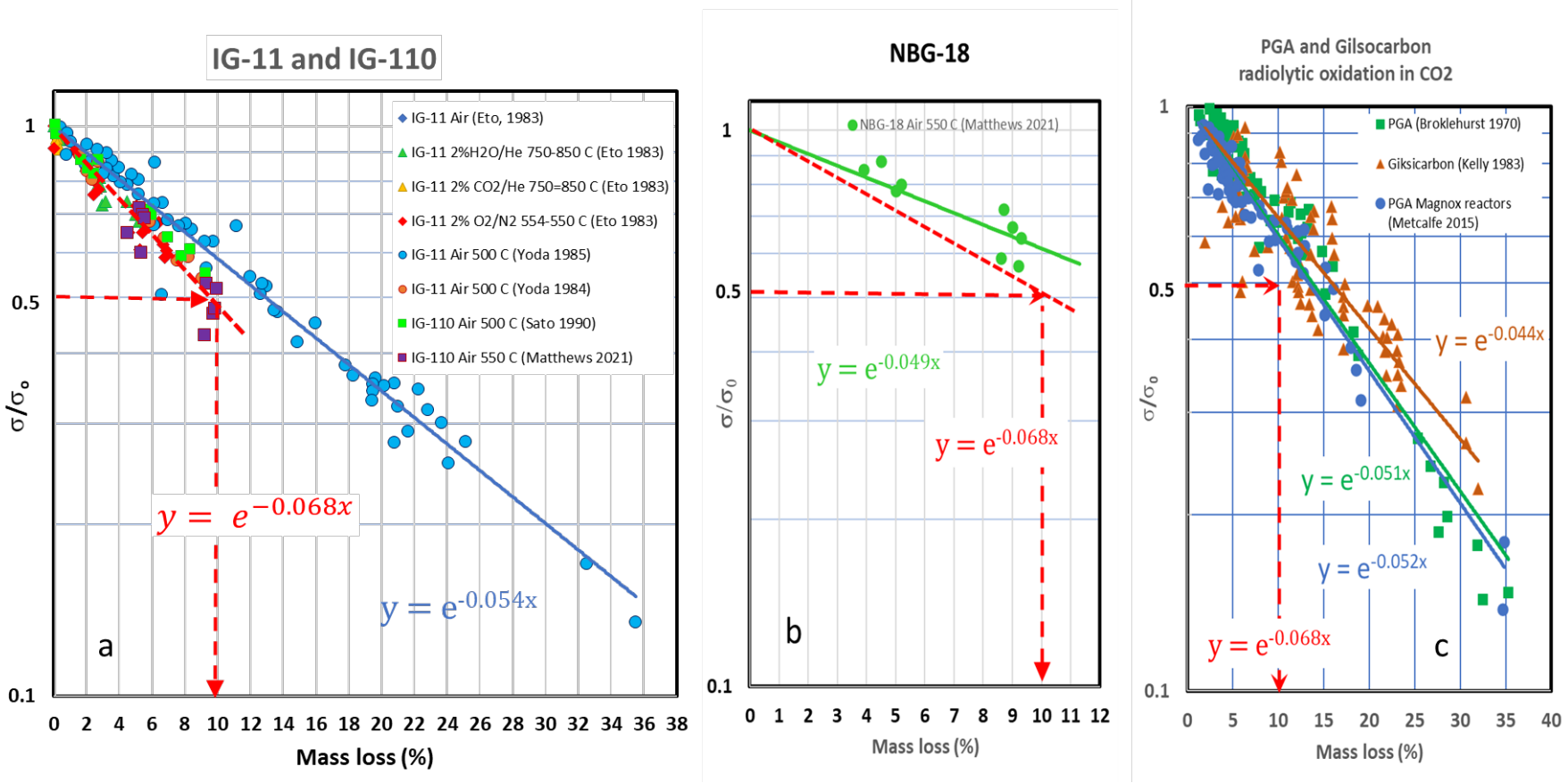

Figure 36. Compressive strength degradation versus weight loss after thermal and radiolytic oxidation. Results are shown for thermal oxidation in air of graphites(a) IG-11 and IG-110,[110,116,117,118,119] and (b) NBG-18;[119] and (c) results for radiolytic oxidation in CO_2 of graphites PGA and Gilsocarbon.[126,127,128] The red dashed lines indicate the rule of thumb correlation (n = 6.8). Oher equations show the best fitting of experimental points to an exponential equation.

5.2.2.2 Tensile strength and Young's modulus

Information on thermal oxidation effects on tensile strength and Young's modulus of modern grades of graphite is scarce. In general, the correlation of various properties (e.g., strength, Young's modulus, thermal resistance) versus oxidative mass loss can be modeled by the Knudsen's equation, as well.[120] Publications from JAERI provide details of mechanical properties of graphite IG-11 uniformly oxidized in air, such as compressive fracture strength and Young's modulus. Yoda et al. observed that the Young's modulus variation with the density of uniformly oxidized graphites follows a similar trend to the compressive strength, and both can be described by Knudsen's empirical formula (Figure 37).[110]

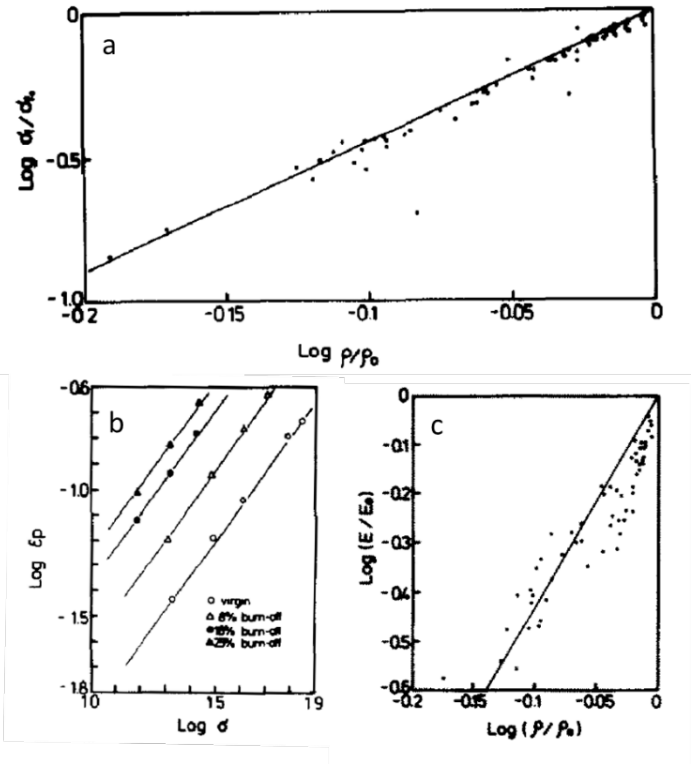

Figure 37. Effect of uniform oxidation in air on mechanical properties of IG-11. (a) Logarithmic variation of compressive fracture strength versus weight loss (or density); (b) stress–strain relationship from compressive tests of uniformly oxidized specimens with various weight loss levels; and (c) Young's modulus variation of uniformly oxidized specimens versus weight loss. (More information available in ref.[110]).

Another report by Yoda et al. shows double logarithmic plots of compressive and tensile strength versus the density for uniformly oxidized IG-11 (Figure 38).[117] The reported coefficients of Knudsen's equation for strength are $n = 4.28$ (compression) and $n = 3.95$ (tension), and for Young's modulus, they are $n = 4.28$ (compression) and $n = 4.64$ (tension). Both reports [110,117] contain numerical values tables for the flow stress under compression of unoxidized specimens, and for the flow stress ratios of oxidized to unoxidized specimens as a function of weight loss levels and various strain values. The ratios were almost constant, independent of strain.

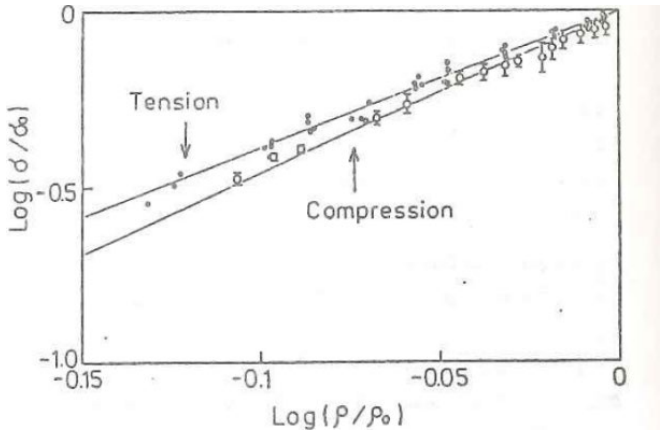

Figure 38. Logarithmic plots of compressive and tensile strength versus density for uniformly oxidized IG-11. (More information available in ref.[116])

5.2.3 Analysis of Density Gradients in Oxidized Specimens

In principle, the stress–strain relationship for specimens with nonuniform oxidation profile could be estimated, provided the density gradient along the radial direction and the correlation between mass loss and strength drop are known.[110,117] A condensed form of this calculation is shown below.

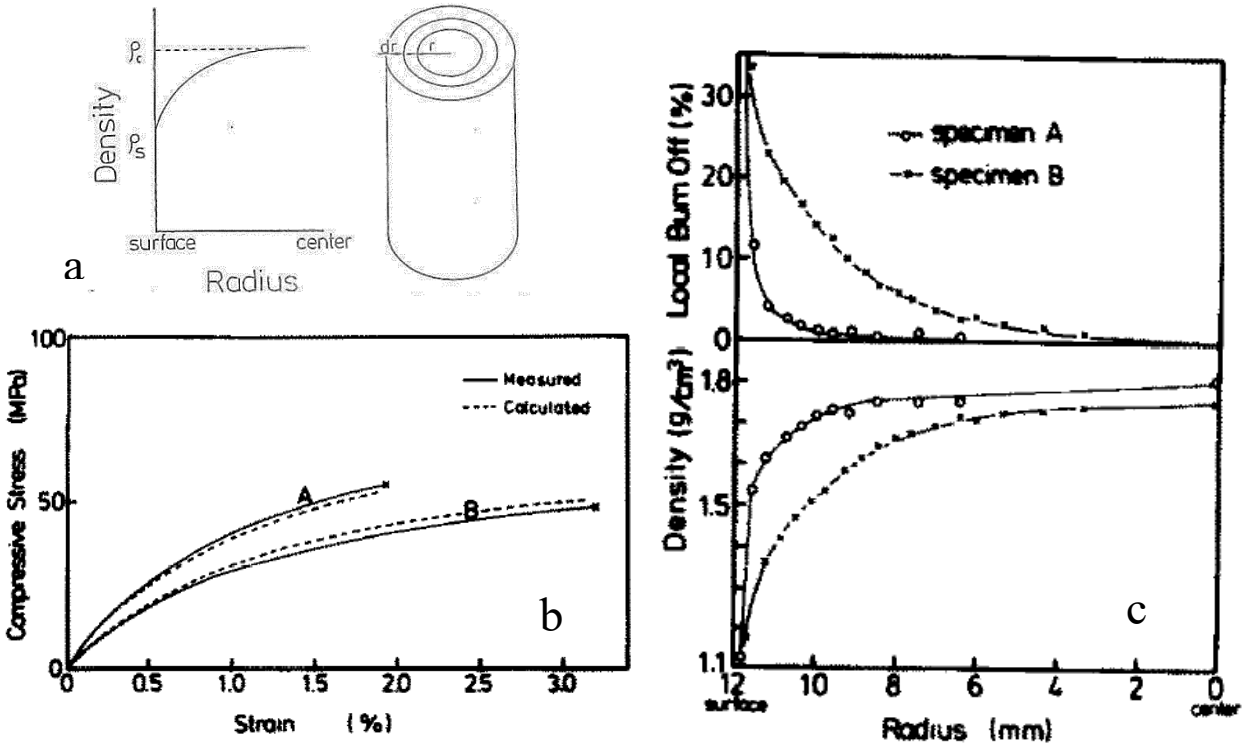

Figure 39. Estimation of density gradients on compressive strength of cylindrical specimens. (a) Schematic of a graphite cylinder with density gradient in the oxidized surface region; (b) comparison between experimental and calculated stress–strain profiles; and (c) specimens burn-off and density distributions measured experimentally. (Based on data from refs.[110,117])

For example, assume an isolated hollow cylinder in a larger cylindrical graphite body. The hollow cylinder has radii between r and r + dr, and the local density is ρ. If the axial compressive stress of the hollow cylinder is σ, the external load is dP = 2π$r\sigma$dr, and the total applied load is

$$P = \int 2\pi r\sigma dr \, . \tag{20}$$

However, if the radial density gradient is known from independent measurements, then r can be expressed as a function of ρ as

$$r = f(\rho) \, . \tag{21}$$

From these equations, P can be rewritten as

$$P = \int_{\rho_c}^{\rho_s} 2\pi\sigma f(\rho)\, f'(\rho) d\rho \, , \tag{22}$$

where ρ_c and ρ_s are densities at the graphite body's center and surface. Using the Knudsen's relationship (available from previous measurements), $\sigma/\sigma_0 = (\rho/\rho_0)^n$, where σ and σ_0 are strength values of regions with density ρ and ρ_0, respectively, the following relation is obtained:

$$\sigma(\varepsilon) = A\sigma_0(\varepsilon)\rho^n \, , \tag{23}$$

where $\sigma(\varepsilon)$ and $\sigma_0(\varepsilon)$ are the respective strengths at a given strain ε, and A is expressed as $A = {\rho_0}^{-n}$. After substitution, the following is obtained:

$$P = \sigma_0(\varepsilon) 2\pi A \int_{\rho_c}^{\rho_s} \rho^n f(\rho) f'(\rho) d\rho \, . \tag{24}$$

Here, P is the total load applied on a nonuniformly oxidized cylindrical specimen at strain, ε. Figure 39b shows two examples of experimental and calculated stress–strain curves for IG-11 specimens oxidized at two mass loss levels and with the density gradients shown in Figure 39c.[110]

Notably, the described procedure was not independently tested. It requires more experimental verification before it can be recommended for engineering calculations.

5.3 DEGRADATION OF OXIDIZED GRAPHITE IG-110 PROPERTIES

Degradation of fracture mechanics properties of graphite IG-110 caused by oxidation was amply characterized in a 1990 report by researchers in Japan.[129] They used circular discs (30 mm D, 3 mm H) for fracture toughness in mode I and II (K_{IC} and K_{IIC}), thermal shock resistance, and thermal shock fracture toughness tests; long rods (8 mm D, 80 mm H) for bending strength and Young modulus tests; and short rods (8 mm D, 16 mm H) for compressive strength tests. These specimens were oxidized in air to nominally 2.5% and 7.5% weight loss. Based on the density change, the oxidation was considered relatively uniform in the bulk. Measurements were conducted by various methods, including the diametral compressive strength using disc specimens. All results were interpreted according to Knudsen's general equation written as

$$S = S_0 \exp(-n\, b) \, , \tag{25}$$

where S and S_0 are the properties of oxidized and virgin material, and b is the fractional weight loss. Figure 40 shows the relative change of Young's modulus, bending strength, diametral compressive strength (which expresses the maximum tensile stress inside the disc), and compressive strength. Some results measured by

JAERI are also reported for comparison. The difference between the results available from the two sources was attributed to possible differences in graphite properties between lots and the non-homogeneity of graphite billets. Figure 41 shows the change in mode I to mode II fracture coefficients ratio. Figure 42 shows variation of fracture toughness in mode I and mode II as a function of weight loss percentage of uniformly oxidized IG-110.[129]

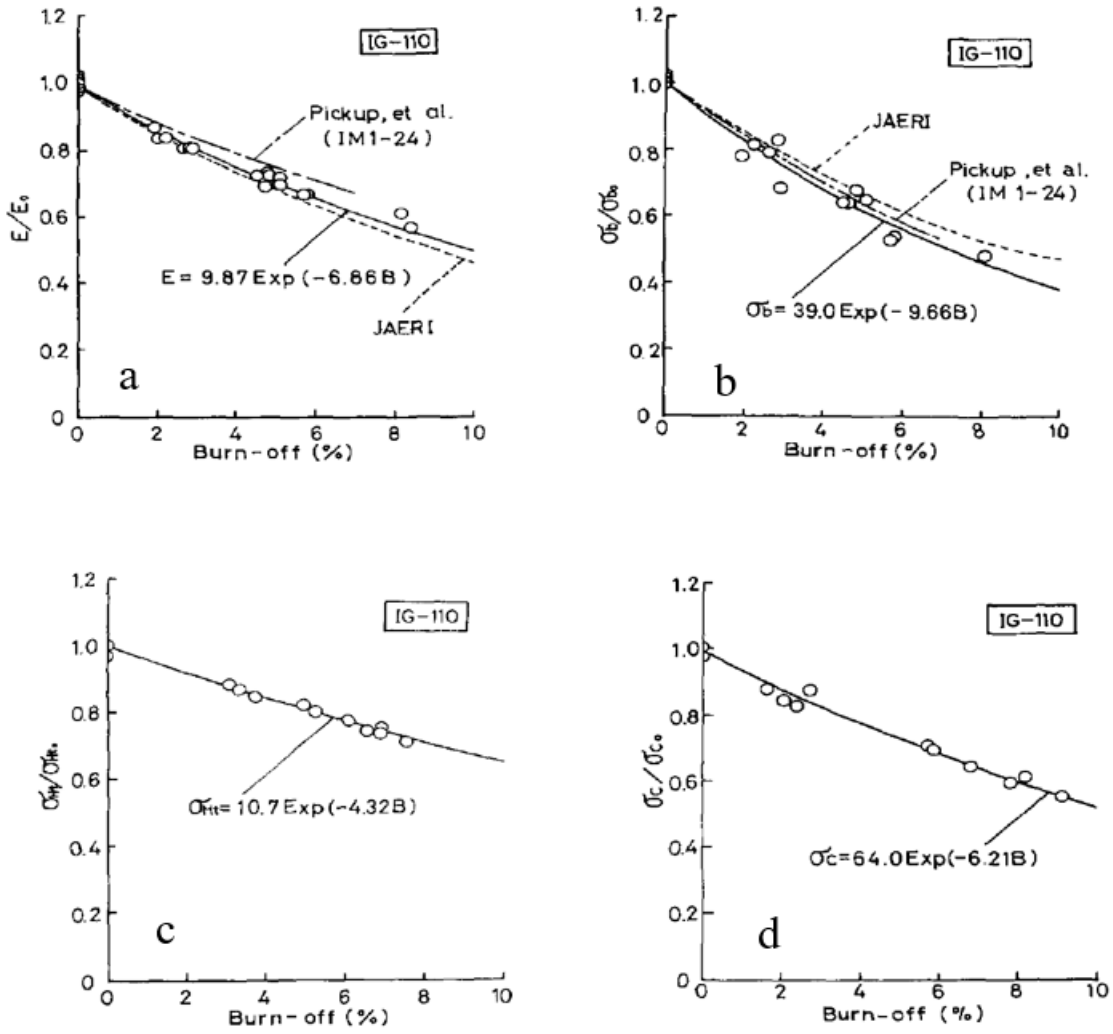

Figure 40. Mechanical properties of uniformly oxidized IG-110 specimens. (a) Young's modulus; (b) bending strength; (c) diametral compressive strength; and (d) compressive strength as a function of weight loss percentage. (More information available in ref.[129])

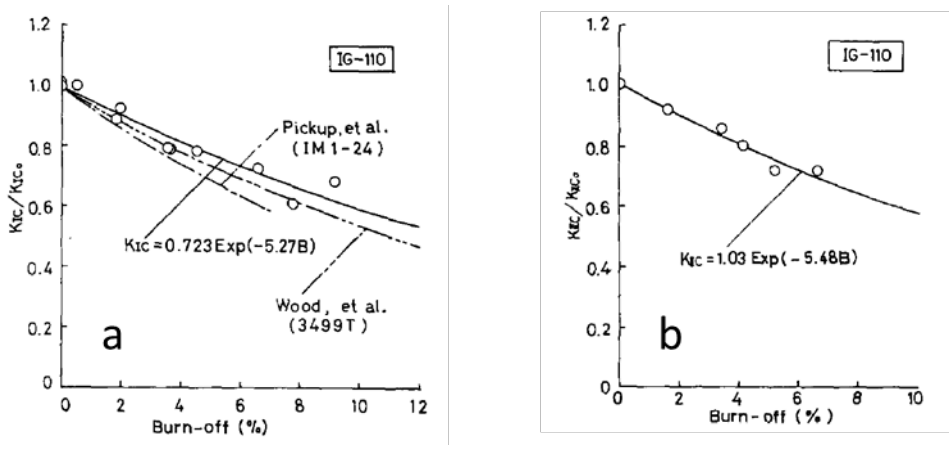

Figure 41. Change of mode I to mode II fracture coefficients ratio of uniformly oxidized IG-110 specimens as a function of weight loss percentage. (a) Mode I and (b) mode II. (More information available in ref.[129])

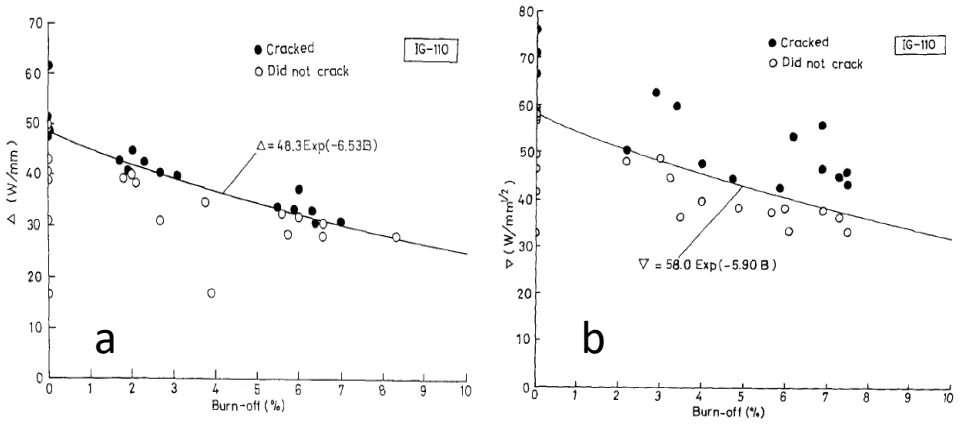

Figure 42. Change of thermal shock properties uniformly oxidized IG-110 as a function of weight loss percentage. (a) Thermal shock resistance and (b) thermal shock fracture toughness (More information available in ref.[129])

Table 7. Graphite IG-110 material constants S_0 and n in Knudsen's equation.[129]

		IG-110	
		S_0	n
Young's modulus	E (GPa)	9.87	6.86
Bending strength	σ_b (MPa)	39	9.66
Compressive strength	σ_c (MPa)	64	6.21
Diametral compressive strength	σ_{Ht} (Pa)	10.7	4.32
Mode I fracture toughness	K_{IC} (MPa m$^{1/2}$)	0.723	5.27
Mode II fracture toughness	K_{IIC} (MPa m$^{1/2}$)	1.03	5.48
Thermal shock resistance	Δ (W/mm)	48.3	6.53
Thermal shock fracture toughness	∇(W/mm$^{1/2}$)	58	5.90

Table 7 describes the material constants for virgin properties (S_0) and the exponent (n) in Knudsen's equation. Table 8 presents the parametric variation of thermal shock resistance and thermal shock fracture toughness for IG-110 specimens oxidized as various levels of weight loss. Both these tables contain data from the above cited paper by Sato et al. [129]

Table 8. Variation of thermal shock resistance and fracture toughness of uniformly oxidized graphiteIG-110 up to 10% weight loss[129]

		Weight loss %					
		0	**2**	**3**	**5**	**8.5**	**10**
Tensile strength	σ_t (MPa)	25.5	21	20.7	19.4	174	15.5
Thermal conductivity	k (W/mK)	128	89	80	66	53	49
Young's modulus	E (GPa)	9.87	8.6	8.03	7	3.51	4.97
Coefficient of thermal expansion	α ($\times 10^{-6}$/K)	4.9	4.75	4.68	4.58	4.46	4.38
Mode I fracture toughness	K_{IC} (MPa m$^{1/2}$)	0.723	0.651	0.617	0.536	0.462	0.427
Thermal shock resistance	Δ (W/mm)	48.3	42.4	39.7	34.8	27.7	25.1
Thermal shock fracture toughness	∇(W/mm$^{1/2}$)	58	51.5	48.6	43.2	25.1	32.2

In another report, researchers at JAERI examined the high-temperature Young's modulus of pre-oxidized and pre-stressed graphite IG-110 specimens.[130] Oxidation was performed in air up to 10% weight loss; at this temperature, oxidation was slow, and the bulk was uniformly oxidized. Pre-stress levels were 60 % or 80 % of the mean compressive strength. Both oxidation and pre-stressing decreased the Young's moduli at room temperature and at high temperatures. This decrease was explained by cracks opening and growing. The following empirical equation was proposed, by which the high temperature moduli of oxidized specimens could be estimated from the room temperature moduli of the unoxidized specimens:

$$\frac{E(T,d_0)}{E(RT,\,d_0)} = f(T) = 0.999 - 2.43\times10^{-5}T + 1.275\times10^{-7}T^2 + 8.885\times10^{-12}T^3\,, \qquad (26)$$

where $E\,(T, d_0)$ and $E\,(RT, d_0)$ are moduli of unoxidized specimens at temperature T and room temperature (RT), respectively. Assuming that the Knudsen's relationship is valid not only at room temperature, but also at higher temperatures, the following relationships were found for the variation with temperature of the exponent n:

$$n(T) = 6.579 + 1.34\times10^{-3}\,T\,, \qquad T \le 800°\text{C}\,, \qquad (27a)$$

$$n(T) = 7.540 + 6.82\times10^{-5}\,T\,, \qquad T > 800°\text{C}\,. \qquad (27b)$$

The respective variations (at various levels of weight loss) are shown in Figure 43a. From Eqs. 27a and 27b, the modulus of oxidized specimens at any temperature T can be determined:

$$\frac{E(T,d)}{E(RT,d_0)} = f(T)\left(\frac{d}{d_0}\right)^{n(T)}\,, \qquad (28)$$

where the function $n(T)$ is plotted in Figure 43b.

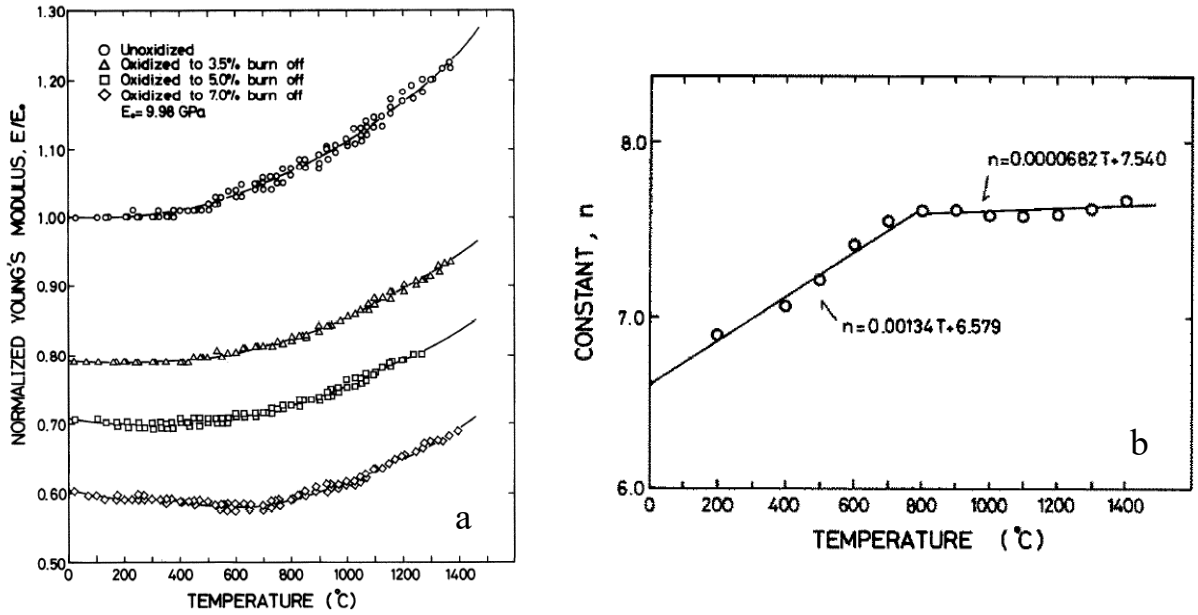

Figure 43. Temperature dependence of Young's modulus of uniformly oxidized IG-110 samples. (a) Effects of oxidation weight loss; and (b) temperature dependence of the exponent in Knudsen's equation for Young's modulus. (More information available in ref.[130])

The hysteretic changes of Young's modulus of specimens during heating and cooling are recorded in Figure 44a for unoxidized specimens and for specimens oxidized to 5 % weight loss. The hysteresis loop was more pronounced for oxidized specimens than for non-oxidized ones. Another interesting observation relates to the effect of annealing on the modulus recovery from various temperatures (Figure 44b). Annealing was done in vacuum between 200 °C and 1800 °C.[130]

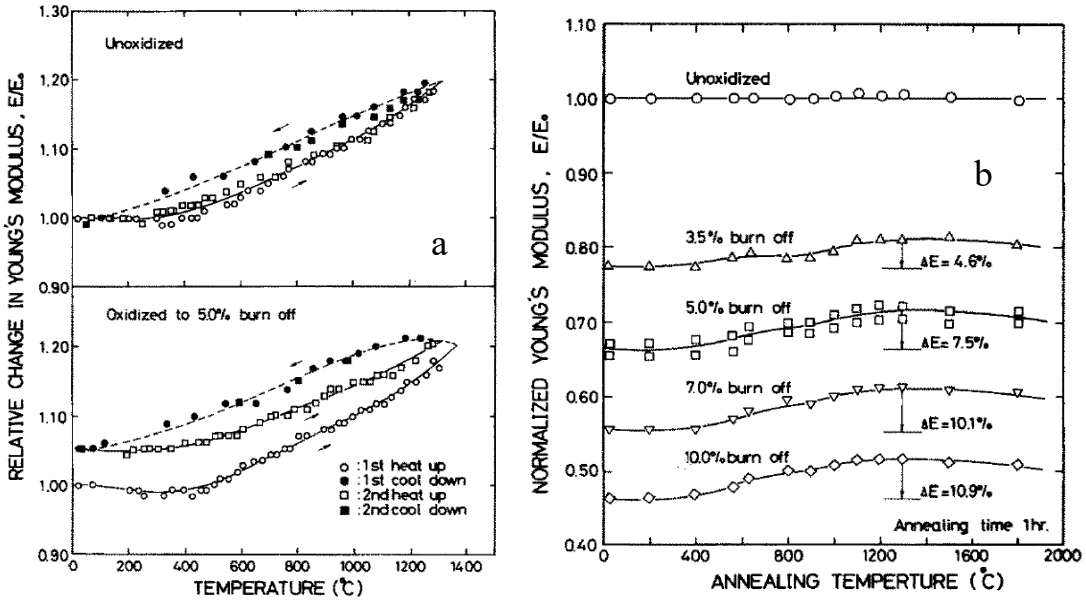

Figure 44. Temperature effects on Young's modulus of virgin and oxidized IG-110 specimens. (a) Hysteresis loops between heating and cooling of virgin and oxidized (to 5% weight loss) IG-110 specimens; and (b) changes of Young's modulus versus annealing temperature for unoxidized specimens and specimens oxidized at various weight loss levels. (More information available in ref.[130])

Recently, the relationship between elastic moduli of oxidized graphites IG-110 and NBG-18 and the corresponding weight loss (or density) values was reexamined based on physics-based models and compared against new experimental measurements using contact-free ultrasonic methods. The new effective medium model for graphite, as a polycrystalline porous solid, proposed by Olasov and Spicer[131] provides a more rigorous theoretical justification of the observed elastic moduli behavior. The model is based on the concept that oxidation not only causes porosity development, but also preferentially changes specific portions of the microstructure, and introduces or enlarges preexisting microcracks.

Figure 45a shows experimental results for elastic and shear moduli of oxidized graphites at various levels of weight loss and their predicted variation derived from the new model.[131] Similar dependence of Young's modulus for oxidized IG-110 specimens was reported earlier by Eto et al.,[130] who used power law functions to represent the drop of Young's modulus with the change in density, as shown in Figure 45b for oxidized and oxidized and annealed (1300 °C) specimens. The power law function is a practical and convenient data fitting model for degradation of mechanical properties after oxidation (as shown in Figure 40, Figure 41, and Figure 42), but it is only partially justified on theoretical grounds.[131] In contrast, the model for the linear elastic response of polycrystalline graphite with pores and microcracks is a better representation of physical and chemical effects of graphite oxidation. This model is presented in Figure 45c and Figure 45d, where Young's modulus data from Figure 45b are replotted on a linear scale and compared with the power law fitting used by Eto et al.[130] and the predictions of the new model.[131] Although the overall behavior and the goodness of fit are similar, the new physical model developed by Olasov and Spicer[131] is better linked to the microstructural oxidation processes and specific structural changes that selectively affect the elastic response.

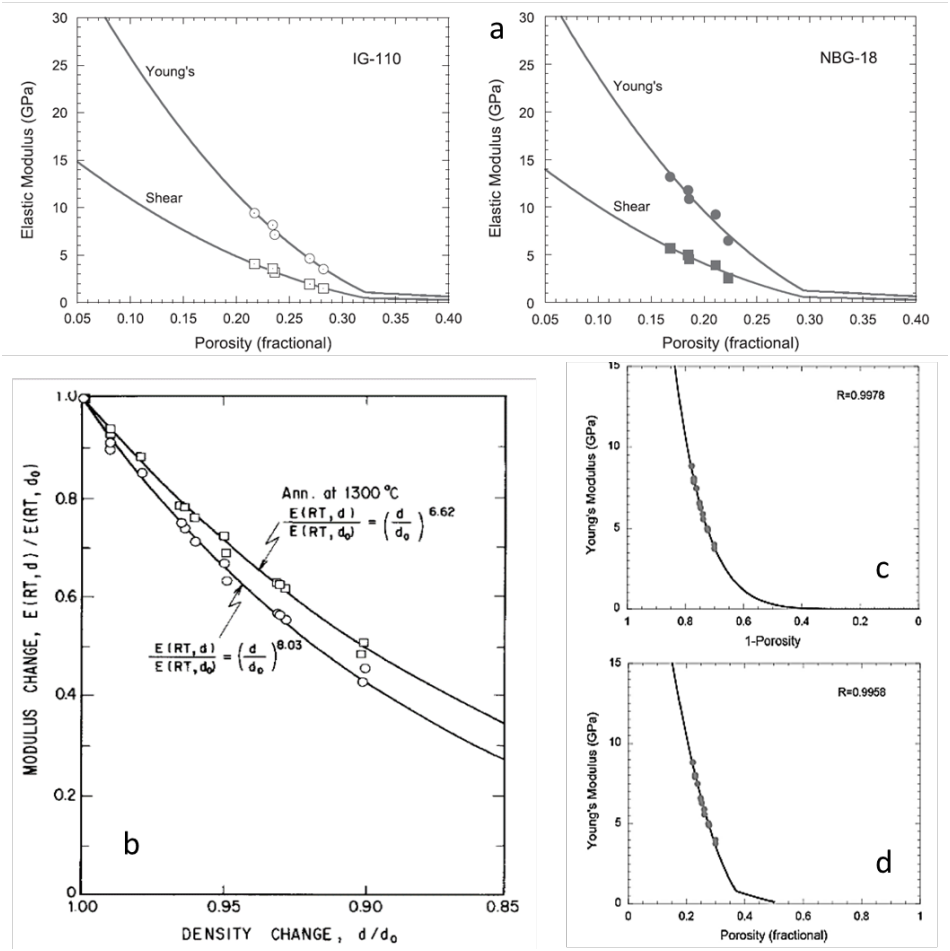

Figure 45. Effects of oxidation by air on elastic moduli of nuclear graphites. (a) Experimental results[131] for the variation of Young's and shear moduli of IG-110 and NBG-18 oxidized by air as a function of porosity; (b) Room temperature Young's moduli of as-oxidized and oxidized and annealed (from 1300°C) IG-110 specimens as a function of oxidative density changes;[130] (c) Fit of room temperature data from (b) using Eto's power law model;[130] (d) Fit of same data from (b) using Olasov-Spicer's physics-based model.[131] (Data compiled from refs.[130,131])

Laser ultrasonic methods have the advantage that they can be deployed in the reactor core for examination of graphite components' health condition during periodic revisions and refueling campaigns. This contact-free technique requires only optical access to graphite components' exposed surfaces, and the measurements can be done by robots. In addition, measurements by contact-free ultrasonic measurements do not require the removal of oxidized ends like had to be done for the compressive test specimens.

6. BRIEF REVIEW OF OXIDATION MODELS

6.1 EXPECTATIONS

Design criteria and safety analysis of graphite components requires reliable graphite oxidation models. Development of such models must start from a good understanding of oxidation mechanisms and the effect of various determining factors and should be supported by accurate, verifiable, reproducible experimental data. Even if the basic mechanism is well understood and correctly formalized as a mathematical algorithm, the output of the oxidation model will be as good as the quality of the experiment-derived input information used for model validation. With this caveat, the models should be able to predict graphite's oxidation behavior at conditions beyond those used for its validation. In addition, it is expected that a model validated for one graphite material should be used to predict accurate information on another graphite's behavior in similar or related oxidation conditions and with properly accounting for the material properties of the second graphite. Model translation between graphite grades (with updated material properties) should be feasible, which requires that the intrinsic properties and behaviors of the two graphite grades have been reliably understood and accurately characterized.

6.2 CHALLENGES OF DEVELOPING OXIDATION MODELS

The complex nature of graphite oxidation processes is a serious challenge for development of a universal oxidation model that can be applied to any graphite grade at any process condition. Ideally, such a model should be robust, comprehensive, and versatile, and it should provide accurate results that can be easily integrated in the broader modeling scenarios for reactor operation.

This task is marred by multiple challenges rooted in the variability of graphite materials (between lots, between billets, and even between positions in the billets). The oxidation process itself causes structural changes in the graphite components, which vary both with time (or the history of the oxidation process) and with position (the distance from the surface). Correct prediction of time dependence of the oxidation process, which includes pore structure evolution and dimension changes, requires informed knowledge on in-pore transport and interfacial mass transfer processes. That prediction is challenging because some characteristic parameters can only be accurately measured for the unoxidized material (effective diffusivity reduction factor β, porosity fraction ε), and others are inferred by analogy with processes that can be more easily characterized (e.g., interfacial heat transfer as a surrogate for mass transfer at high temperatures).

Besides material properties, a multitude of other factors related to specific conditions and practical situations complicate the development of these models. Shape and size of graphite bodies seem to be the easiest factors to account for, but they are interdependent, and their significance depends on the balance between chemical reaction rates and in-pore transport rates. The same oxidation conditions (temperature, oxidant concentration and supply rate) might be expected to not produce significantly different results between small laboratory-scale specimens and massive graphite components, so that the information from laboratory experiments can be reliably translated to large size components. However, that expectation is most of the times inaccurate. Oxidation of small specimens may penetrate their whole volume if a specimen's characteristic size is comparable to the oxidant penetration depth at steady-state conditions. In contrast, large-volume components are affected only near their surface, whereas a significant fraction in the core may not be reached by the oxidant. Scalability of oxidation models, from laboratory experiments to full-sized components, remains an open problem. A change of the coordinate system may help: if cylindrical coordinates are appropriate for small size specimens, the large components should be treated as semi-infinite slabs.[74,75,76]

The oxidant supply rate and the flow conditions in the gas phase are often neglected from analysis, but they are not less important than the solid-phase properties. At one extreme, oxidant starvation conditions may

develop at high temperatures if the oxidant supply rate is kept constant while the oxidant chemical consumption rate increases exponentially with temperature. Examples from Section 4.3 show the effect of the often-neglected relationship between the ratio of oxidant supply to carbon gasification rates on the transition between chemical kinetics control (Regime 1) to in-pore diffusion control (Regime 2). In other words, the range of temperatures where the Arrhenius model can be applied is highly dependent on circumstantial parameters, as demonstrated with examples from the literature in Figure 13.

Another complication relates to the gas phase itself. The oxidant concentration in the outmost graphite layer is typically assumed to be the same as the gas-phase concentration. This assumption is accurate at low temperatures, where the interfacial mass transfer is not limited by a stagnant layer near the surface. With an increase in temperature, the mass transfer resistance also increases, and the oxidant concentration in the outmost graphite surface layer is diminished from the free gas concentration. This variation must be included in the calculations but is sometimes neglected. The flow regime (laminar of turbulent) referenced by the Reynold's number, and the convective versus diffusive mass transfer rate at gas/graphite interface (referenced by Sherwood's number) become highly significant for modeling of graphite oxidation in the regime of boundary layer control (Regime 3).[132]

6.3 OXIDATION MODELING TRENDS

Most graphite oxidation processes of interest for their potential safety consequences are expected to occur in the diffusion-controlled regime (Regime 2). However, modeling in this regime is the most challenging because of the lack of a general model. Modeling should simultaneously consider two competing processes:

- Chemical reaction, whose rate depends on local oxidant concentration at the reactive graphite surface and on temperature

- Oxidant transport (diffusion) through the open pore system of graphite, which depends on average pore size, pore connectivity, pore tortuosity, and temperature

The slowest process is always rate controlling. Temperature has stronger effects on chemical rates, which increase faster than diffusion rates. The competition between the two processes determines the transition temperature from Regime 1 (chemical control) to Regime 2 (in-pore diffusion control) as temperature increases. The examples from Figure 13 show that the transition temperature is not significantly dependent on graphite properties; rather, it is more strongly affected by circumstantial conditions (such as oxidant supply rate, specimen size and shape, and even the laminar or turbulent character of the oxidant gas flow). With the progress of oxidation, more porosity is opened, a larger internal surface becomes accessible for chemical attack, and these structural changes determine changes in the transport rate. The transient oxidation regime of early oxidation stages is replaced by a steady-state condition lasting from approximately 5 % up to approximately 35–40 % weight loss. Beyond this point, oxidation rates decrease as pores collapse in advanced oxidation stages. Conversely, as temperature increases and overall oxidation rate is limited more and more by the in-pore diffusion rate, the gas phase oxidant supply and the mass transfer rate through the boundary layer start having a greater effect that opposes the exponential increase of chemical rates with temperature.

There are several basic fundamentally different approaches for modeling graphite oxidation in Regime 2:

- One approach is to start with well-characterized chemical rates, measured as much as possible in diffusion-free conditions, and then to include the effect of in-pore diffusion. This method uses reasonable estimates of concentration gradients across the oxidized layer based on best-estimate values for the effective oxidant diffusivity through the porous system. This material-focused

approach is equivalent to treating in-pore diffusion-controlled oxidation (Regime 2) as a transport-perturbed case of chemically controlled oxidation (Regime 1).

- In another approach, oxidation in Regime 2 is regarded as a relaxed case of transfer-limited oxidation in the boundary layer (Regime 3). Depending on gas flow conditions (laminar or turbulent, based on Reynold's number) and other factors, the oxidant concentration at the graphite surface may be different from the gas-phase concentration. This approach places emphasis on gas phase CFD models, which provides local values for oxidant concentration as a function of position, time, and temperature. This method is an engineering-focused approach useful for accident scenario analysis and safety assessment based on selected initial conditions.

- A balanced approach has also been proposed in which oxidation in Regime 2 is regarded as a superposition of oxidation in Regimes 1 and 3.

- Other approaches have also been proposed from various perspectives on the graphite oxidation process. They diverge from one another, such as by using the intrinsic kinetic characteristics of the $C + O_2$ oxidation reaction; by analyzing the graphite porosity evolution at the microstructure level; by using semi-global treatment of chemical reactions with probabilistic rather than deterministic methods; and by simultaneously analyzing multiple interdependent physical and chemical processes using advanced multiphysics methods.

These various approaches are briefly summarized in the following paragraphs. The intent was to outline the advantages and limitations of the most significant developments by the time of this writing rather than to offer in-depth guidance on each approach.

6.3.1 Material-based Approach

There are several excellent reviews on oxygen reactions with porous graphite materials.[4,31,41,66] As they are discussed briefly here, some repetition of the above-introduced information could not be avoided. The general rate of oxidation rates in Regime 1 (chemical control at low temperature, diffusion perturbations neglected) was introduced above as Eq. (2):

$$Rate_1 = K_1 (P_{ox})^n F_b = k_0 \exp\left(\frac{-E_{app}}{RT}\right) (P_{ox})^n F_b \qquad (2')$$

The transient function that describes the acceleration of the oxidation rates during the onset stage (from the initial contact with oxidant up to about 5 % weight loss) was modeled by many researchers according to the 2D RPM introduced by Bhatia et al. as Eq. (7):

$$F_b = \frac{dX}{d\tau} = (1 - X)\sqrt{1 - \Psi \ln (1 - \mathrm{X})}\,, \qquad (7')$$

which is more of a data fitting exercise than a true material property definition. A promising alternative is the 3D RPM developed by Paul, which is consistently grounded in graphite microstructural properties and the proven mechanisms of pore evolution during oxidation.[46,47,48] This microstructural-dedicated approach is discussed in Section 6.3.6.

The 2D and 3D RPMs both satisfactorily reproduce experimentally observed variations of oxidation rates with time (see Figure 8) or mass of the remaining unoxidized graphite (see Figure 7). Such information was implicitly collected in all oxidation tests performed according to ASTM D7542. The dependence on size and shape of graphite specimens (see Figure 9 and Figure 10) is still not fully understood, but there is

sufficient experimental data to use for validation of those oxidation models to examine this question in the near future.

In the material-focused approach, the oxidant diffusion is treated as a local perturbation of the kinetically controlled regime, which slows the observed rates compared with the hypothetical diffusion-free conditions. An example is provided in Figure 46**,** which shows experimental results on oxidation of hollow graphite cylinders at three temperatures between 435 and 485 °C.[133] This figure compares the variation with temperature of the measured oxidation rates and of the diffusion-free chemical reaction rate (corrected by the Thiele efficiency factor). When the oxidant diffusion rate becomes comparable with the oxidant consumption rate in chemical reactions, a concentration gradient of oxidant is established inside the graphite bulk. The oxidant transport and its consumption in chemical reactions are balanced as described by the following general equation:

$$\frac{\partial(\varepsilon C_{ox})}{\partial t} = \frac{1}{\partial x} D_{eff} \left(\frac{\partial C_{ox}}{\partial x}\right) - Rate \quad \rho\nu \,, \tag{29}$$

where C_{ox} is the local oxidant concentration, ε is the local void fraction, ρ is the local graphite density, and ν is the stoichiometry coefficient of the chemical reaction. The notation *Rate* for the local chemical rate is a placeholder. It may be replaced with $Rate_I$, the general expression of the oxidation rate in chemical regime from Eq. (2). For more complex reaction mechanisms in which accumulation of reaction products slows (inhibits) the main reaction, one can use $Rate_{LH}$ from Eq. (10) for the LH kinetic model, or $Rate_{BLH}$ from Eq. (12) for the BLH mechanism, or any other correlation that is demonstrably applicable, such as Eq. (15).

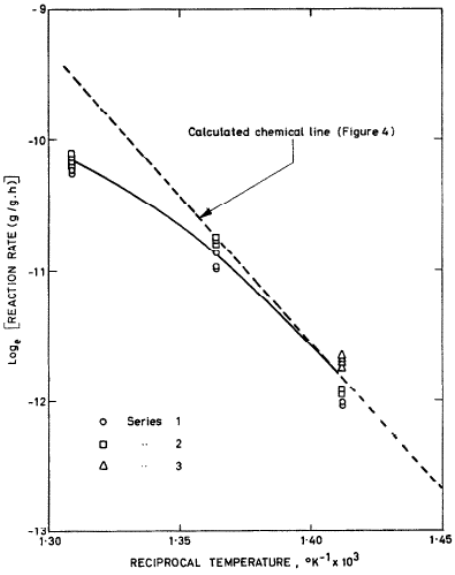

Figure 46. Variation with temperature of observed oxidation rate and of chemical reaction rate. Hollow nuclear graphite cylinders were oxidized in air at 435 °C, 460 °C, and 485 °C. (Data from ref.[133])

Finding analytical solutions for Eq. (29) is possible with several simplifying assumptions, including neglecting effective diffusivity variation during oxidation (equivalent to assuming constant graphite density in the active oxidation zone) and using a linearized expression for *Rate* as in Eq. (2). Wichner et al.[74,75] showed that, with these simplifications, the oxidant concentration profile (and the corresponding graphite density profile) can be estimated as a function of temperature, as shown in Eq. (17). The graphite density profiles estimated by this route have been successfully compared against direct density measurements in the oxidized layer.[106,112] In the case of chronic oxidation by moisture in helium, the simplifying assumptions described above were not violated as long as the weight loss was low, and a good agreement was obtained

between estimated density profiles and direct measurements (see Figure 24 and Figure 25). In that example, the D_{eff} have been measured in separate experiments with unoxidized graphites, and any further variation with the progress of oxidation by moisture was neglected as long as the weight loss was below 1–1.5 %.

In Germany, Hinssen and Moormann[31] obtained numerical solutions of Eq. (29) using the LH kinetic equation for the *Rate* term and compared the results with experimental oxidation rates by air of a 2 cm sheet of German nuclear graphite V483T. Figure 47 shows that diffusion permeability increases with the oxidative weight loss, and that simultaneously more low-dimension pores contribute to diffusional transport. These changes modify the O_2 concentration profiles as shown in the right panel of Figure 47. At 800 °C, oxidation was in Regime 2. With the increase of weight loss (oxidation time), the oxidant profiles changed from the initial exponential decay shape (after first 2000 s) to sigmoidal shapes. The gradual shift inward from the exposed surface with every 4000 s oxidation time increment indicates dimensional shrinkage caused by erosion. The case with the neglect of erosion is represented by curve H in Figure 47, which reveals a boundary layer effect up to 6 mm from the surface. This penetration depth is larger than what would have been estimated with the neglect of transitory rates acceleration in the initial onset stage. Although modeling provided partial agreement with the experimental data, the authors emphasized that more theoretical and experimental work was needed to develop fully predictive models of graphite oxidation in Regime 2.[31]

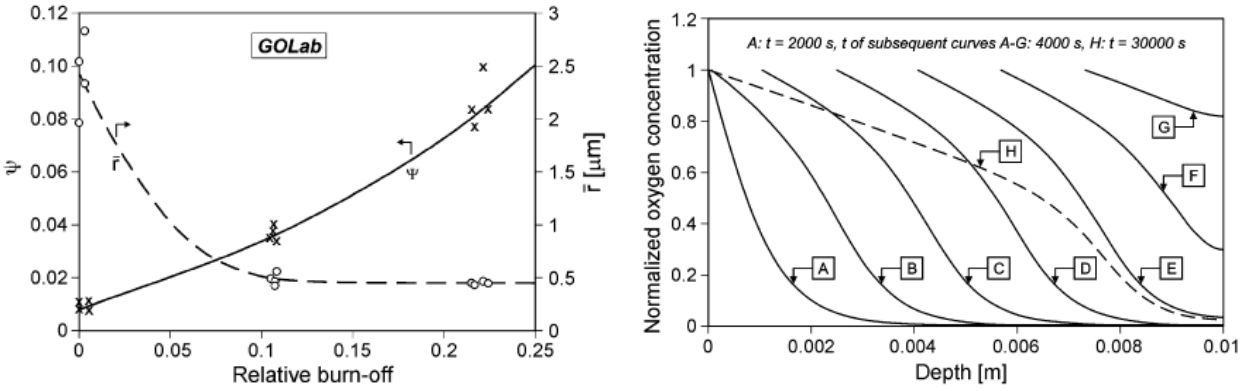

Figure 47. Measured structural changes and calculated oxidant profiles for graphite V483T oxidized by air. Left: Weight loss dependence of diffusivity reduction factor ($\Psi = D_{eff}/D_{\text{free gas}}$) and average radius of transport pores; Right: Oxygen profiles at 800 °C in air (A at t = 2000 s; subsequent curves B–G at 4000 s increment; H at 30,000 s). (Data from ref.[31])

In China, transient analysis of IG-110 oxidation was carried out in a similar manner for safety analysis of the pebble-bed modular reactor HTR-PM.[134] Following the model presented by Wichner et al.,[74,75] a system of partial differential equations that combines oxidant conservation, porosity development, and linearized consumption rates for O_2 and C was solved numerically:

$$\frac{\partial(\varepsilon C_{O2})}{\partial t} - \nabla\left(D_{eff}\nabla C_{O2}\right) = \text{Rate}_{O2}\,, \qquad \text{oxidant conservation,} \qquad (30)$$

$$\varepsilon = \varepsilon_0 + (1-\varepsilon_0)b\,, \qquad \text{porosity development,} \qquad (31)$$

$$\text{Rate}_{O2} = -z\frac{\rho_C}{M_c}Ae^{-E_a/RT}TF_bC_{O2}\,, \qquad O_2 \text{ consumption rate,} \qquad (32)$$

$$\frac{\partial b}{\partial t} = Ae^{-E_a/RT}TF_bC_{O2}\,, \qquad \text{graphite oxidation rate.} \qquad (33)$$

Although similarities exist between Eqs. (29) and (30) and between Eqs. (2) and (32), the full set of differential equations was reproduced here for completeness. The boundary conditions were selected for spherical IG-110 pebbles (radius 3 cm), and the calculated oxidation rates were compared against experimental rates for oxidation in air of cylindrical specimens machined according to ASTM D7542.[50] The match was not good, as Figure 48a shows. The calculated rates were always higher than the experimental rates. The deviation is caused by the neglect of the boundary layer transfer in the simplified oxidation model, which reduces oxidation rates at high temperatures (Regime 3). Nevertheless, according to this model, O_2 penetration depth decreases with temperature: only 100 s after the oxidant attack, the predicted penetration depths were stabilized at 3 cm at 500 °C, 1.25 cm at 600 °C, 0.5 cm at 700 °C, and 0.25 cm at 800 °C (Figure 48b).[134]

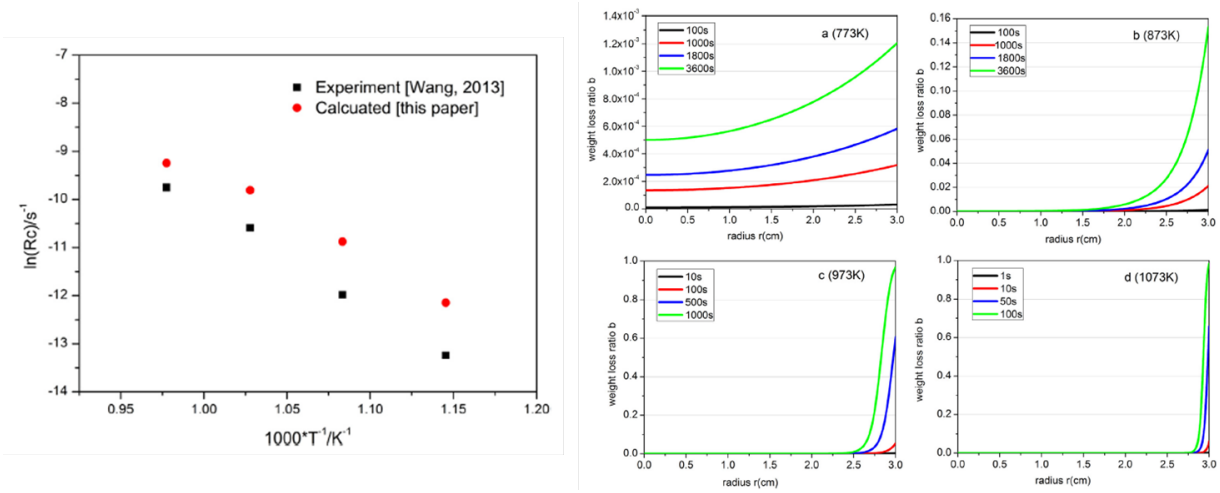

Figure 48. Model calculations for graphite IG-110 oxidation in air. (a) Comparison of experimental oxidation rates with the rates calculated by a simplified model. (b) Transient evolution of O_2 penetration depths at various temperatures. (More information available from ref.[134])

Oxidation models based on the material-focused approach were incorporated in several computer codes designed to model oxidation behavior of reactor graphite components. Early codes, such as GRSAC developed at ORNL,[41] OXIDE-3 developed by General Atomic Company,[135] and MELCOR modified by Sandia National Laboratories and INL[136] [137] have been upgraded with graphite oxidation subroutines that combine oxidant consumption and transport rates with CFD calculations for particular thermal-hydraulic conditions associated with postulated accident events.

6.3.2 Chemistry-based Approach

In the United States, El-Genk and Tournier at the University of New Mexico focused on the evolution of chemical species during graphite oxidation by air. They compared kinetics and thermodynamics of elementary carbon oxidation reactions against the rates of oxidant supply to the graphite surface, and they derived kinetic parameters of elementary reactions such as O_2 adsorption and CO and CO_2 desorption.[138,139,140,141,142,143] Rather than using empirical parameters that greatly depend on experimental circumstances, they assumed that specific activation energies and rate constants of each elementary reaction have a Gaussian-type distribution around a mean value (Figure 49a,b). The model assumes that the chemical reaction mechanism is the same for all types of graphite (or carbon), but the particular values of kinetic parameters are specific to the type of nuclear graphite. They combined material-specific and experiment-dependent factors into an adjustable parameter (i.e., initial active sites surface area, ASA_o), which is included as input of the kinetics gasification model. ASA_0 characterizes the initial reactivity of graphite grades and varies with weight loss. The transient variation of ASA during gasification– was modeled using the 2D

random pore model (Figure 49c,d). On those grounds, chemical kinetics parameters for multiple nuclear graphite grades – namely IG-110, IG-430, NBG-25,[139] NBG-18,[143] and PCEA[142] – have been determined by a multi-parameter optimization algorithm applied to global oxidation rates and transient weight loss data reported by various sources. With the appropriate parameters, the model simulates transient variation of gasification rates during the onset oxidation stage, but it can also predict the evolution of oxidation rates and the transitions between oxidation regimes with temperature (Arrhenius plots) for specific, experiment-determined conditions. Moreover, the model can also estimate the ratio between gasification products, CO and CO_2, as a function of temperature (Figure 49e,f). The model was validated with experimental data reported in the literature for several graphite grades. Simulations were successfully demonstrated for a variety of experiment conditions (including initial mass and shape of graphite specimens, air supply rates, and specific flow conditions in the oxidation reactor).

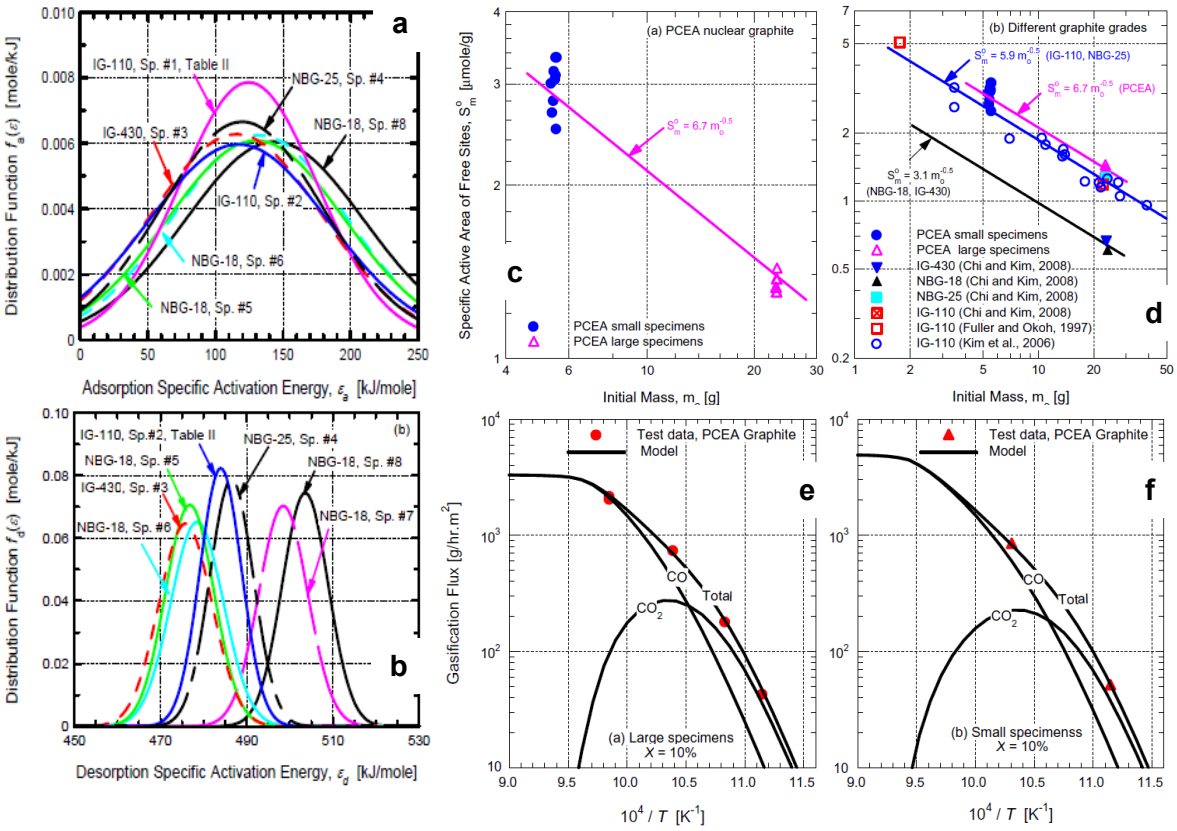

Figure 49. Example of results of chemical reactions-kinetics model. Distribution function of specific activation energies for O_2 (a) adsorption and (b) desorption on several graphite grades;[139] Variation of specific active area of free sites with initial mass of (c) PCEA and (d) other graphite grades in selected examples of graphite oxidation from literature;[142] and (e, f) predicted gasification flux of CO and CO_2 versus oxidation temperature for PCEA samples with different sizes. (Compiled from refs.[139,142])

This chemical reactions-kinetics model has two adjustable parameters: the structural factor Ψ of the 2D RPM model, Eq. (7), and the initial ASA, ASA_o. The former was introduced as a material-specific parameter[39] but was not generally confirmed as such by other researchers. The latter depends not only on intrinsic graphite reactivity factors, but also on size and shape of specimens. This parameter was treated as freely adjustable by the authors in various simulations of experimental data from the literature, even for same-grade graphite samples with different shapes and sizes. The "loose" character of this adjustable parameter reduces the value of this model as a general predictive tool for graphite oxidation.

6.3.3 Gas Phase–based Approach

The early version of the chemical reactions-kinetic model developed by El-Genk and Tournier could not predict the weight loss profile and the penetration depth as a function of temperature. A substantial improvement was made by the same authors in a later version, which was then expanded to simulation of full-scale reactor components oxidation in an accidental air ingress scenario. In these conditions, the external gas phase, its composition, temperature, and flow pattern must also be considered. El-Genk and Tournier recognized that coupling CFD codes with their chemical reaction kinetics model would be computationally intensive. Therefore, they used a simplified approach in which results of the gasification model were compiled in readout tables or arrays, ready for coupling with the CFD code for reactor safety analysis. The readout tables listed molar fluxes of CO and CO_2 gases versus temperature, oxygen partial pressure in the bulk gas, and local graphite weight loss.[141] The model was implemented on a MATLAB/Simulink platform.

In this indirect way, the improved model could analyze transient gasification of NBG-18 graphite in a typical flow channel of HTGR fuel assembly. Five gas species (He, N_2, O_2, CO, and CO_2) were handled from both kinetic and thermodynamic angles by accounting for concentration variations and heat released in exothermic reactions producing CO and CO_2. When coupled with the CFD calculations, the model provided estimates for CO and CO_2 fluxes, local O_2 partial pressure in bulk gas, and local graphite weight loss as a function of graphite temperature, Reynolds number, and air temperature at the channel inlet. Moreover, a new correlation was proposed for the Sherwood number which is needed to calculate the oxygen diffusion velocity from the bulk gas phase, through the stagnant surface layer, to finally reach the graphite surface.[132] The correlation is valid for the laminar flow conditions prevalent in most laboratory-scale oxidation experiments. At the end of the simulation (when the weight loss reached 10 %), the weight loss was highest at the channel entrance and decreased rapidly with axial distance because of depletion of oxygen from the gas flow (Figure 50).[143] This conclusion agrees very well with early observations from experiments of graphite oxidation in channels with flowing air.[133,144,145] However, because the model focused mostly on the gas-phase conditions estimated from CFD calculations, it did not analyze O_2 diffusion in graphite pores, and therefore could not predict the development of nonuniform density profiles near the exposed surface by oxidation in a diffusion-controlled regime (Regime 2). Nonuniform density in oxidized graphite components is expected and could jeopardize the mechanical strength of graphite components.

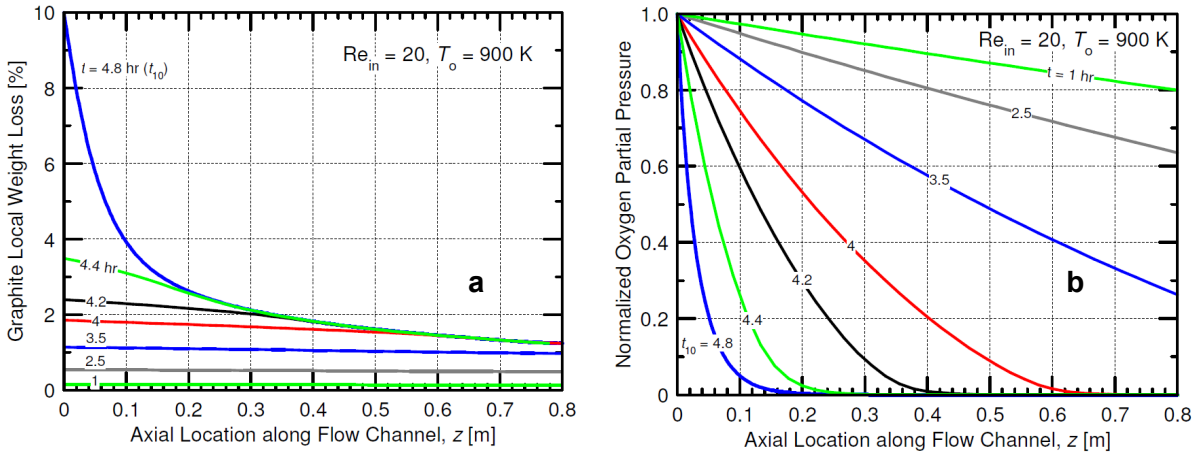

Figure 50. Model predictions for progress of NBG-18 transient gasification in a VTGR fuel channel. (a) Simulated variations of local graphite weight loss and (b) normalized O_2 partial pressure plotted against axial location positions in a 0.8 m long graphite flow channel. (More information available from ref.[143])

6.3.4 Balanced Approach

Another predictive model of graphite oxidation in Regime 2 was developed in collaboration by INL in the U.S. and Korea Advanced Institute of Science and Technology (KAIST) in Korea.[56,146] The model is based on similarities between resistors in a parallel electrical circuit and the graphite oxidation reaction channels. Thus, the overall oxidation rate in Regime 2 can be regarded as the result of parallel combination of oxidation rates in Regime 1 and Regime 3:

$$\frac{1}{Rate_{global}} = \frac{1}{Rate_1} + \frac{1}{Rate_3}. \tag{34}$$

The slowest of $Rate_1$ and $Rate_3$ will prevail in this equation. Moreover, oxidation in Regime 2 combines external surface reaction ($R_{surf} = -\rho \frac{d\,V}{d\,t}$) and internal pores reaction ($R_{bulk} = -\frac{d\,\rho}{d\,t} V$); both potentially modify the graphite specimen volume V and its density ρ. In Regime 1, a general Arrhenius type equation is used for the reaction rate controlled by chemical kinetics. In Regime 3, the rate of boundary layer transfer is estimated from the analogy between mass transfer and heat transfer. The explicit forms of $Rate_1$ from Eq. (2) and $Rate_3$ from Eq. (5) were used in Eq. (34) to evaluate the global oxidation rate, $Rate_{global}$.

The simulations were implemented in the computer code GAMMA. This code was specially designed for multicomponent analysis of HTGR ingress accidents from integrated analysis of thermo-fluid and chemical reactions related to air or water ingress in HTGRs.[147] In the collaborative work between INL and KAIST discussed here, graphite-specific parameters for Regimes 1 and 3 were obtained from oxidation rate data measured by the gasification method at near-zero weight loss combined with CO/CO_2 ratio measurements.[56,148] The function F_b in Eq. (2), which describes the transient rate change with weight loss, was modeled by Eq. (7) introduced by the 2D RPM pore development model.[39,40] In addition, the oxidation model used an ad-hoc introduced parameter, the internal surface density, to represent geometrical effects on oxidation rates.[51] However, its value (12,760 m^2/m^3 or 0.0073 m^2/g for IG-110) is less than 1% of the TSA (1.38 m^2/g) of IG-110 calculated by the BET method from N_2 adsorption at 77 K. This low value likely represents the RSA in the very early stages of oxidation at 600°C (from rates extrapolated to zero weight loss).[56] Modeling was performed assuming that only the internal porosity (and surface area) of graphite (but not its chemical or structural properties) vary with the increase in weight loss. The effect of pore structure evolution on the effective diffusivity was not considered, but the possibility that Knudsen diffusion may play a role in the effective diffusion coefficient was investigated. With some simplifications, the predicted weight loss variation was in very good agreement with the experimental results (Figure 51) at temperatures where oxidation would have transitioned from Regime 1 (600 °C) to Regime 2 (700–800 °C) and eventually to Regime 3 (900 °C). Figure 52 shows simulated results for variation of the density profile with time at various temperatures.[147]

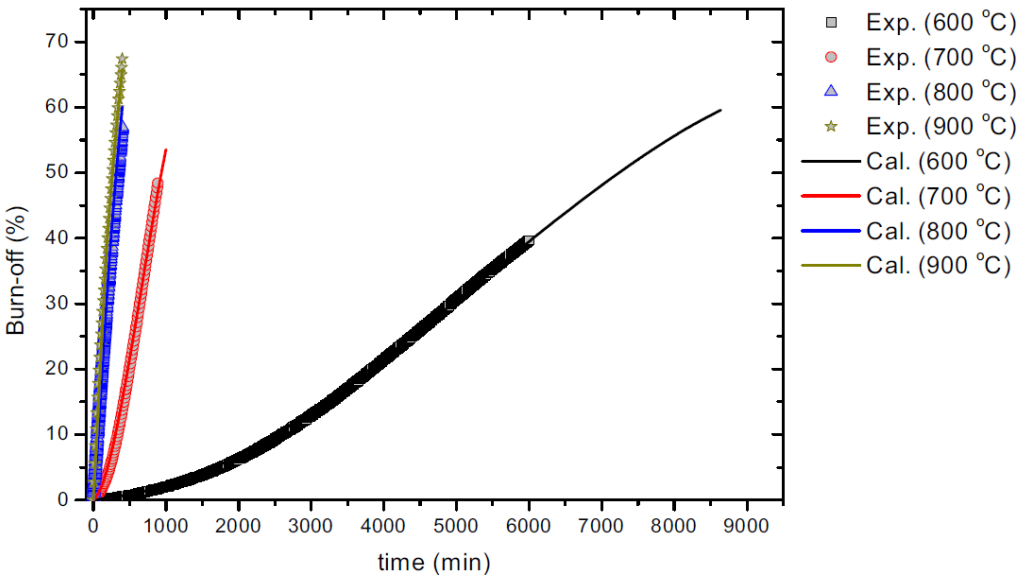

Figure 51. Comparison of IG-110 transient weight loss variation between experimental and calculated results. (More information available from ref.[147])

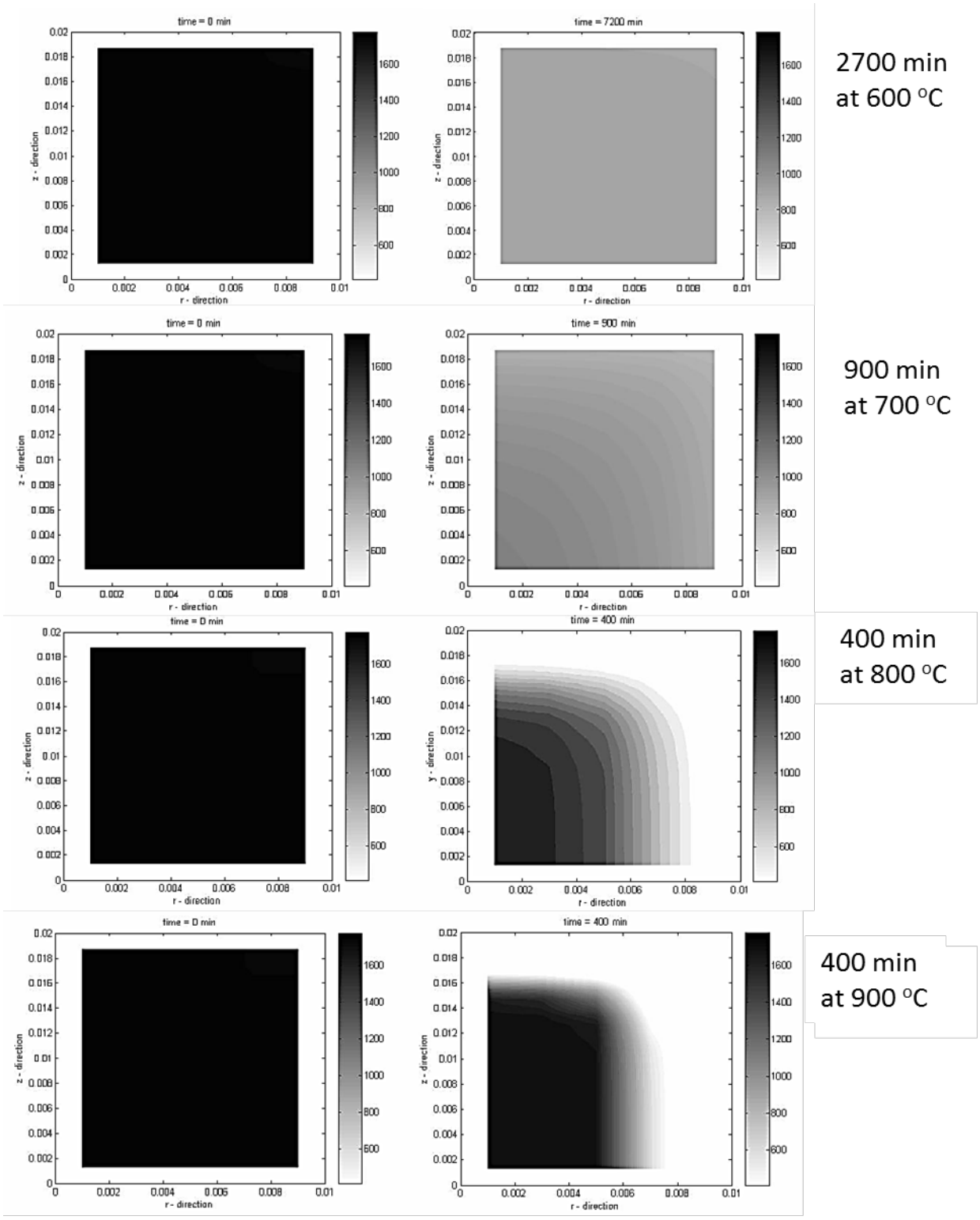

Figure 52. Simulated results for IG-110 density oxidized at different times and temperatures. (More information available from ref.[147])

6.3.5 Intrinsic Kinetics Approach

A new, completely different approach was proposed by Kane et al.[84,149] on the premise that all high-purity graphites have essentially the same chemical compositions and therefore, carbon reactions with oxygen should follow the same chemistry. At the crystallite level, this approach assumes that the reactive sites are C atoms at edges of graphite sheets (graphenes), for which there is only a limited number of structurally possible topologies. Also, the reaction between carbon and oxygen leads to either CO_2 or CO. Depending on the local configuration of edge carbon atoms, there are only a few energy profiles along the reaction paths. Moreover, the approach assumes that oxidation occurs only at the internal surface of open pores, where oxidants have direct access. Recognizing that the basic chemistry has limited variations, the difference between oxidation behavior of various graphite grades is assumed to be caused by the vastly diverse surface landscape of chemically reactive C sites. The density and configuration of sites are controlled by the microstructural properties of each graphite grade, among which the fraction of reactive edge sites in the accessible surface of internal pores is the most important and determines specific differences in graphite's intrinsic reactivity.

The oxygen transfer model (OTM) proposed by Kane et al.[84,149] uses the classical kinetic formalism. A sequence of elementary reactions for O_2 adsorption at edge sites and basal plane sites, followed by reaction with C atoms and desorption of CO_2 and/or CO, was assumed. The respective kinetic constants were introduced by Arrhenius expressions. Eventually, a complicated formal equation for the global oxidation process was obtained, which could be reduced to the following form:

$$-N_C = k''_{eff}(T, [O_2])[O_2]\,, \tag{35}$$

where N_c is the molar flux of carbon gasification and k''_{eff} is an effective reaction rate constant, in fact a composite constant that includes rate constants and O_2 dependence of elementary reaction steps assumed for the model. The rate expressed by Eq. (32) is normalized to the RSA, which is not actually a constant material property (it varies with temperature, time, and sample size). This normalization is a significant and important difference from the practical definitions of oxidation rates used in the other approaches. However, in this approach, kinetic terms are decoupled from grade-specific structural properties. With a simple scheme of elementary reactions, it is proposed that the unique kinetic equation (35) can be used for all graphite grades, whereas the grade-specific differences (modulated by microstructure properties) should be considered separately.

The OTM was tested on *powdered* NBG-18 samples, which were oxidized with variable oxygen partial pressures at various temperatures.[149] Powdered graphite was selected to eliminate diffusion perturbations as much as possible. The experiments showed that the effective kinetic constant k''_{eff} vary with temperature and oxygen partial pressure as shown in Figure 53a.[84] The plots indicate interesting variations of the overall activation energy with temperature (at constant P_{O2}) as shown in Figure 53b**.** A different mechanism was proposed for the effect of temperature: rather than transitions from different oxidation regimes (as usually encountered with massive graphite samples), the slope changes were attributed to changes in temperature-dependent prevailing reaction steps in the chain of the global process. This hypothesis, if independently verified, would allow oxidation rate predictions for any selection of environmental conditions (e.g., temperature, flow rate, oxidant concentration). The main challenge for practical purposes is the independent evaluation of RSA as a continuously variable fraction of ASA. Recent progress in this area was made by combining slow experiments (chronic oxidation conditions) with porosity characterization using X-ray computerized tomography (XCT).[104]

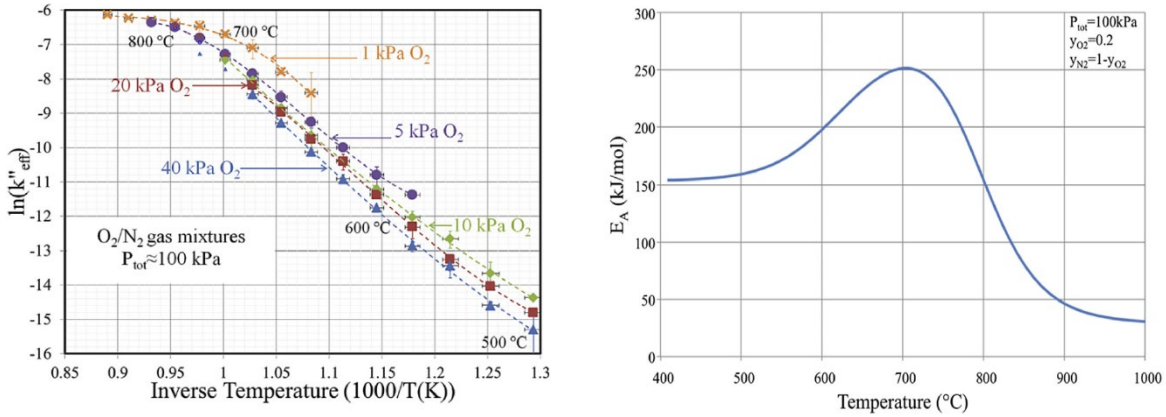

Figure 53. Effects of temperature and O_2 concentration on effective reactivity and activation energy during oxidation of NBG-18 powder. (a) Experimental results for effective activity constant versus temperature and O_2 concentration; and (b) effective activation energy variation with temperature at constant O_2 concentration. (More information available from refs.[84,149])

6.3.6 Microstructure-based Approach

The 3D random pore model (3D RPM) developed by Paul was introduced briefly in subsection 4.2.2.2.[46,47,48,49] It is a microstructure-based model that describes graphite oxidation in the kinetic regime (Regime 1). The pore structure is described by randomly placed spherical voids, some of which are open to oxidant access and others being closed at the initial moment. It is assumed that oxidation occurs only at the surface of open pores, in a region extending to certain depth under the exposed surface. In this region, open pores grow in size at an intrinsic reaction rate, which depends on temperature, and eventually, they connect with (i.e., discover) nearby closed pores.[46] In this way, initially closed pores become open and continue to grow with the same intrinsic reaction rate. At any given time, the total pore volume is shared between a surface region of open pores, an intermediate region of open and newly discovered pores, and a bulk region of closed (not yet discovered) pores. Thus, depending on sample size, the model predicts the development of a nonuniform density (or porosity) profile under the surface, as has been observed experimentally in the kinetic regime, usually defined by persistence of linear Arrhenius plots with the increase in temperature.

In summary, the 3D RPM model describes the transient oxidation rate in Regime 1 using two main variables: one (α) describes temperature-dependent intrinsic reactivity of graphite grades, and the other (β) describes the structure-related rate of closed pores being discovered and joined with expanding open pore neighbors. The model was validated on an extensive data base of transient oxidation data (weight time) for numerous graphite grades (not only nuclear) of various sizes and shapes.[46,49] Selected examples for the three grades of interest for this review are shown in Figure 54. In general, interpretation of multiple examples shows that transient weight losses in the onset oxidation stage occur quickly for graphites with fine pores, low bulk densities, small sample sizes, and high reactivity ratios. Aggregated values of reactivity ratio for 10 graphite grades versus the inverse of temperature (between 450 and 750 °C) showed an activation energy of 187 kJ/mol, which reasonably matches the range of grade-specific values (170–225 kJ/mol).

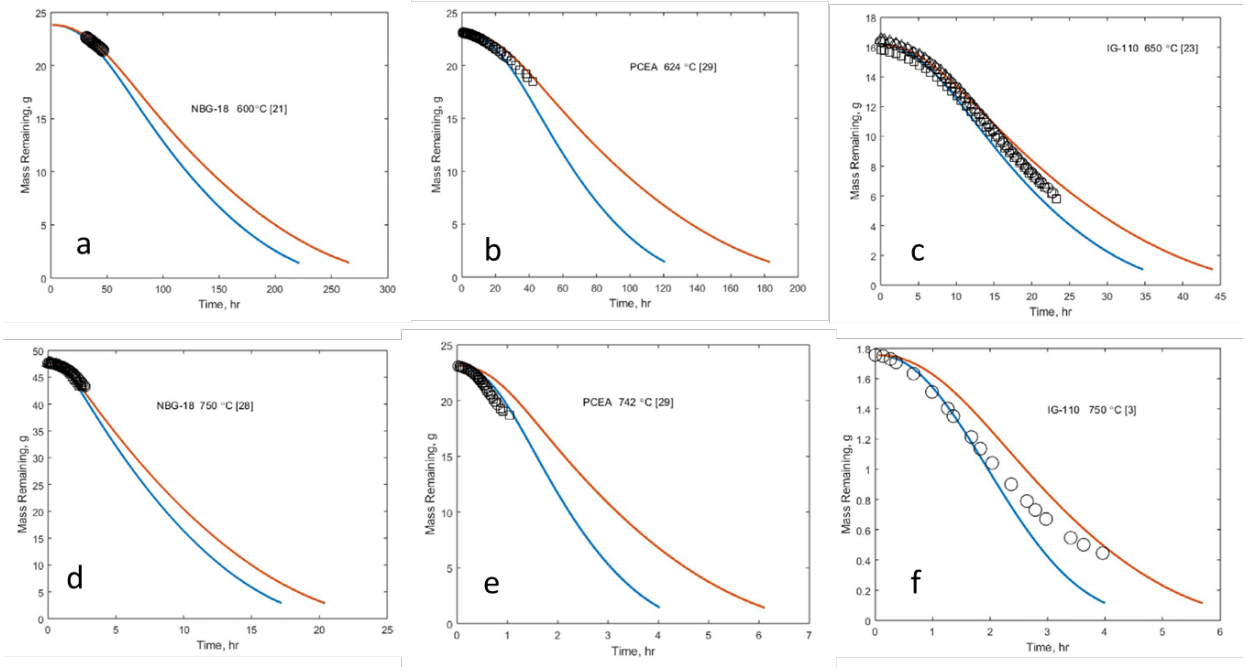

Figure 54. Selected examples of experimental and 3D RPM predictions of NBG-18, PCEA, and IG-110 oxidation behavior at different temperatures:[46] (a,b,c) low temperature (600–650°C); (d,e,f) high temperature (742–750°C); (a,d) NBG-18; (b,e) PCEA; and (c,f) IG-110. Data for various weight samples, reported by different authors, were fitted using the same parameters for each graphite grade. Ranges of minimum and maximum variation are shown. (Authors' data)

The main factor that differentiates oxidation behavior between graphite grades is the microstructure, characterized by the number, size, and position of open and closed pores, which also determines the initial graphite bulk density. In addition, two more experiment-related factors, sample size and shape, are quantitatively included in the model.

6.3.7 Probabilistic Approach

All the graphite oxidation models discussed thus far are based on the classical chemical kinetics formalism. The models assume that the chemical reactions (in the diffusion-free conditions of Regime 1) can be formally represented by multiple elementary processes in which surface C atoms (in typical topological configurations) react with the oxidant species according to a predictable reaction path. Little variability (if any) is assumed between possible reaction paths; their corresponding energy profiles are indistinguishable. From this deterministic perspective, gas–solid chemical reactions are regarded within the framework of classical chemistry textbooks and diffusion perturbations are completely neglected. Despite the ample evidence for significant variability of results in response to differences in the extrinsic or conjunctural experimental conditions, the hypothesis that the variability may also be found in the topologic and energetic heterogeneity of surface reactive sites is mostly neglected in the deterministic approach. The only acceptable way to explain scattering of experimental results is to regard Arrhenius parameters obtained by fitting classical rate equations as "effective," or condition-dependent. However, this explanation does not improve the understanding of the complex behavior of graphite oxidation that is revealed, for example, by repeated measurements with the most studied grade, IG-110 (see Section 4.3.2).

Probabilistic models may represent the next stage in the development of graphite oxidation models. The well-documented reality of energetic and structural non-homogeneity of graphite surfaces[138,140] and the variable topology of their C atoms[104,149] can be conveniently treated by using probabilistic models. The

diversity of reactive surface sites on graphite surface is one aspect to consider. Another aspect is the multiplicity and diversity of parallel and simultaneous elementary reaction steps on the chemical transformations path from reactants to products. Treating each of these "assumed true" elementary processes is not possible and may be even insignificant because arguments based on chemical kinetics are not sufficient for proving reaction mechanism. For example, Eq. (10), which is the classical reaction rate for oxidation of graphite by water according to the LH mechanism, can be derived formally from two different sequences of elementary processes (proposed by Gadsby[67] and Giberson[150]), and there is no way of determining which is the "true" mechanism based only on reaction rate evidence.

The probabilistic (or stochastic) approach starts from a simplified reaction scheme, which – even though it may differ from the true (but hard to separately analyze) chain of elementary steps – obeys general chemistry laws and satisfactorily describes the overall kinetic behavior. Recognizing that the topological diversity of surface C atoms must have energetical implications on binding energies and activation energies, Hurt and Calo[151] introduced the semi-global kinetic treatment of char combustion. The implication is that classical kinetic parameters, such as activation energy and pre-exponential term (frequency factor) in the Arrhenius equation are no longer represented as well-determined values (even with some associated standard error). Instead, in the probabilistic approach, they are expressed by probability distribution functions (Gaussian or another type) centered around a median value. Because gasification (oxidation) reactions occur through desorption of surface complexes, desorption energy (E_{des}) plays a significant role in the oxidation kinetics. In this case, the global gasification rate can be expressed as

$$Rate_{global} = \int f(E_{des})\ Rate_{local}\ (E_{des})\ \mathrm{d}E_{des}\ , \tag{36}$$

where $Rate_{local}(E_{des})$ is the local gasification rate, which can be approximated, for example, by the LH model. The distribution function $f(E_{des})$ can conveniently be modeled by a Gaussian distribution characterized by its center E_{deso} and standard deviation $\sigma_{\text{E-des}}$. With these assumptions, the pressure dependence of the reaction rate depends on the breadth of the Gaussian distribution: the case of homogeneous surface ($\sigma_{\text{E-des}} = 0$) leads to the basic LH model, where the rates stabilize at some value with the increase in oxidant pressure, whereas for nonuniform surfaces (energetically and structurally), larger widths of Gaussian distribution function result in continuous dependence of the oxidation rates on the oxidant pressure.[152] (Figure 55a) Moreover, there is indirect evidence of cooperative effects between reactive surface sites for oxidation by small moisture concentration in helium, as shown in Figure 55b by the inconsistent response of isothermal oxidation rates to changes of P_{H2O}. Uncorrelated variations produced the expected rate acceleration with P_{H2O} (although scattered), whereas continuous P_{H2O} decrease produced opposite results. This sort of surface site "memory effects" is not expected, nor is it accounted for by deterministic models.[65]

A semi-global approach was used by El-Genk for simulation of literature experimental results on acute oxidation in air of various graphite grades,[43,138,139,140] and by Contescu [33,71,72,65] for modeling of chronic oxidation by low moisture concentration of several graphite grades. The stochastic representation of global processes relies heavily on numerical methods for multiparameter fitting of simultaneous multivariable equations. For example, although this approach may reduce estimation errors of individual parameters, the numerical results may not always have a clear physical meaning. For example, Figure 55c illustrates experimental data for oxidation rates by moisture of four different graphite grades over a broad range of P_{H2O} and temperatures and their best fitting using LH, linearized LH, and BLH models.[33] Some best fitted solutions returned negative activation energies with disputed physical meaning, but examples of negative activation energy can be found even in the classical treatment of LH kinetics.[79] In other words, physical significance is partially sacrificed for the benefit of higher accuracy and better predicting performance. This method may be preferable by designers for practical use (e.g., safety analysis) but may not be highly regarded by researchers looking for a physical understanding of underlying mechanisms.

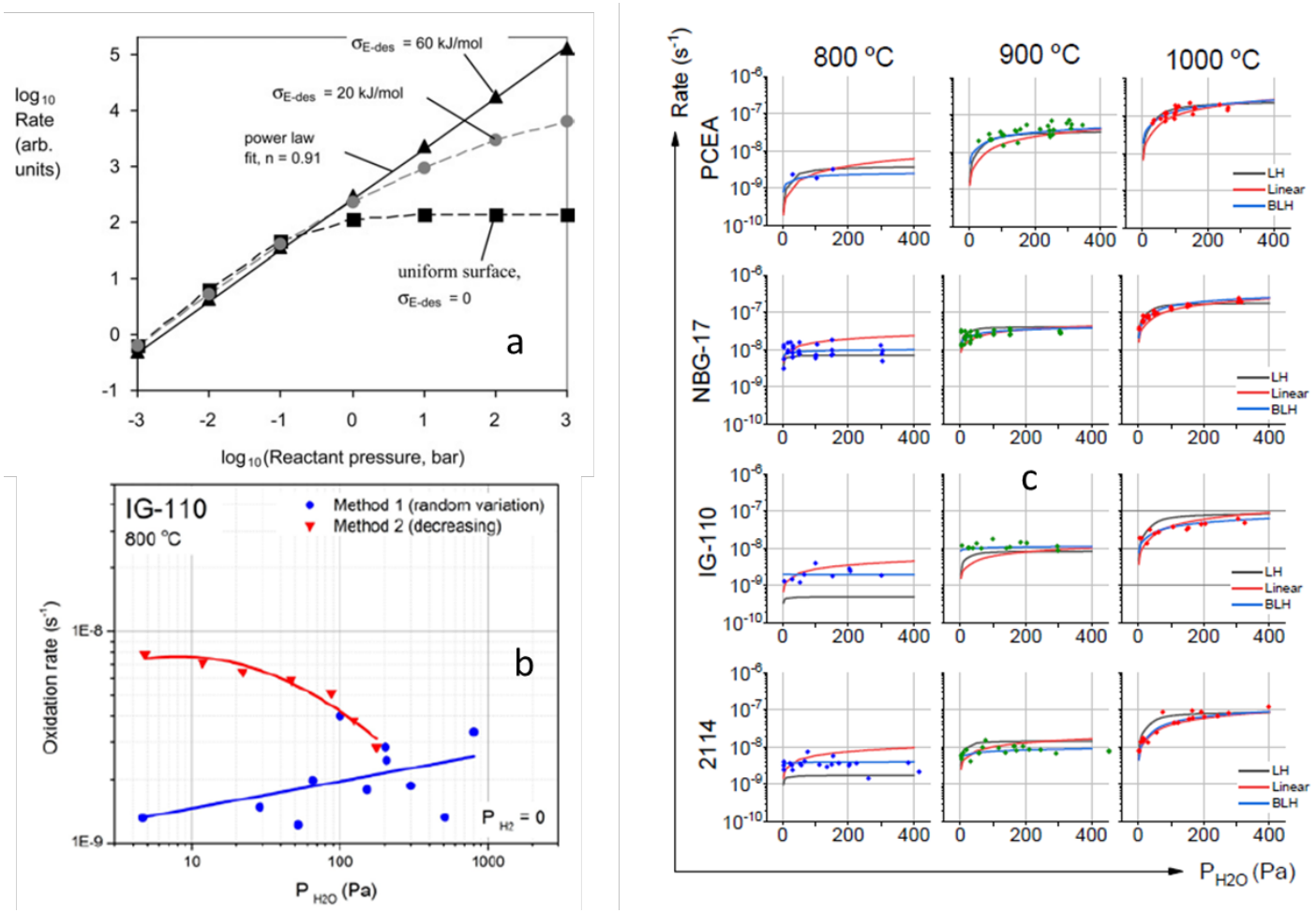

Figure 55. Probabilistic approach for oxidation models. (a) Isothermal variation of oxidation rates with oxidant pressure on surfaces with uniform and nonuniform distribution of desorption energies;[152] (b) isothermal oxidation rates by moisture measured for graphite IG-110 have different behavior when P_{H2O} is varied randomly or not, indicating the presence of cooperative effects between reaction sites;[65] and (c) comparison between measured oxidation rates by low water pressure in helium and predictions using LH, BLH, and linearized kinetic models. (Compilation of authors' data from ref.[33,65] and data from ref.[33])

6.3.8 Engineering Approach

Graphite oxidation is a highly complex process, and development of comprehensive, robust, and accurate models is challenging. Although the efforts toward a better understanding and representation of graphite oxidation behavior will continue, immediate needs for quick yet reliable assessment of the effects of various conditions may be of direct interest to designers. Until computer simulation codes have accurate models to predict oxidation behavior in terms of reaction rates, the use of global correlations supported by a broad range of experiments is a temporary pragmatic solution for predicting oxidation behavior.

Such correlations have been analyzed by Stempniewicz for both water ingress[153] and air ingress[63] into the primary HTR system. Stempniewicz selected available correlations from the literature, estimated their accuracy, and compared with experimental data, when found. For water ingress events, the researcher proposed an improved correlation that contains pressure-dependent and burn-off–dependent corrections of oxidation rates in the most conservative situations. The rate of the primary heterogeneous reaction ($C + H_2O \rightarrow H_2 + CO$) was expressed as

$$\frac{dm}{dt} = \frac{1.12\times10^4 \exp\left[-\frac{30788}{T}\right](P_{H2O})^{0.44}}{1+2.37\times10^{-7}\exp\left[\frac{14552}{T}\right](P_{H2})^{0.9}(P_{H2O})^{-0.4}} M(P,B)\ , \tag{37}$$

where *M(P,B)* is the function containing pressure and burn-off correction factors.[153]

For oxidation by air, Zheng and Stempniewicz[63] compared three experimental correlations from literature with experimental data measured from the 2008 NACOK experiment at the Julich Research Center in Germany. NACOK is the experimental facility built for real-time simulation of air ingress events on graphite components. The three literature correlations selected for comparison with the experiment are as follows:

- The NKL correlation for graphite IG-110:[154]

$$\text{Rate (kg m}^{-2}\ s^{-1}) = 7500 \exp\left(-\frac{26218}{T}\right) P_{O2}^{0.75} \tag{38}$$

- The CEA correlation for graphite PCEA:[155]

$$\text{Rate (kg m}^{-2}\ s^{-1}) = 25.6 \exp\left(-\frac{19240}{T}\right) P_{O2}^{0.5} \tag{39}$$

- The CEA correlation and for graphite NBG-17:[155]

$$\text{Rate (kg m}^{-2}\ s^{-1}) = \exp\left(-\frac{18040}{T}\right) P_{O2}^{0.5} \tag{40}$$

- The Roes correlation, which includes air flow rate, *v*, as a parameter:[156]

$$\text{Rate (kg m}^{-2}\ s^{-1}) = \left(\frac{P_{O2}}{10^5}\right)\left[\left(7500\ exp\left(-\frac{16140}{T}\right)\right)^{-1} + (0.0008v^{0.65}T^{0.34})^{-1}\right]^{-1} \tag{41}$$

Figure 56a shows the variation of oxidation rates versus absolute temperature according to these correlations. They are compared with the graphite oxidation rates measured in the NACOK experiment and processed by the TINTE code. The correlation by Roes[156] was found to better fit the experimental data if the air flow velocity was adjusted to match the experimental conditions (1 m/s). Next, the air flow and

temperature in the NACOK experiment were calculated as a function of time and position using TINTE and SPECTRA codes. The results were verified with the oxidation rates predicted by the Roes correlation. As shown in Figure 56b, predicted graphite corrosion distribution very accurately reproduced the qualitative observation that corrosion was more intense at the bottom, as well as the quantitative estimate of total mass loss after 9 h (8.9% versus 8.4% measured).[63]

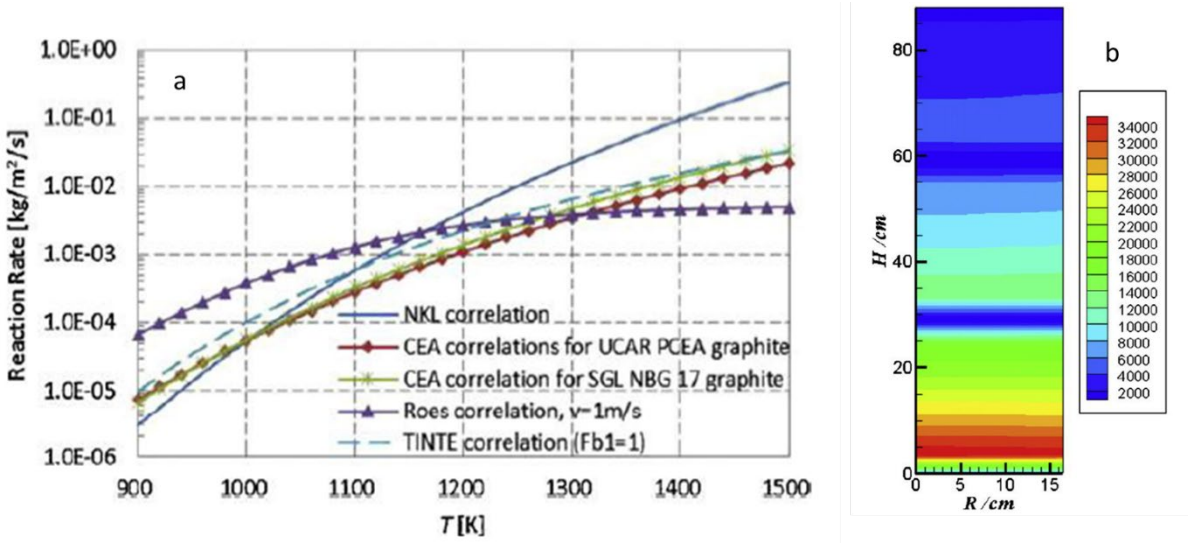

Figure 56. Graphite oxidation correlations and experimental results after 9 h graphite corrosion in the NACOK experiment. (More information available from ref.[63])

The NACOK experiment summarized here demonstrated that computer codes and engineering correlations (cross-validated between several sets of experimental reports) can successfully simulate large-scale experiments representing HTGR air ingress events.

6.3.9 Multiphysics Approach

Development of multiphysics computer codes enables numerical study of complex problems that involve multiple coupled physical processes that cannot be covered by a single traditional discipline. Wang et al.[60,Error! Bookmark not defined.] recognized that oxidation models alone cannot fully represent graphite behavior d uring either normal operation or accident conditions because other important fields for the process are not involved. Thus, the authors pioneered a multiphysics simulation of MHTGR graphite oxidation by water. Using COMSOL Multiphysics, they investigated moisture – graphite reactions by combining the free fluid flow, porous medium flow, heat and mass transfer, chemical reactions, and graphite structural changes. The gas flow of free fluid was modeled by a Reynolds-averaged Naiver–Stokes equation, and the transport in graphite pores was simulated by the Darcy law. The diffusivity of each component was calculated by considering graphite tortuosity, gas mixture diffusivity, and Knudsen diffusivity. The LH reaction rate[32] was calculated with graphite-specific parameters determined from accelerated oxidation tests at ORNL.[33] The rate acceleration factor in the onset transient stage was modeled according to the 2D RPM model[39] with graphite-specific values for the structural factor Ψ. Heat transfer was simulated for both convection and conduction. Considering the very low reaction rates, the reaction heat was not included in calculation, but the fission power was considered.

The helium coolant was assumed to carry 1.2 Pa H_2O and 10 Pa H_2 at 6.4 MPa total pressure and temperatures between 800 and 1400 K (527–1127°C).[60,78] The LH kinetic parameters were preferred over the BLH parameters.[33] It was found that the order of increasing oxidation damage at the graphite surface was IG-110 < NBG-17 < PCEA < 2114. Depending on the temperature gradients along the 8 m high fuel

blocks in the reactor's core, oxidation occurred unevenly along the distance from the gas inlet (Figure 57). Density reduction was greater at the reactor bottom, where temperatures are higher, but oxidation was limited to a thin surface layer, not exceeding 1.5 mm. The local mass loss in this thin layer may have large variations, from 81% for PCEA and 8% for IG-110 at 0.01 mm just below the surface to 0.5% for PCEA and 0.8% for IG-110 at 2 mm from the surface. The difference between grades is related to graphite-specific kinetic constants and in-pore transport properties.[76] Most graphite materials will remain unoxidized, so chronic oxidation by moisture will not reduce the mechanical strength of graphite components, provided that the coolant chemical composition is rigorously monitored and maintained within the design parameters. The results should be considered conservative because closure of graphite caused by neutron irradiation was not considered.

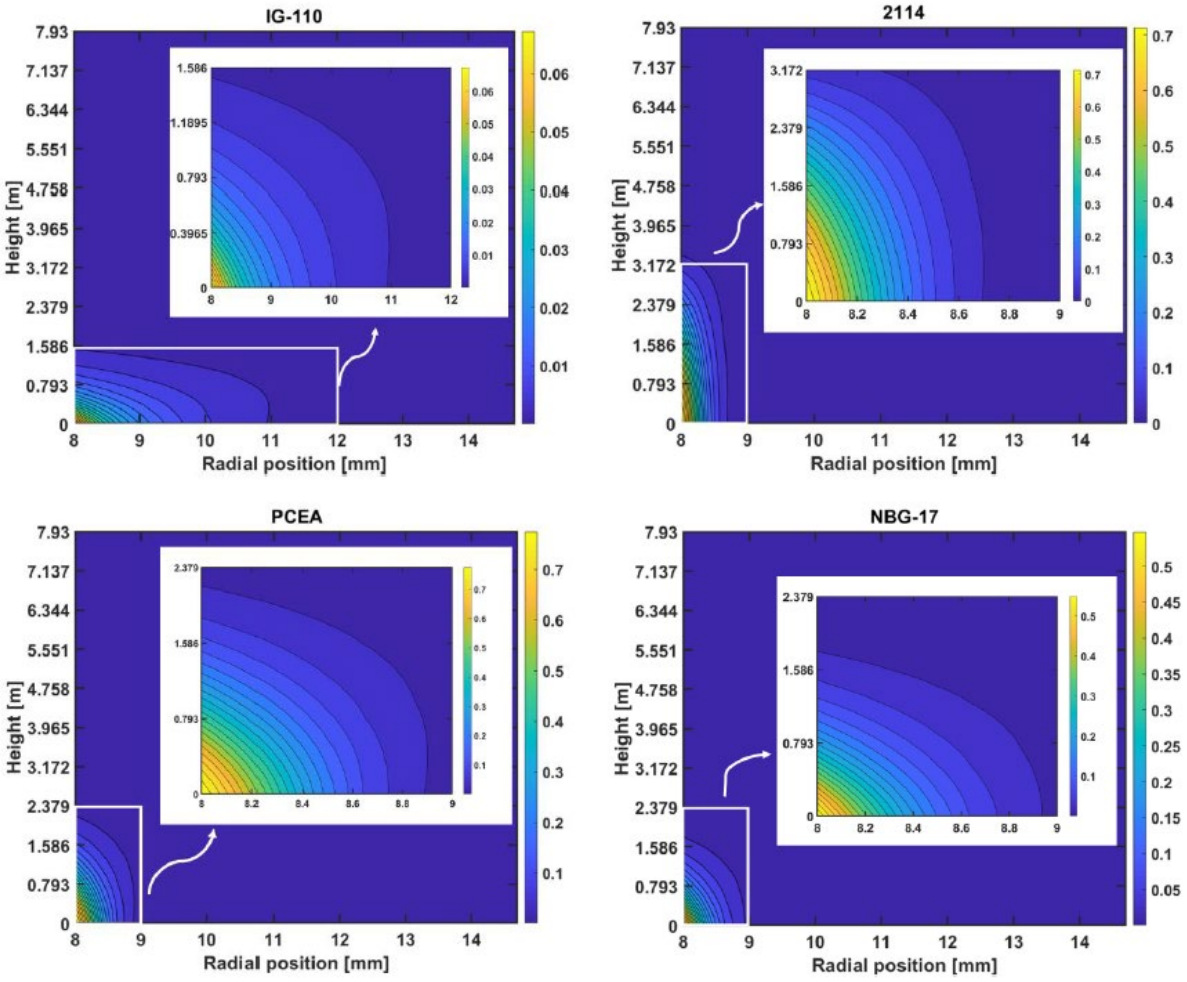

Figure 57. Multiphysics simulation results for oxidized graphites' weight loss distribution along the height of coolant channels after 36 months of normal operation. Height zero stands for the bottom of the active core. (More information available from refs.[60,78])

7. KNOWLEDGE GAPS AND FURTHER RESEARCH NEEDS

7.1 EXPERIMENTAL DATA

The mechanism of chemical reactions between C materials and gaseous oxidants (O_2, H_2O, CO_2) has been debated for decades, stimulated not only by academic interests but also by the need to gain control on processes in which carbon oxidation is either the main process (coal gasification) or an undesirable side effect (oxidation of graphite electrodes in metallurgy, C–C composites for civil and military purposes, and in-core components of nuclear reactors). Although some general understanding of the mechanisms at atomic and crystal scales have been reached, the debate is not closed yet.

Validation of kinetic models and implementation for specific cases of graphite oxidation events require two types of experimental data input:

- Oxidation rates at various conditions (temperature, oxidant concentration, weight loss level) and derived values of kinetic parameters (activation energies, pre-exponential factors, reaction order) in the formal kinetic equation(s) describing the chemical processes

- Rates of transport processes determined by concentration gradients (diffusivity) or pressure differences (permeability) for viscous transport, or by molecular properties and pore diameters for Knudsen diffusion

Complications arise from the fact that oxidation causes continuous structural changes, such as dilation of existing open pores, discovery and connecting with previously closed pores, and collapse of pore separation walls. The expansion and reconfiguration of the initial pore system with the progress of oxidation is difficult to dynamically predict or characterize. For practical reasons related to nuclear graphite's structural function, oxidation modeling may not be needed beyond approximately 10 % weight loss. As discussed previously, oxidation rates vary with the progress of weight loss: they increase nonlinearly up to about 5 % weight loss (the transient oxidation regime in the onset period [93]) and then reach a quasi-stable plateau between approximately 5 % and 30–35 % weight loss (the quasi-steady oxidation regime).[42] Measurements according to ASTM D7542 between 5 and 10% weight loss provide not only the oxidation rates in the quasi-steady oxidation regime, but also information on transient oxidation rates in the onset regime. Unfortunately, this additional information, which is already available from experiments, was only scarcely analyzed for modeling purposes.[39,40,46,47,48] Scrutinizing these data might help improve the understanding of shape and size effects, which are often neglected.

In addition, the effect of structural changes on transport parameters (oxidant effective diffusivity) is difficult to measure directly. It is generally accepted that the diffusivity of gas molecules in a porous body is significantly reduced compared with the free gas diffusivity, but widespread agreement on how to quantitively relate the diffusivity reduction factor β to pore system characteristics is still absent. Before more research data become available, empirical correlations continue to be used for the relationship between diffusivity parameters and local porosity (or density) in the oxidized layer.

7.2 KNOWLEDGE GAPS

7.2.1 Insufficiently Understood Oxidation Rate Factors in the Kinetic Regime

The discussion on IG-110 acute oxidation by air in Section 4.3.2 provides credibility to rate measurements according to the ASTM D7542 [50] procedure. Researchers who followed that standard (perhaps with only minor variations) obtained quite well-concurring results in the temperature range of the chemically

controlled regime. Furthermore, the above discussion highlights the spreading of measured oxidation rates obtained in experiments that did not adhere to ASTM D7542.

Considering these findings, only those kinetic parameters determined according to the standard test method, namely the activation energy and the pre-exponential factor, can be regarded as reliable within the repeatability and reproducibility limits determined through the ASTM inter-laboratory study.[50] Unfortunately, other graphite grades have not been studied as much as IG-110, and the amount of information from parallel studies is limited. This is true for NBG-18 and even more for PCEA.

However, as discussed, oxidation rates are also influenced by the size and shape of graphite specimens. Most oxidation experiments were conducted using cylindrical graphite specimens (i.e., rods). In oxidation conditions in which the maximum penetration depth (δ) is smaller than the graphite rod's radius (R), a nonuniform weight loss (or density) profile with cylindrical symmetry develops under the surface, and a significant region of the core is not affected by oxidation. That is the case of support posts at the bottom of the reactor, for which the strength degradation upon oxidation in Regime 1 depends on the slenderness ratio and graphite's initial density.[125] However, if $\delta \geq R$, the specimen's core is completely penetrated by the oxidant. A weight loss gradient may still develop, but with slower density decay rates on radial directions. Because of overlapped oxidant transport from the diametral directions, overall oxidation rates of slender rods are faster than those of larger diameter rods. The thinner the cylindrical graphite specimens, the faster they may be consumed by oxidation, and the faster a quasi-uniform oxidation profile may develop.

The above-described situations are exemplified by the transient weight loss variations of PCEA specimens with different diameters (2.54 and 1.27 cm) in Figure 58. Among the four situations illustrated, the effect of temperature on identical size specimens is expected (Figure 58a), but the effect of diameter is not usually considered by oxidation models (Figure 58c,d). The aspect ratio has no effect on oxidation rates (Figure 58b) unless the diameter also changes (Figure 58c). The illustration in Figure 58e shows the development of weight loss profile in specimens of different diameters. The thinner the specimens, the faster the oxidation and more uniform the oxidation profile in Regime 1. For example,[98,99] rates for oxidation by air of very thin IG-110 plates (0.192 cm) become measurable starting from temperatures as low as 400°C (see plots in Figure 21). Experience shows that Arrhenius plots may still be linear with the increase in temperature for conditions in which large specimens may develop nonuniform oxidation profiles. Based on the linearity of Arrhenius plots, these situations are still typically considered in Regime 1.

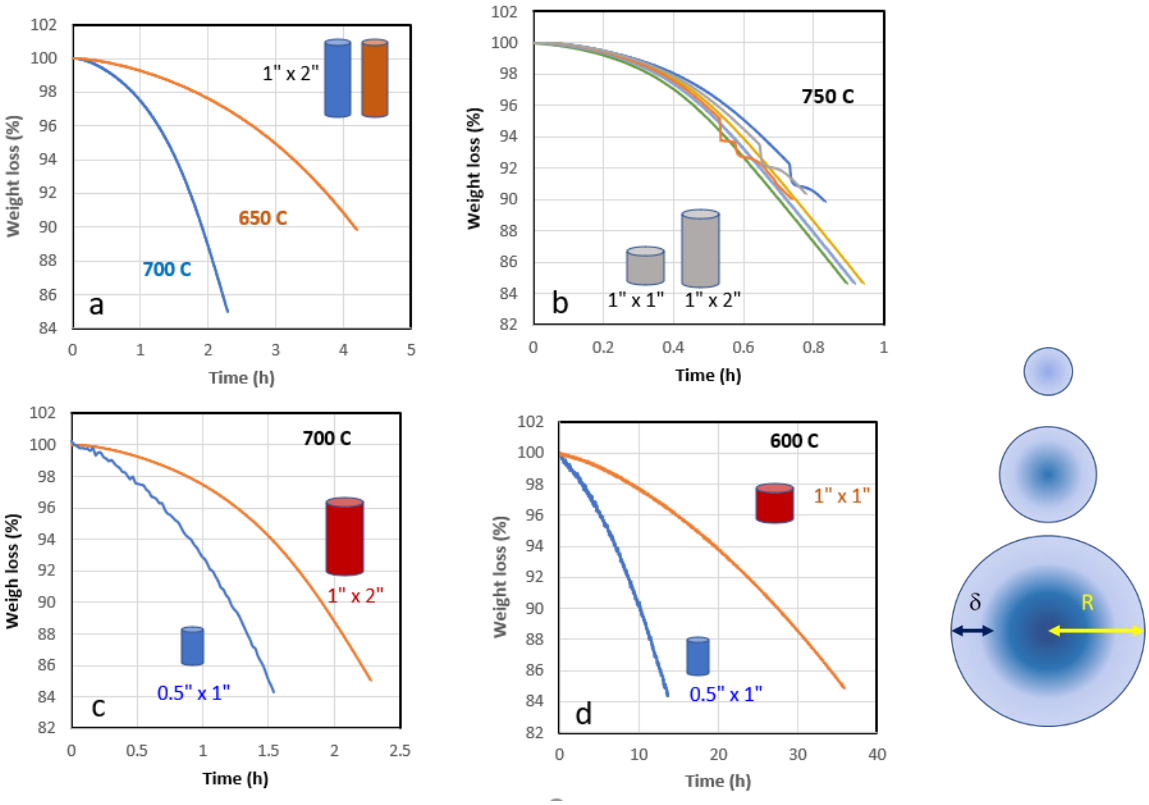

Figure 58. Temperature and size effects on PCEA graphite oxidation rates and density profiles. (a) Different temperatures, same size, same aspect ratio: oxidation rates increase with temperature; (b) different aspect ratios, same diameter, same temperature: no effect on oxidation rates; (c) different diameters, same aspect ratio, same temperature: the thinner specimen oxidizes faster; (d) different diameters, different aspect ratio, same temperature: thinner specimen oxidizes faster; (e) schematic representation of weight loss (density) profile development at identical oxidation conditions in cylindrical specimens of different diameters. (Authors' data compiled from refs.[38,57])

In practical situations, the degree of nonuniformity and density gradients in the oxidized layer are greatly influenced by specimen size. For small specimens used in laboratory-scale tests (about 1–2 cm diameter), oxidation in Regime 1 extends to approximately 700 °C. However, for full-sized components (such as moderator or reflector blocks), the chemically controlled Regime 1 ends at a lower temperature because of high diffusion resistance to the interior of the block.[41] In fact, nonuniform density profiles are *always expected* (and theoretically predicted) in processes involving reaction and transport.

The effect of specimen shape and size on oxidation behavior was only scarcely investigated by researchers, and to the best of the authors' knowledge, it is not yet included in a comprehensive kinetic model. Kim et al.[51] investigated the relationship between area-normalized oxidation rates in air (at 600 °C) and the exposed geometric surface of a series of IG-110 specimens with various shapes and size (and widely varying S/V ratios). They concluded that 1 m^3 of this graphite grade contains 12,760 m^2 of internal surface area, which was obtained from analysis of initial oxidation rates (near-zero weight loss). This corresponds to 0.0073 m^2/g, which is approximately 0.5% of the TSA calculated by the BET method (1.38 m^2/g) and approximately 0.7% of the non–basal plane area based on N_2 adsorption measurements (Table 2).[17] This low value may be correct for the RSA responsible for *initial* oxidation rates, but it is expected to increase with the progress of oxidation.[104] The absolute magnitude of RSA in the quasi-steady oxidation regime (between about 5 and 10% weight loss) is not known.

7.2.2 Insufficiently Understood Oxidation Rate Factors Outside the Kinetic Regime

The oxidation events of interest for reactor safety are unlikely to occur in the kinetic (i.e., chemically controlled) regime. On the contrary, air ingress accident models suggest such these events, which have extremely low occurrence probability, would be characterized by either high temperatures or oxidant-starving conditions, or both. For example, some models[137,157] predict that the decay heat will raise the fuel temperature close to about 1600 °C. However, most designs of typical modular HTGRs aim for a lower range of the peak fuel temperature, such as 1000–1100 °C [87] or even lower.[158] Oxidation will most likely be in Regime 3. However, CFD modeling, and flow experiments at INL indicated that the dominant air ingress mechanism in a loss-of-coolant accident (LOCA) will be a density gradient–driven stratified flow.[159] Under these conditions, the oxygen concentration in the reactor would be less than 21%. Rapid oxidant consumption for graphite oxidation at the more exposed reactor positions may cause oxidant-starving conditions at other locations. Several oxidation studies on IG-110 cited previously[56] attempted to reproduce such conditions, outside of the kinetic regime targeted by ASTM D7542. They produced results at variance with those of standard measurements, which highlights the deviant oxidation behavior outside the kinetic regime.

The logical approach for addressing these nonstandard situations would be to start from an oxidized model grounded on reliable data measured in standard conditions and to determine its response to the new conditions that mimic those of nonstandard experiments. For example, oxidation behavior at nonstandard conditions (lower O_2 concentrations than the 21 vol % of air or starving conditions due to reduced flow rates) could be simulated and compared with the existing pool of experimental data. Another challenge is accounting for odd shapes and sizes of graphite specimens. Fortunately, the vast experimental body of information on IG-110 oxidation by air at nonstandard conditions (outside of the kinetic regime) can be used to develop and finely tune more robust and reliable oxidation models.

7.2.3 Knowledge Gaps Regarding In-Pore Oxidant Transport Factors

Oxidant diffusion into the graphite pore structure occurs by a combination of viscous (or "normal") diffusion governed by Fick's laws and molecular diffusion governed by Knudsen's law. Normal diffusion is prevalent in porous materials with large pores, where resistance to diffusion comes from intermolecular collisions, as described by molecular gas theories. In narrow pores with diameters comparable with the mean free path of gas molecules, gas diffusion is controlled by molecules' collisions with the pore walls. This effect (i.e., Knudsen diffusion) is important at low gas pressures. Transition between viscous flow and Knudsen diffusion occurs gradually as the gas pressure decreases.

Viscous diffusion in free gas is characterized by the diffusivity coefficient (D_0), which has a power law variation with temperature ($D \sim T^q$, where $1.5 < q < 1.75$). In the graphite pore system, the effective gas diffusivity (D_{eff}) is a small fraction (β) of the free gas diffusivity, namely $\beta = D_{eff}/D_0$. In the absence of systematic studies, β may be represented as $\beta = \frac{\sigma\varphi}{\tau}$, where φ is the fraction of open porosity, τ is the tortuosity factor (the ratio between the geodesic path length of a pore and the Euclidean distance traveled across the porous material), and σ describes the constrictions of pore-connecting paths. When both viscous and Knudsen diffusions can coexist, the effective diffusivity coefficient can be written as follows:[160,134]

$$D_{eff} = \frac{\varepsilon}{\tau}\left(\frac{1}{D_0} + \frac{1}{D_{Kn}}\right)^{-1} . \quad (42)$$

Other authors used different approximations that do not agree with each other, such as $\beta = \tau$[161] or $\beta = \varphi\tau$.[162] If the latter is combined with an alternate definition of the tortuosity factor (such as $\tau = \varphi^{1/3}$),[163] one comes to the approximation $\beta = \varphi^{4/3}$. Unfortunately, clarity is still missing when it comes to estimating the effective diffusivity reduction factor β based solely on graphite structural parameters.

Direct measurement of D_{eff} is more effective. According to a recent review,[164] β values for O_2 diffusion from air in early nuclear graphite grades vary between 0.008 and 0.012, depending on graphite structure. For the newer grades with finer pores and lower porosity, the measured values of β for gas mixtures such as N_2/Ar are lower, but they still span one order of magnitude between fine-grained and medium-grained graphites.[164] The diffusivity values measured for H_2O vapors in helium for the same grades follow a similar trend.[73,76] Although not identical for N_2/Ar and H_2O/He systems, the structural factors β correlate well with the graphite density or porosity fraction of graphite grades investigated (Figure 47).[76] All data were measured at room temperature.

One complication is that all β values in Figure 59 characterize virgin (unoxidized) graphites. Oxidation dilates the pores and creates new pores, and thus reduces diffusional restrictions compared to the unoxidized material (β increases). Measurements of D_{eff} at various levels of oxidative weight loss were reported for PGA graphite (a historic grade).[165,166,167] Figure 60 illustrates several results. It was found that β had a nonlinear increase with the weight loss. The β values for the unoxidized graphite were roughly in the range of 0.0067 to 0.0123 for several virgin PGA specimens. After oxidation, β increased 3 or 4 times at 10 % weight loss. However, the relative increase of diffusivity (driven by concentration gradients) was greater than the relative increase of permeability (driven by total pressure differences). This difference suggests that pores have a bimodal distribution, with narrow pores being more numerous but having little contribution to the total pore volume. In this explanation, the larger pores are effectively used for oxidant transport and their walls are consumed by oxidation, whereas the narrower pore still restrict oxidant diffusion to the larger fraction of the internal pore area.[167]

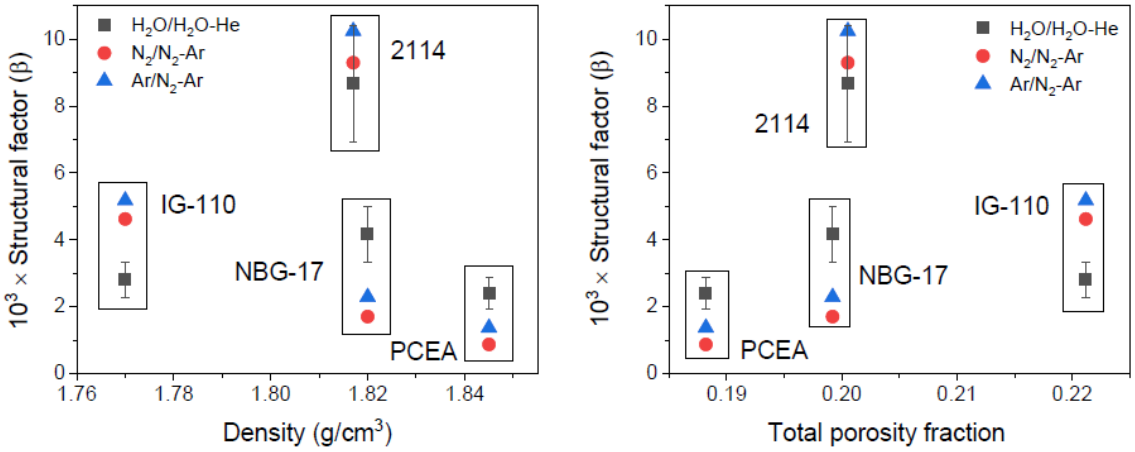

Figure 59. Diffusivity reduction factor β for graphites with various microstructures. Effective diffusivities in N_2–Ar[164] and H_2O–He[73,76] systems were measured at room temperature. (Compilation of authors' data and data from ref.[164])

A more comprehensive understanding of oxidation effects on pore structure parameters was obtained by transient elusion measurements. The results allow for comparing the behavior of thermally oxidized specimens (in air) against that of radiolytically oxidized specimens (in CO_2). All properties measured (diffusivity structural factor, tortuosity factor, pore area, and open pore volume) increased with the weight loss (Figure 61).[168]

Unfortunately, similar measurements on oxidized specimens of the newest graphite grades (possible candidates for HTGR components) could not be found in the open literature at the time of this writing.

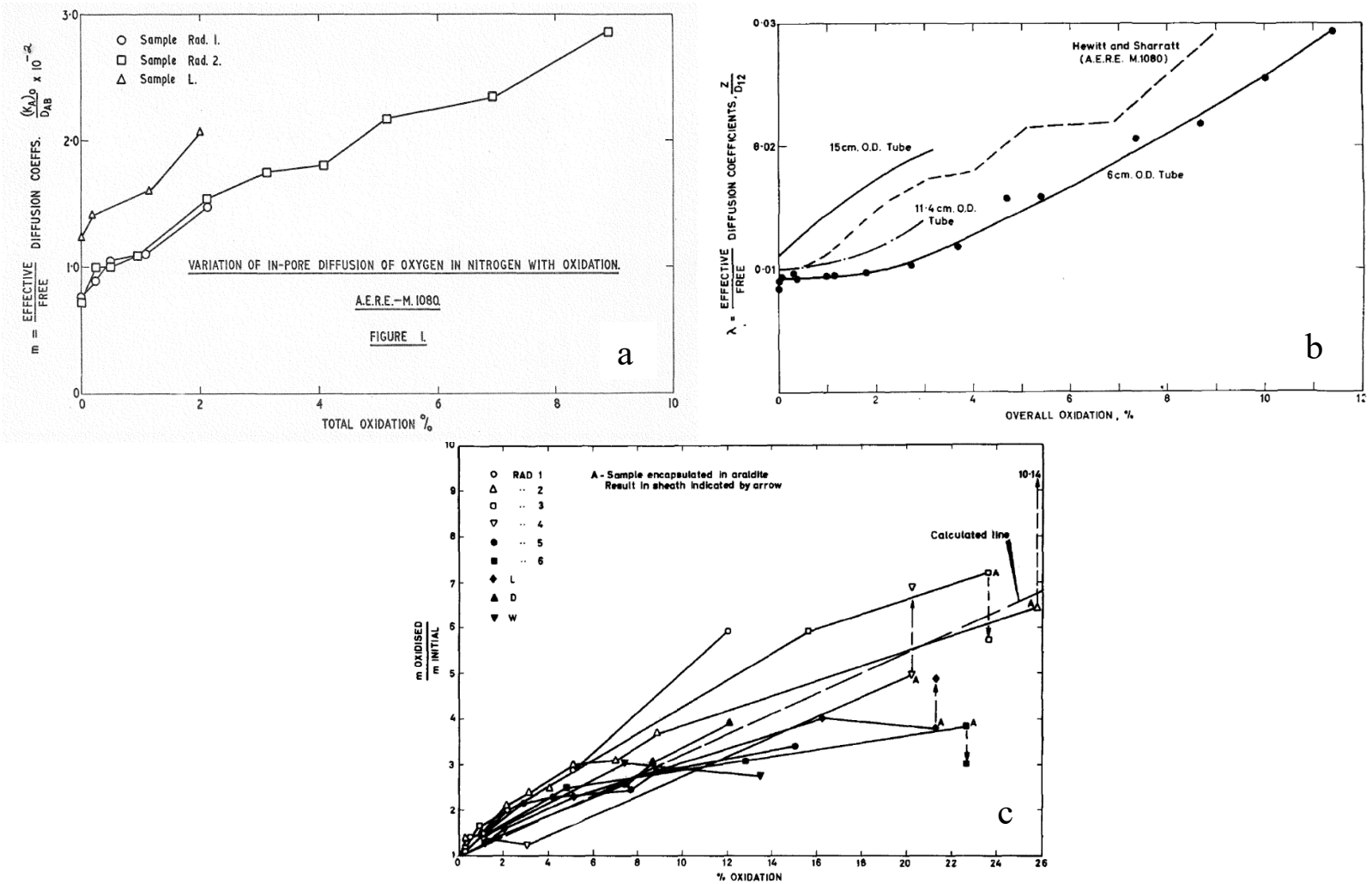

Figure 60. Effects of oxidative weight loss on the effective diffusivity reduction coefficient for O_2 from air in uniformly oxidized graphite PGA. The plots show $\beta = D_{eff}/D_0$ factors (effective diffusion coefficients in oxidized graphite normalized to free gas diffusion coefficients) in (a)[165] and (b)[166] and structural factors β for oxidized graphite (normalized to the β value of unoxidized material) in (c).[167] (Compilation of data from refs.[166,167])

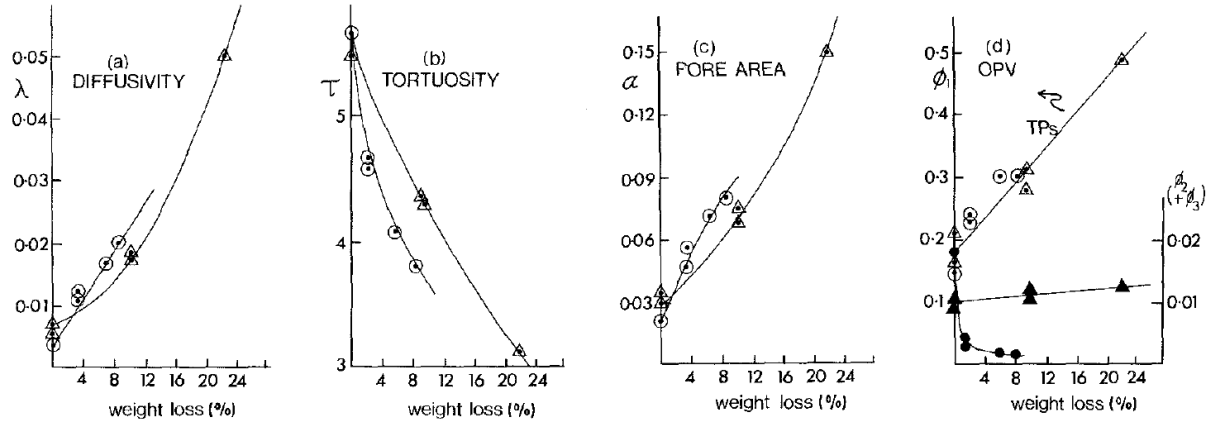

Figure 61. Effects of thermal and radiolytic oxidation on various main pore structure parameters of an unspecified extruded petroleum pitch coke. Circles: thermal oxidation; triangles: radiolytic oxidation. (More information available from ref.[168])

7.2.4 Knowledge Gaps Regarding Boundary Layer Transfer Factors

Graphite oxidation at high temperatures (Regime 3) is limited by the oxygen transfer rate from the gas phase to the exposed surface. The result is fast corrosion of exposed surfaces, dimensional and shape changes, and debris or dust generation. Chemical kinetics is not considered to affect the process because the rates are so high at those temperatures, and therefore, the effect of temperature (measured by the apparent activation energy) is almost null. Corrosion rate calculations are solely determined by mass transfer, which is the rate-limiting factor. The analogy between mass transfer and heat transfer is usually applicable.[169] However, in the case of carbon–oxygen reaction at high temperatures, chemistry cannot be ignored. With the increase in temperature, the main gas product becomes CO, which is thermodynamically favored over CO_2 at high temperatures. A secondary gas phase reaction between CO and O_2 in the boundary layer, near the graphite surface, may produce CO_2. Carbon dioxide is an oxidant for graphite, and its presence in the boundary layer may initiate another carbon oxidation path. The effect is a further acceleration of graphite corrosion, beyond the predictions of the mass transfer rules.[170]

Among the very few experimental studies of graphite oxidation in Regime 3, an experiment reported by Ogawa stands out for its significant conclusions regarding the boundary layer mass transfer with simultaneous chemical reactions.[169] Cylinders of graphite V483T, the German prototypical graphite for HTGRs, were oxidized at temperatures between 848 and 1120 °C in various flow conditions of an O_2-containing gas. The Reynolds numbers varied between 533 and 2490. The oxidation conditions covered Regime 3 (runs 1 and 3 at high temperatures) and Regime 2 (runs 2 and 4 at low temperatures). Ogawa found that chemical reactions did not affect the boundary layer mass transfer. Table 9 lists the experimental conditions and the results of these experiments. Notably, the radii of oxidized specimens varied by less than 1 mm after oxidation times of 2–5 h. The semilogarithmic Arrhenius plots of oxidation rates in Figure 62 clearly identify the change of slope at the transition between Regime 2 and Regime 3. The behavior of boundary-layer mass rates (BLMRs) in Regime 3 was calculated from mass transfer rules using the actual values of Reynolds, Schmidt, Nusselt, and Prandtl numbers (dashed lines in Figure 62). The trend of in-pore diffusion rates in Regime 2 was reproduced from a separate experiment with a matrix graphite.[169]

Table 9. Experimental conditions during oxidation of graphite V483T by air in Regime 3 and corresponding corrosion depth results from four runs.

		Run number			
		1	**2**	**3**	**4**
Reynolds number		533	904	1600	2490
Oxygen concentration (%)		5.38	4.62	4.82	4.39
Gas pressure at test section × 10^5 (Pa)		1.013	0.989	1.1019	1.023
Average gas temperature (°C)		1,100	875	1,030	823
Average cylinder temperature (°C)		1,120	910	1,070	848
Average wall temperature (°C)		1,100	893	1,040	822
Duration of corrosion experiment (h)		5.00	5.00	2.25	3.00
Corroded radial length Dr_{cor} (mm)	Disk 1	0.12	0.09	0.09	0.08
	Disk 2	0.12	0.06	0.06	0.21
	Disk 3	0.16	0.11	0.10	0.12
	Average	0.13	0.09	0.08	0.13

Data from ref.[169]

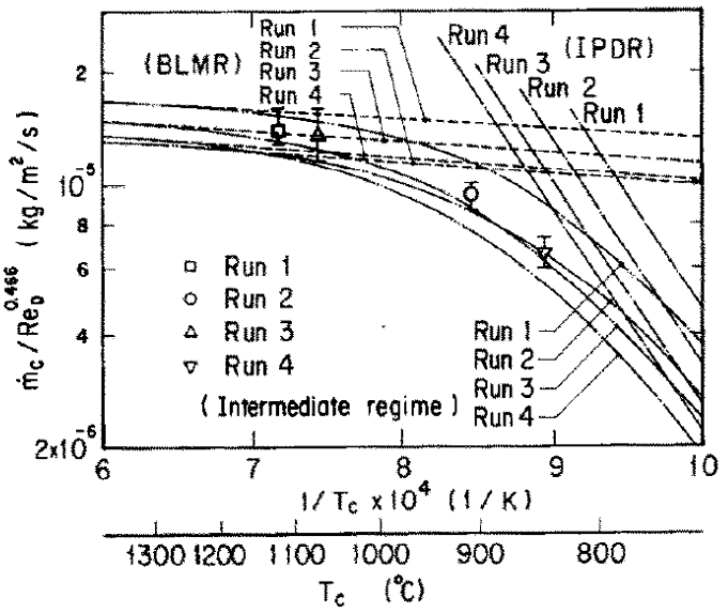

Figure 62. Arrhenius plots for oxidative corrosion rates of graphite V483T during high-temperature oxidation in Regime 3. (More information available from ref.[169])

Ogawa's experiments were further used for simulation of graphite oxidation in a flow channel during a severe air ingress accident.[171] The conditions leading to an explosive gas phase reaction between CO and excess O_2 were analyzed using a steady-state 1D model. The authors found that with minor dimensional modification of the coolant channel, the CO concentration can be reduced below the explosion limit, which demonstrates the feasibility of naturally safe HTGRs.

To summarize, current theoretical and experimental information on mass transfer processes through the stagnant boundary layer at high temperatures is scarce, and measurements are challenging. The common practice is to use the heat and mass transfer analogy. However, this approach does not account for the

obvious changes in the condition of graphite surface subject to rapid corrosion. Dust generation and surface roughening are predictable but not included in the models. Recent reports [88,89] of further acceleration of graphite consumption rates at even higher temperatures may indicate the onset of a new process at extreme temperatures, possibly oxidation of more resistant graphite grains after total consumption of the binder phase.

7.2.5 Knowledge Gaps Regarding Neutron Irradiation Effects

Information on neutron irradiation effects on graphite oxidation behavior is extremely scarce. Neutron irradiation produces structural defects by displacing C atoms from their stable crystal positions. This process leaves behind a vacant atomic position in the graphene layer and places the extracted carbon atom in an interstitial position between parallel graphite sheets. Depending on temperatures, these defects may become mobile and coalesce into larger vacancy and interstitial loops. Eventually, prolonged neutron irradiation results in fragmentation of graphite crystallites, which is expected to significantly augment the number of destabilized carbon atoms that may serve as oxidation active sites. Indeed, a first-principles study of the interactions between O_2 and defective structures typical for irradiated graphite indicated that O_2 adsorption is approximately 10 times stronger on sites neighboring one C atom vacancy than on a defect-free perfect graphite surface.[172]

Oxidation measurements of neutron-irradiated graphite have been very infrequently studied. A 1961 document from Hanford Atomic Products Operations[29] provided information on oxidation of reactor graphite between 450 and 675 °C in air and in oxygen. Incidentally, the procedure used was quite similar with that of ASTM D7542.[50] Up to 650 °C, oxidation rates were accelerated by a gamma flux of up to 10^6 Roentgen/h, but acceleration decreased with increasing temperature. At 600°C, the acceleration factor caused by gamma radiation was approximately 3. Oxidation rates of pre-oxidized graphite exceeded those of unoxidized graphite. However, neutron bombardment of 4×10^{19} nvt [§] (E > 0.18 MeV) or approximately 0.04 dpa at 550 °C did not have a significant influence on oxidation rates. Based on these data, the authors concluded that the effect of neutron irradiation at the operation temperature of HTGRs is expected to have little effect on the oxidation rates, but the influence of gamma radiation may be even greater at higher temperatures.[29]

A report from researchers in Russia[173] describes positive deviations of oxidation rates from the linear trend of the Arrhenius equation when irradiated graphite (grade RBMK among other Russian grades) was reacted with low concentrations of H_2O and CO_2 in helium. Such abnormal increases of oxidation rates were observed at low temperatures (in the kinetically controlled regime) on materials irradiated at fluences of approximately 5–18 dpa (i.e., before the turnaround point of dimensional changes). The effect was more intense on highly irradiated graphite and was observed at temperatures where oxidation of unirradiated graphite is usually very slow. Figure 63a shows examples of temperature dependence of oxidation rates for irradiated and unirradiated samples. In these experiments, the temperature was gradually lowered, and the oxidation rate was measured gravimetrically. Below a certain temperature, rather than continuing the decreasing trend, the rate of oxidation increased suddenly and reached values comparable to those recorded at very high temperatures. This unusual rate acceleration occurred between 800 and 840 °C in oxidation by water and between approximately 860 and 940 °C in oxidation by carbon dioxide. The changes were transitory because in approximately 2–3 h at constant temperature, the oxidation rates returned to the level expected from the Arrhenius trend (Figure 63b). A possible explanation is that the rate variation was caused by re-equilibration of the oxidation reactions between surface-controlled and in-pore–controlled regimes.[174] However, the fact that this effect was more intense for irradiated graphite (although it was also detected for

[§] The unit "nvt" is an archaic unit for neutron fluence equivalent to neutron/cm^2.

unirradiated samples) indicates that the structural changes caused by irradiation may have had a role in intensifying this effect.

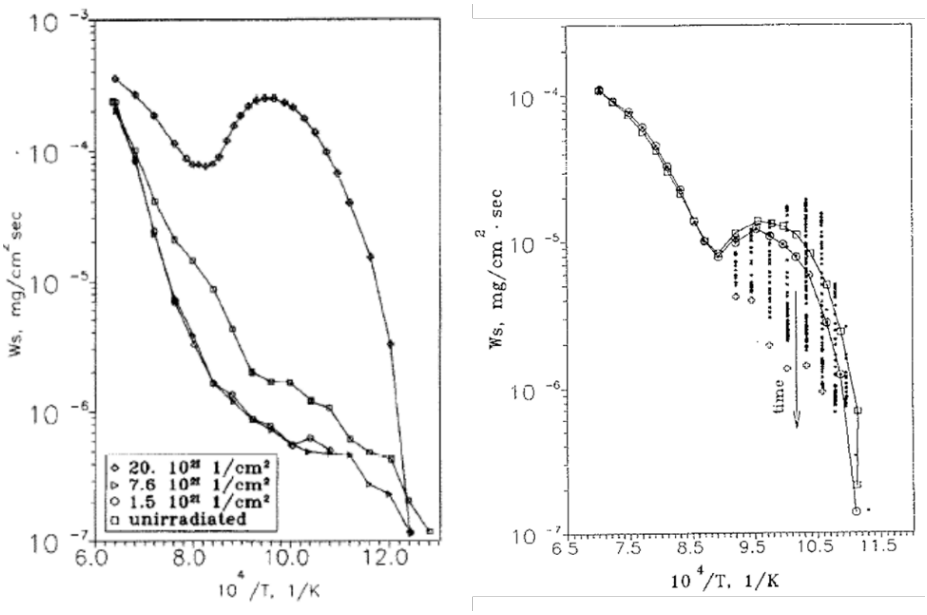

Figure 63. Arrhenius plots showing effects of neutron irradiation on oxidation rates. Left: Oxidation rate by CO_2 (2200 ppmv) of irradiated (500°C) and unirradiated graphite RBMK;[173] Right: Time-dependent relaxation of oxidation rates by H_2O (5000 ppmv) of irradiated GRP2 graphite (10.7 dpa at 550°C).[174] (Compilation of data from refs.[173,174])

A few more fragmentary reports examined the acceleration of graphite oxidation rates in the presence of neutron irradiation. For example, Schweitzer and Singer[175] found that the kinetic parameters of oxidation reaction, and in particular the frequency factors, may be different during in-pile neutron irradiation. In experiments with alternate irradiation and annealing of pile graphite, oxidation rates increased after the first irradiation, but subsequent cycles of annealing out-of-pile and re-irradiation produced oxidation rates and activation energy values that could not be distinguished from the unirradiated control stock (Figure 64). Evidently, the defects responsible for enhanced oxidation rates after the first irradiation were removed by annealing.[175] Considering that low temperature irradiation (< 200 °C) is expected to build up a large amount of Wigner energy (mainly as intimate Frenkel pair defects) it is not unsurprising that these defects were rapidly annealed out at temperatures above 300 °C.

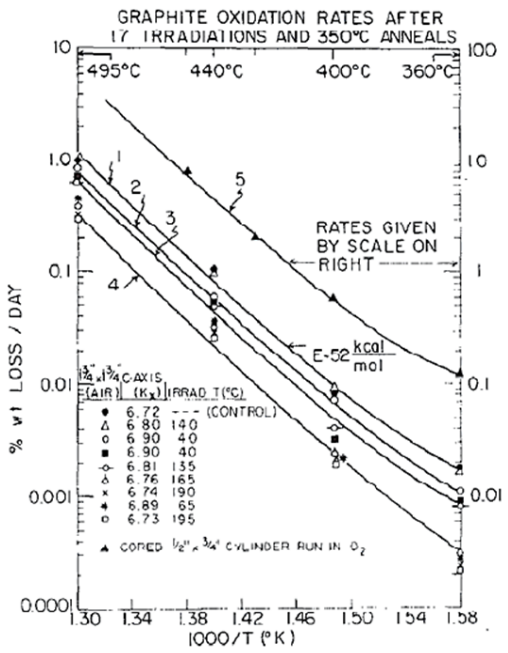

Figure 64. Arrhenius plots for oxidation in air of neutron-irradiated graphite AGOT. Data on four different samples were reproducible after 17 cycles of annealing and re-irradiation. Sample 5 was cored from a reactor block and oxidized in pure O_2. (More information available from ref.[175])

The acute lack of information on oxidation behavior of in-pile irradiated graphite is caused in part by the difficulty of performing oxidation rate measurements on small graphite specimens. Because of space constraints in the test reactor, the graphite specimens subjected to neutron irradiation have atypical sizes and shapes, which are significantly different from the recommendations of ASTM D7542. Although an ASTM standard is available with recommendations for reconciliation of testing requirements for small samples with requirements of existing standard test methods for large samples,[176] a standard specific to oxidation tests is not available. The small specimens are suitable for TGA measurements using commercial instruments. However, an unsolved problem is how to select TGA test conditions to obtain results compatible with the standardized ASTM test results. A recent study by Smith at INL[177] demonstrated that the oxidation rates measured by the continuous gravimetric methods in a VF (conforming to ASTM D7542) and in commercial TGA equipment agree with each other only for carefully selected TGA operation conditions. The most important requirement is avoiding oxidant-starving conditions by providing sufficient air flow rate for the rapidly oxidizing irradiated specimens. With some commercial TGAs, operating at high air flow rates may be challenging.

7.2.6 Insufficiently Understood Factors on the Effect of Oxidation on Graphite Properties

To properly understand the effects of oxidation on graphite properties with various levels of weight loss, one must compare uniformly oxidized specimens. This condition is essential for meaningful analysis of degradation of properties caused by oxidation. Most (if not all) graphite properties depend on graphite's density (or porosity), including mechanical strength and elastic moduli, thermal conductivity, heat capacity, and electrical resistivity. Although neutron irradiation and radiolytic oxidation penetrate the bulk of graphite components, thermal oxidation always advances from the exposed surface inward and generates nonuniform density and porosity profiles. To properly measure the change of graphite properties after oxidation, the perturbing effects of nonuniform profiles must be minimized or eliminated. This requirement was understood by researchers in Japan who characterized the effects of oxidation on the properties of early grades of nuclear graphites. Among those early grades (PGX, H-451, IG-11, and IG-110) developed as

candidates for HTGR components, IG-110 (and its early variant, IG-11) was the most extensively studied, and its degradation of properties caused by oxidation is well documented.[110,111,112,114,115,116,117,118]

The best way to produce uniformly oxidized specimens is to perform oxidation at low temperatures, where diffusion rates are much faster than gasification rates (in regime 1). Oxidation is more easily controlled by using CO_2 or water vapor as the oxidant, rather than performing traditional oxidation by air. Early studies of mechanical properties changes have shown that high-purity graphites (with no catalytic impurities such as iron, vanadium, molybdenum, and chromium) oxidized by 2 % CO_2/He mixtures at about 800–900 °C produce similar strength decay curves versus weight loss curves as specimens oxidized by 2 % H_2O/He at 900–1000 °C or by air at 500 °C.[115,116] Using small size specimens (about 1–2.5 cm characteristic length) and slow reaction rates provides another opportunity to produce uniformly oxidized samples for further properties measurements.

It is not entirely clear how to determine that oxidized specimens are uniformly oxidized. Theoretically, the radial density distribution in oxidized graphite specimens could never be uniform. However, practical acceptability limits should be defined for qualification of experimental specimens as uniformly oxidized for the purpose of characterizing properties. One possible acceptance criterion may use only weight and volume measurements before and after oxidation. Using m_1 and m_2 for a specimen's mass before and after oxidation, respectively, and v_1 and v_2 for their respective volume, the relative variations of mass, volume, and density are $\Delta m = (m_1 - m_2)/m_1$; $\Delta v = (v_1 - v_2)/v_1$; and $\Delta \rho = (\rho_1 - \rho_2)/\rho_1$. If $\Delta m \cong \Delta \rho$ and $\Delta v \cong 0$ the specimens can be considered uniformly oxidized for the purpose of measuring properties.

However, one more complication is that, as Figure 65 shows, the requirements for machining graphite specimens for standardized measurements of various mechanical [178,179,180,181,182,183] and thermal [184, 185] properties are far from being uniform. Specific types of measurements require specific shapes and sizes of specimens. These requirements work very well for characterizing properties of unoxidized graphites but complicate selection of oxidation conditions that would consistently produce uniformly oxidized specimens of comparable weight loss but with different sizes and shapes.

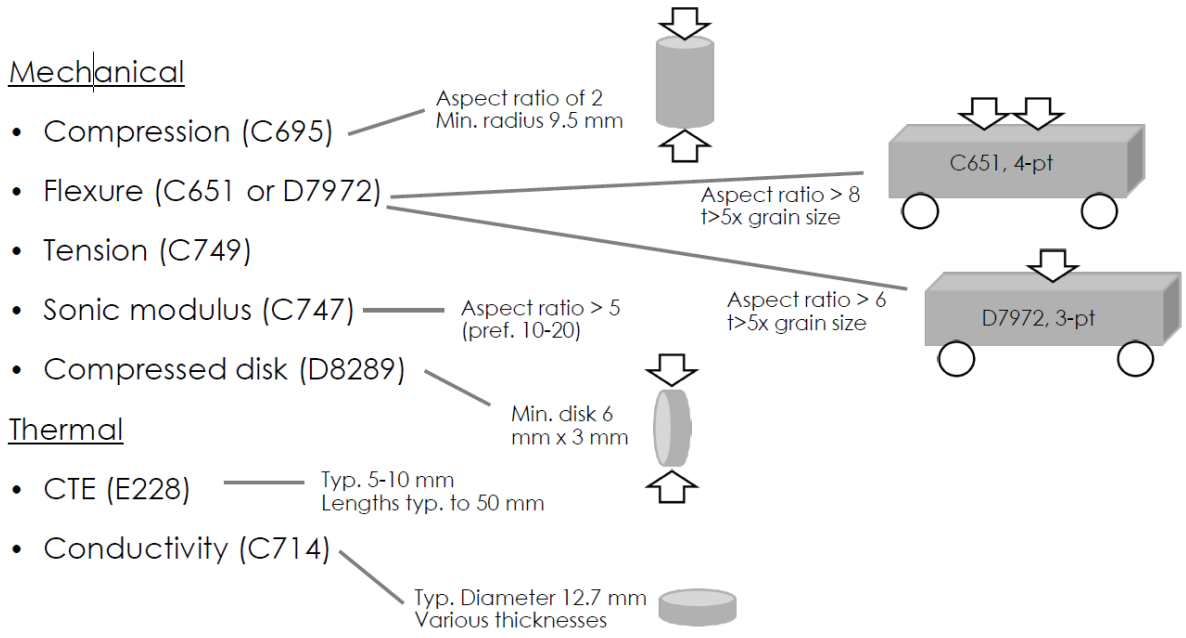

Figure 65. Diversity of graphite specimens' shapes and sizes recommended by current ASTM standards for mechanical and thermal properties characterization. (Authors' schematic)

This discussion points to the need for dedicated ASTM direction regarding preparation and characterization of uniformly oxidized graphite specimens appropriate for further measurement of specific mechanical and thermal properties. For example, ASTM subcommittee D02-F could take steps for elaboration of a standardized guidance, or perhaps a best practices document for producing, characterizing, and measuring the properties of uniformly oxidized graphite specimens. The document should also inform on the need to apply additional machining of oxidized specimens before proceeding to mechanical testing by the existing standards. For example, it was empirically found that trimming the soft oxidized ends of cylindrical samples prepared for compressive strength measurements increases the reproducibility of test results[108,124] compared with the tests on untrimmed specimens.[125] Evidently, if oxidation produced a nonuniform density profile in specimens, the soft oxidized ends would fail first and would indicate weaker fracture strength results. It is not clear whether trimming the ends would still be needed for uniformly oxidized specimens.

7.2.7 Overview

Finally, as much as the understanding of graphite oxidation behavior has evolved and grade-related differences between various graphite types have become visible, one should never miss the big picture. Specifically, one cannot disregard the common characteristics in all graphite oxidation processes:

- The limits of the three basic oxidation regimes are not rigorously fixed, but rather, they vary depending on circumstances such as temperature, oxidant supply rate, and component size.

- Oxidation rates increase exponentially with temperature (Regime 1), then slow (Regime 2), and eventually become independent of temperature (Regime 3) before increasing again at extreme temperatures.

- Oxidation is local and must be treated as such.

    - Large components will be less affected by oxidation than small, laboratory-scale specimens.

    - In the near-surface zone affected by oxidation, weight loss is a local property that varies with the distance from the surface.

- The density profile under the surface of oxidized graphite becomes steeper (i.e., narrower) with an increase in temperature.

- Local degradation of properties (e.g., mechanical, thermal) correlate with the density profile.

Although current graphite oxidation models may not be able to fully reproduce graphite oxidation behavior in every detail related to graphite structures and/or conjunctural differences, these general trends will hold true and should not be overlooked.

8. CONCLUDING SUMMARY

Nuclear graphite is very different from metals and metallic alloys in many aspects, which is precisely why it works so well as a neutron moderator in nuclear reactors. Contrary to metals and alloys, graphite benefits from the presence of porosity because pores are the internal buffer able to absorb the crystallite expansion after neutron bombardment, which would otherwise increase dimensional changes of graphite components and severely damage their structure. However, porosity may also act as a conduit for oxidants transport into the graphite body, which is detrimental for oxidation resistance. Because graphite is a high-purity carbon material, metal impurities at extremely low concentrations (e.g., in ppm range) cannot catalytically enhance oxidation reactions. Reactions between carbon and O_2 (and possibly H_2O or CO_2) are described globally by very few reaction routes leading to gas products such as CO_2 and CO (and possibly H_2). Upon closer examination, the oxidation mechanism is complicated by topological differences between various arrangements of C atoms in the graphite crystal, which determine differences between their reactivity at various positions in the graphite structure. Therefore, C atoms at edge sites in graphene structures are much more reactive than the much more numerous C atoms at basal plane positions. Only atoms belonging to the ASA may acquire sufficient reactivity for reaction with oxidants. The RSA, which is that fraction of ASA containing C atoms that actually react with the oxidant, is a small and variable fraction of the TSA, which is measured by the BET method.

Another complication is that chemical reactions can occur only at positions in the open pore system that can be accessed by the oxidant species through a long and tortuous diffusion path. Temperature acts differently on chemical reactions and oxidant diffusion. Depending on which of these processes is slower, the general behavior will be chemical (or kinetic) control (Regime 1) at lower temperatures, and in-pore diffusion control (Regime 2) at higher temperatures. The transition between these regimes is continuous, and it additionally depends on air flow rate. The graphite component's size is also important because it controls how far inward from the exposed surface the oxidant species can diffuse before being consumed by rapid chemical reactions. Thus, a gradient of oxidant concentrations develops under the surface, which determines an inverse gradient of local graphite densities and of associated material properties (e.g., mechanical, thermal). The progress of oxidation, in time and in space, depends on many factors, both intrinsic (specific to graphite grades) and extrinsic (depending by external conditions). The picture becomes even more complicated by the fact that local graphite properties evolve (degrade) in the near-surface zones of active oxidation. With that degradation, prediction of oxidation effects on graphite properties (dimensions, local density, mechanical and thermal properties) is reduced, in mathematical language, to solving a multivariable system of differential equations with boundary conditions specific to each situation.

Oxidation is essentially an interaction between the solid graphite phase and a surrounding gas phase. In accident conditions, the changes in temperature, composition, and hydrodynamic properties of the gas phase are ultimately those that control **WHERE, WHEN,** and **HOW MUCH OXIDATION will occur**. All safety analyses of reactor behavior in postulated accident conditions have to integrate graphite oxidation models with thermal-hydraulic codes, which creates another complication. The accuracy of such simulations cannot exceed the precision of results returned by the oxidation models. The models are only as good as the raw data, hypotheses, equations, and materials constants entered into them.

Almost eight decades have passed since graphite was first used as neutron moderator in Fermi's first graphite pile reactor is a long time, during which many grades of graphites have been produced, tailored, characterized, tested, and qualified for use as HTR in-core components. Some old grades (e.g., H-451, PGX), although qualified for use, were never fabricated into components because of changes in priorities regarding nuclear energy or because their raw source materials became unavailable. Newer grades (e.g., NBG-18, NBG-17, PCEA, 2114) still wait for "their reactor" to be fully designed, approved, and built. IG-110 is arguably the only grade that has been around for decades and has been the subject of many studies,

especially by researchers in Japan. The studies performed on IG-110, including many oxidation studies completed with properties changes and simulation and modeling activities, constitute a rich database available to designers. No other nuclear graphite grades that were studied in the past are still available, and modern grades (among them NBG-18 and PCEA) do not have the benefit of a long history of study.

Significant progress has been made over the past several decades of increasing graphite oxidation knowledge. Graphite structure is now better characterized, and its effect on the oxidation behavior of various graphite grades is better understood. A vast body of raw experimental data on graphite oxidation at different conditions has been accumulated, and it has already led to rationalization of observed differences between graphite grades and discovery of common trends in degradation of properties. The range of experimental temperatures for oxidation measurements has been extended toward the maximum range tolerated by the fuel. Now, the oxidation effects are better understood to be local, and the properties changes in a narrow subsurface region are easier to locate and observe. The density profile in the oxidized zone has been experimentally characterized in multiple studies and simulated by various oxidation models. The correlation between oxidant penetration depth (and profile) and the local variation of mechanical properties (compression and tensile strength, Young's modulus) has been observed for graphite grades, and some general trends have been proposed.

The overall trends in graphite research support optimistic conclusions. Highly pure, highly crystalline, highly densified nuclear graphite cannot undergo self-supported combustion, like low-quality, porous, impure charcoals. However, graphite is oxidizable if not properly protected. During normal operation in HTGRs, graphite components will be oxidized continuously but extremely slowly by trace concentrations of oxidizing impurities (mostly H_2O) in the helium coolant. However, because of extremely low concentrations and very slow oxidation rates, over several decades of reactor's operation, humidity traces will penetrate and oxidize only a few millimeters from the exposed surfaces, where the local weight loss will be less than 1%. This conclusion is of course conditioned by the strict control of helium impurities within the prescribed parameters for normal operating conditions.

On the other hand, exposure of core graphite components to air or steam ingress would trigger off-normal events, which may have serious or more severe consequences. Such evolutions are classified as either AEs with low probability or DBEs with extremely low probability. In AE scenarios, if limited air or water intrusion is quickly stopped along with other safety actions being taken, oxidation of graphite components is expected to be limited at the most exposed sites in the reactor. DBEs, which are more concerning, may affect larger regions in the reactor, causing more graphite oxidation, with possible structural degradation and radiologic consequences. Because there is very limited experimental information on such events, the understanding is based on model simulations, which may occasionally be validated by direct experiments, if available. Computer analysis and successful simulations of experiments (such as NACOK and others) indicates that various postulated accident scenarios can be accurately modeled even by early graphite oxidation models and engineering correlations. With a better understanding of oxidation behavior and development of more sophisticated simulation models integrated with the latest computer codes, prediction of low-probability off-normal events will reach higher levels of confidence. These improvements are the key for development of safer reactor designs for modular gas-cooled reactors.

Safety concerns are a crucial component regarding acceptance of nuclear energy. Past nuclear reactor accidents from earlier generations of nuclear plants may still influence hesitant positions toward nuclear energy as a safe and clean alternative to fossil fuels-based energy production. Informed scientists, engineers, regulators, and policymakers can help contribute to education on the safety features of Generation IV nuclear reactors, of which HTGRs and MHTGRs have been selected for development and future deployment.

9. REFERENCES

[1] ASTM D7219, Standard specification for isotropic and near-isotropic nuclear graphite, ASTM International.

[2] W. Windes, G. Strydom, R. Smith, J. Kane, Role of nuclear grade graphite in controlling oxidation in modular HTGRs, INL/EXT-14-31720, Idaho National Laboratory (2014).

[3] ASTM D7301-21, Standard specification for nuclear graphite suitable for components subjected to low neutron irradiation dose, ASTM International.

[4] P. L. Walker, F. Propp, L. G. Austin, Gas reactions of carbon, *Advances in Catalysis,* **11** (1959) 134–221.

[5] G. A. Roush, The manufacture of carbon electrodes, *Industrial & Engineering Chemistry*, **1** (1909) 286–295.

[6] C. L. Mantell, The technology of carbon electrode industry, *Chemical and Metallurgical Engineering*, **27** (1922) 3.

[7] R. Nightingale, *Graphite in Nuclear Industry*, Academic Press, New York, and London, 1962.

[8] S. Ragan, H. Marsh, Science and technology of graphite manufacture, *Journal of Materials Science*, **18** (1983) 3161–3176.

[9] T. R. Hupp, I. C. Lewis, J. M. Criscione, R. L. Reddy, C. F. Fulgenzi, D. J. Page, F. F. Fisher, A. J. Dzermejko, J. B. Hedge, Graphite, artificial, in *Kirk-Othmer Encyclopedia of Chemical Technology*, Wiley (2000).

[10] T. D. Burchell, Graphite: Properties and Characteristics, in *Comprehensive Nuclear Materials*, eds. T. R. Allen, R. E. Stoller, S. Yamanaka, Elsevier (2011), Chapter 2, 285–305.

[11] B. J. Marsden, *Nuclear graphite for high temperature reactors*, AEA Technology, Risley, Warrington (2001).

[12] T. Burchell, S. Nunn, J Strizak, M. Williams, AGC-1 sister specimen testing data report, ORNL/TM-2009/025.

[13] H. McCoy, R. L. Beatty, W. H. Cook, R. E. Gehlbach, C. R. Kennedy, J. W. Koger, A. P. Litman, C. E. Sessions, J. R. Weir, New developments in materials for molten-salt reactors, *Nuclear Applications and Technology*, **8** (1970) 156–169.

[14] C. I. Contescu, T. Guldan, P. Wang, T. D. Burchell, The effect of microstructure on air oxidation resistance of nuclear graphite, *Carbon*, **50** (2012) 3354–3366.

[15] ASTM D8075-16 (Reapproved 2021), Standard guide for categorizing of microstructural and microtextural features observed in optical micrographs of graphite, ASTM International.

[16] J. Kane, C. Kartik, D. P. Butt, W. E. Windes, R. Ubic, Microstructural characterization and pore structure analysis of nuclear graphite, *Journal of Nuclear Materials*, **415** (2011) 189–1972.

[17] N. C. Gallego, J. D. Arregui-Mena, C. I. Contescu, Probing basal planes and edge sites in polygranular nuclear graphite by gas adsorption: Estimation of active surface area, *Carbon,* **179** (2021) 633–645

[18] ASTM C559-16 (Reapproved 2020), Standard test method for bulk density by physical measurements of manufactured carbon and graphite articles, ASTM International.

[19] ASTM B923-21, Standard test method for metal powder skeletal density by helium or nitrogen pycnometry, ASTM International.

[20] ASTM D4284-12, Standard test method for determining pore volume distribution of catalysts by mercury intrusion porosimetry, ASTM International.

[21] R. Krishna, A. N. Jones, B. J. Marsden, Gamma radiation effects on nuclear reactor grades graphite, *23rd International Conference on Structural Mechanics in Reactor Technology,* SMiRT-23, Div. IV, paper 157, Manchester, UK, August 10–14 (2015).

[22] Z. Xu, L. Liu, Y. Huang, Y. Sun, X. Wu, J. Li, Graphitization of polyacrylonitrile carbon fibers and graphite irradiated by γ rays, *Materials Letters*, **63** (2009) 1814–1816.

[23] C. Goodwin, A. Barkratt, M. Al-Sheikhly, On the mechanism of the interactions of neutrons and gamma radiation with nuclear graphite - Implications to HTGRs, *Radiation Physics and Chemistry,* **97** (2014) 38–47.

[24] T. Tanabe, S. Muto, Y. Gotoh, K. Niwase, Reduction of the crystalline size of graphite by neutron irradiation, *Journal of Nuclear Materials,* **175** (1990) 258–261.

[25] R. H. Telling, M. I. Heggie, Radiation defects in graphite, *Philosophical Magazine*, **87** (2007) 4797–4846.

[26] B. J. Marsden, M. Haverty, W. Bodel, G. N. Hall, A. N. Jones, P. M. Mummery, M. Treifi, Dimensional change, irradiation creep and thermal/mechanical property changes in nuclear graphite, *International Materials Review*, **61** (2016) 155–182.

[27] T. Tanabe, T. Maruyana, M. Iseki, K. Niwase, H. Atsumi, Radiation damage of graphite: degradation of material parameters and defect structures, *Fusion Engineering and Design*, **29** (1995) 428–434.

[28] B. T. Kelly, T. D. Burchell, Structure-related property changes in polycrystalline graphite under neutron irradiation, *Carbon,* **32** (1994) 499–505.

[29] R. E. Dahl, Oxidation of graphite under high temperature reactor conditions, HW-68493, Hanford Atomic Products Operation (1961).

[30] A Blanchard, The thermal oxidation of graphite, in *Irradiation damage in graphite due to fast neutrons in fission and fusion systems*, IAEA-TECDOC-1154, International Atomic Energy Agency (2000).

[31] H.-K. Hinssen, K. Kuhn, E. Moormann, B. Schlögl, M. Fechter, M. Mitchell, Oxidation experiments and theoretical examinations of graphite materials relevant for the PBMR, *Nuclear Engineering and Design*, **238** (2008) 3018–3025.

[32] C. Velasquez, G. Hightower, R. Richards, The oxidation of H-451 graphite by steam. Part 1: Reaction kinetics, GA-A14951, General Atomics Company (1978).

[33] C. I. Contescu, R. W. Mee, Y. Lee, J. D. Arregui-Mena, N. C. Gallego, T. D. Burchell, J. J. Kane, W. E. Windes, Beyond the classical kinetic model for chronic graphite oxidation by moisture in high temperature gas-cooled reactors, *Carbon* **127** (2018) 158–169.

[34] X. Yu, L. Brissonneau, C. Bourdeloie, S. Yu, The modeling of graphite oxidation behavior for HTGR fuel coolant channels under normal operating conditions, *Nuclear Engineering and Design*, **238** (2008) 2230–223.

[35] C. I. Contescu, R. W. Mee, P. Wang, A. V. Romanova, T. D. Burchell, Oxidation of PCEA graphite by low water concentrations in helium, *Journal of Nuclear Materials*, **453** (2014) 225–232.

[36] Y. J. Cho, K. Lu, Water vapor oxidation behavior of nuclear graphite IG-110 for a postulated accident scenario in high temperature gas-cooled reactors, *Carbon,* **164** (2020) 251–260.

[37] A. K. Galway, M. E. Brown, Application of the Arrhenius equation to solid state kinetics: Can this be justified?, *Thermochimica Acta*, **386** (2002) 91–98.

[38] C. I. Contescu, Oxidation rate data measured according to ASTM D7542 (unpublished), Oak Ridge National Laboratory (2008 and 2011).

[39] S. K. Bhatia, D. D. Perlmutter, A random pore model for fluid–solid reactions: I Isothermal, kinetic control, *AIChE Journal,* **26** (1980) 379–386.

[40] J.-L. Su, D. D. Perlmutter, Effect of pore structure on char oxidation kinetics, *AIChE Journal,* **31** (1985) 973–981.

[41] R. P. Wichner, S. J. Ball, Potential damage to gas cooled graphite reactors due to severe accidents, ORNL/TM-13661, Oak Ridge National Laboratory (1999).

[42] E. L. Fuller, J. M. Okoh, Kinetics and mechanism of the reaction of air with nuclear grade graphites: IG-110, *Journal of Nuclear Materials,* **240** (1997) 241–250.

[43] M. S. El-Genk, C. I. Contescu, J.-M. P. Tournier, Comparison of oxidation model predictions with gasification data of IG-110, IG-430 and NBG-25 nuclear graphite, *Journal of Nuclear Materials,* **420** (2012) 141–158.

[44] W. Xu, S. Lei, Y. Zheng, Transient analysis of nuclear graphite oxidation for high temperature gas cooled reactor, *Nuclear Engineering and Design,* **306** (2016) 138–144.

[45] X. Luo, X. Yu, S. Yu, J.-C. Robin, Analysis of graphite gasification by water vapor at different conversions, *Nuclear Engineering and Design,* **273** (2014) 68–74.

[46] R. M. Paul, Application of a three-dimensional random pore model for thermal oxidation of synthetic graphite, *Journal of Nuclear Materials,* **543** (2021) 152589.

[47] R. M. Paul, J. E. Morral, A 3D random pore model for the oxidation of graphite with closed porosity, *Journal of Nuclear Materials,* **509** (2018) 425–434.

[48] R. M. Paul, J. E. Morral, A 3D random pore model for the oxidation of graphite with open porosity, *Journal of Nuclear Materials,* **499** (2018) 344–352.

[49] R. M. Paul, J. D. Arregui-Mena, C.I. Contescu, N. C Gallego, Effect of microstructure and temperature on nuclear graphite oxidation using the 3D random pore model, *Carbon*, **191** (2022) 132-145.

[50] ASTM D7542-21, Standard test method for air oxidation of carbon and graphite in the kinetic regime, ASTM International.

[51] E. S. Kim, K. W. Lee, H. C. No, Analysis of geometrical effects on graphite oxidation through measurement of internal surface area, *Journal of Nuclear Materials,* **348** (2006) 174–180.

[52] C. I. Contescu, S. Azad, D. Miller, M. J. Lance, F. S. Baker, T. D. Burchell, Practical aspects for characterizing air oxidation of graphite, *Journal of Nuclear Materials*, **381** (2008) 15–24.

[53] S.-H. Chi, G. C. Kim, Effects of air flow rate on the oxidation of NBG-18 and NBG-25 nuclear graphite, *Journal of Nuclear Materials*, **491** (2017) 34–42.

[54] X. Luo, J.-C. Robin, S. Yu, Effect of temperature on graphite oxidation behavior, *Nuclear Engineering and Design*, **227** (2004) 273–280.

[55] J. J. Lee, T. K. Ghosh, S. K. Loyalka, Oxidation rate of nuclear-grade graphite IG-110 in the kinetic regime for VHTR air ingress accident scenarios, *Journal of Nuclear Materials*, **446** (2014) 38–48.

[56] E. S. Kim, J. C. No, Experimental study on the oxidation of nuclear graphite and development of an oxidation model, *Journal of Nuclear Materials*, **349** (2006) 182–194.

[57] R. E. Smith, J. J. Kane, W. E. Windes, Determining the acute oxidation behavior of several nuclear graphite grades, *Journal of Nuclear Materials*, **545** (2021) 152648.

[58] ASTM C1179-15, Standard test method for oxidation mass loss of manufactured carbon and graphite materials in air, ASTM International.

[59] W. Lu, X. Li, X. Wu, L. Sun, Z. Li, Investigation on the oxidation behavior and multi-step reaction mechanism of nuclear graphite SNG742, *Journal of Nuclear Science and Technology*, **57** (2020) 263–275.

[60] C Wang, Experimental and numerical investigation of graphite-steam oxidation for HTGRs, PhD dissertation, University of Michigan (2021).

[61] R. Moormann, Phenomenology of graphite burning in massive air ingress accidents, Proceedings *3rd International Topical Meeting on High Temperature Reactor Technology* (HTR2006) Johannesburg, South Africa (2006).

[62] D. G. Schweitzer, et al., Oxidation and heat transfer studies in graphite channels (I–IV), *Nuclear Science and Engineering*, **12**, 39–45, 40–50, 51–58, 59–62 (1962).

[63] Y. Zheng, M. M. Stempniewicz, Investigation of NACOK air ingress experiment using different system analysis codes, *Nuclear Engineering and Design*, **251** (2012) 423–432.

[64] B. Castle, NGNP reactor coolant chemistry control study, INL/EXT-10-19533, Idaho National Laboratory (2010).

[65] C. Contescu, R. Mee, Status of chronic oxidation studies of graphite, ORNL/TM-2016/195, Oak Ridge National Laboratory (2016).

[66] T. J. Clark, R. E. Woodley, D. R. de Halas, Gas-graphite systems, in *Nuclear Graphite*, ed. R. E. Nightingale, Academic Press (1962), Chapter 14.

[67] J. Gadsby, C. N. Hinshelwood, K. W. Sykes, The kinetics of the reactions of the steam-carbon system, *Proceedings of Royal Society (London)*, **A187** (1946) 129–151.

[68] M. B. Richards, Reaction of nuclear-grade graphite with low concentrations of steam in the helium coolant of an MHTGR, *Energy*, **15** (1990) 729–739.

[69] M. Richards, React-Compact: A computer code for modeling graphite corrosion and fuel hydrolysis, Proceedings *International Topical Meeting on High Temperature Reactor Technology* (HTR2016), Las Vegas, Nevada, November 6–10 (2016).

[70] Y. H. Cho, K. Lu, Water vapor oxidation behaviors of nuclear graphite IG-110 for a postulated accident scenario in high temperature gas-cooled reactors, *Carbon,* **164** (2020) 251–260.

[71] C. I. Contescu, T. D. Burchell, R. W. Mee, Kinetics of chronic oxidation of NBG-17 nuclear graphite by water vapor, ORNL/TM-2015/142, Oak Ridge National Laboratory (2015).

[72] C. I. Contescu, Y. Lee, R. W. Mee, Oxidation kinetics by water vapor of nuclear graphite grade 2114, ORNL/TM-2018/1057, Oak Ridge National Laboratory (2018).

[73] C. I. Contescu, T. D. Burchell, Water vapor transport in nuclear graphite, ORN/TM-2015/88, Oak Ridge National Laboratory (2015).

[74] R. P. Wichner, T. D. Burchell, C. I. Contescu, Penetration depth and transient oxidation of graphite by oxygen and water vapor, *Journal of Nuclear Materials*, **393** (2009) 518–521.

[75] R. P. Wichner, T. D. Burchell, C. I. Contescu, Note of graphite oxidation by oxygen and water, ONL/TM-2008/230, Oak Ridge National Laboratory (2008).

[76] C. I. Contescu, Validation of Wichner predictive model for chronic oxidation by moisture of nuclear graphite, ORNL/TM-2019/1306, Oak Ridge National Laboratory (2019).

[77] T. Gerczak, C. I. Contescu, J. J. Lee, R. Mee, A. Schumacher, J. Stempien, M. Trammell, Oxidation of matrix material in helium with varied moisture content, ORNL/TM-2019/1341, Oak Ridge National Laboratory (2019).

[78] C. Wang, X. Sun, E. N. Christensen, Multiphysics simulation of moisture-graphite oxidation in MHTGR, *Annals of Nuclear Energy*, **131** (2019) 483-495.

[79] J. Gadsby, F. J. Long, P. Sleightholm, K. W. Sykes, The mechanism of carbon dioxide–carbon reaction, *Proceedings of Royal Society* (London), **A193** (1948) 357–376.

[80] J. V. Best, W. J. Stephen, A. J. Wickham, Radiolytic graphite oxidation, *Progress in Nuclear Energy*, **16** (1985) 127–178.

[81] S. Brunauer, P. H. Emmett, E. Teller, Adsorption of gases in multimolecular layers, *Journal of American Carbon Society*, **60** (1938) 309–319.

[82] N. C. Gallego, J. D. Arregui-Mena, C. I. Contescu, Probing basal planes and edge sites in polygranular nuclear graphite by gas adsorption: Estimation of active surface area, *Carbon*, **179** (2021) 635–645.

[83] L. R. Radovic, P. L. Walker, R. G. Jenkins, Importance of carbon atoms active sites in the gasification of coal chars, *Fuel*, **62** (1983) 849–856.

[84] J. J. Kane, C. I. Contescu, R. E. Smith, G. Strydom, W. E. Windes, Understanding the reaction of nuclear graphite with molecular oxygen: Kinetics, transport, and structural evolution, *Journal of Nuclear Materials*, **493** (2017) 343–367.

[85] J. N. Ong, On the kinetics of oxidation of graphite, *Carbon,* **2** (1964) 281–297.

[86] T. Takeda, M. Hishida, Study on the passive safe technology for the prevention of air ingress during the primary-pipe rupture accident of HTGR, *Nuclear Engineering and Design*, **200** (2000) 251–259.

[87] S. J. Ball, Overview of modular HTGR safety characterization and postulated accident behavior licensing strategy, ORNL/TM-2014/187, Oak Ridge National Laboratory (2014).

[88] I.-H. Lo, A. Tzelepi, E. A. Patterson, T.-K. Yeh, A study of the relationship between microstructure and oxidation effects in nuclear graphite at very high temperatures, *Journal of Nuclear Materials*, **501** (2018) 361–370.

[89] I.-H. Lo, T.-K. Yeh, E. A. Patterson, A. Tzelepi, Comparison of oxidation behavior of nuclear graphite grades at very high temperatures, *Journal of Nuclear Materials*, **532** (2020) 152054.

[90] R. E. Helms, R. E. MacPherson, Summary report on the reaction of steam with large specimens of graphite for the experimental gas-cooled reactor, ORNL-TM-1430, Oak Ridge National Laboratory (1966).

[91] Preliminary Safety Information Document for the Standard MHTGR, DOE/HTGR-86-024, Stone and Webster Engineering Corp. (1986).

[92] Y. Zheng, L. Shi, Y. Wang, Water ingress analysis for the 200 MWe pebble-bed modular high temperature gas-cooled reactor, *Nuclear Engineering and Design*, **240** (2010) 3095–3107.

[93] R. E. Smith, J. J. Kane, W. E. Windes, Determining the acute oxidation behavior of several nuclear graphite grades, *Journal of Nuclear Materials*, **545** (2021) 152648.

[94] C. I. Contescu, Microstructure effect on air oxidation behavior of three nuclear grade graphite materials: NBG-18, PCEA, and IG-110, ORNL/TM-2011/324, Oak Ridge National Laboratory (2011).

[95] S.-H. Chi, G. C. Kim, Comparison of the oxidation rate and degree of graphitization of selected IG and NBG nuclear graphite grades, *Journal of Nuclear Materials*, **381** (2008) 9–14.

[96] W. Lu, X. Li, X. Wu, L. Sun, Z. Li, Investigation on the oxidation behavior and multi-step reaction mechanism of nuclear graphite SNG742, *Journal of Nuclear Science and Technology*, **57** (2020) 263–275.

[97] W.-H. Huang, S.-C. Tsai, C.-W. Yang, J.-J. Kai, The relationship between microstructure and oxidation effects of selected IG- and NBG-18 grade nuclear graphites, *Journal of Nuclear Materials*, **454** (2014) 149–158.

[98] X. Sun, Y. Dong, Y. Zhou, Z. Li, L. Shi, Y. Sun, Z. Zhang, Effect of reaction temperature and inlet oxidizing gas flow rate on IG-110 graphite oxidation used in HTR-PM, *Journal of Nuclear Science and Technology*, **54** (2017) 196–204.

[99] R. Yan, Y. Dong, Y. Zhou, X. Sun, Z. Li, Investigation of oxidation behaviors of nuclear graphite being developed and IG-110 based on gas analysis, *Journal of Nuclear Science and Technology*, **54** (2017) 1168–1177.

[100] J. J. Lee, T. K. Ghosh, S. K. Loyalka, Oxidation rate of nuclear-grade graphite NBG-18 in the kinetic regime for VHTR air ingress accident scenarios, *Journal of Nuclear Materials*, **438** (2013) 77–87.

[101] J. J. Lee, T. K. Ghosh, S. K. Loyalka, Comparison of NBG-18, NBG-17, IG-110 and IG-11 oxidation kinetics in air, *Journal of Nuclear Materials*, **500** (2018) 64–71.

[102] C. I. Contescu, T. Guldan, R. P. Wichner, T. Burchell, Oxidation resistance of NGNP graphite materials: Comparative study of NBG-18 and PCEA nuclear graphite materials, internal report, Oak Ridge National Laboratory (2008).

[103] C. I. Contescu, J. P. Strizak, T. R. Guldan, T. D. Burchell, Microstructure effect on air oxidation of nuclear graphite materials: NBG-18, PCEA, and IG-110, ORNL/TM-2011/324, Oak Ridge National Laboratory (2011).

[104] J. J. Kane, A. C. Matthews, W. D. Swank, W. E. Windes, Effects of air oxidation on the evolution of surface area within nuclear graphite and the contribution of macropores, *Carbon*, **199** (2020) 291–306.

[105] Z. Yanhua, S. Lei, W. Yan, Water ingress analysis for the 200 Mwe pebble-bed modular high temperature gas-cooled reactor, *Nuclear Engineering and Design*, **240** (2010) 3095–3107.

[106] F. B. Growcock, Advanced Reactor Safety Research Division, Quarterly Progress Report, July 1–September 30, 1980, NUREG/CR-1799, BNL-NUREG-51297, Brookhaven National Laboratory (1980).

[107] C. Contescu, T. Burchell, Status of diffusion-controlled graphite oxidation studies for high-temperature gas-cooled reactors, ORNL/TM-2012/598, Oak Ridge National Laboratory (2012).

[108] C. Contescu, J. P. Strizak, T. R. Guldan, T. D. Burchell, Effect of air oxidation on pore structure development and mechanical properties of nuclear graphite, ORNL/TM-2010/197, Oak Ridge National Laboratory (2010).

[109] C. Contescu, T. Burchell, Oxidation profiles and porosity development during oxidation of graphite in air, *10th International Nuclear Graphite Specialists Meeting* (INGSM), Yellowstone, September 30, (2009).

[110] S. Yoda, M. Eto, K. Tanaka, T. Oku, Effect of oxidation on compressive deformation behavior of nuclear-grade isotropic graphite, *Carbon*, **23** (1985) 33–38.

[111] A. C. Collins, H. G. Masterson, P. P. Jennings, The effect of oxidation on the compressive strength of graphite, *Journal of Nuclear Materials*, **15** (1965) 135–136.

[112] M. Eto, F. B. Growcock, Effect of oxidizing environment on the strength and oxidation kinetics of HTGR graphites, Part 1: Reactivity and strength loss of H451, PGX and IG-11 graphites, NUREG/CR-24008, BNL-NUREG-51493, Brookhaven National Laboratory (1981).

[113] C. Velasquez, W. Johnson, G. Hightower, R. Burnette, The effect of steam oxidation on the strength and elastic modulus of graphite H-451, GA-A14657, UC-77, General Atomics Company (1977).

[114] M. Eto, T. Oku, T. Konishi, High temperature Young's modulus of a fine-grained nuclear graphite oxidized or prestressed to various levels, *Carbon*, **29** (1991) 11–21.

[115] M. Eto, T. Kurosawa, S. Nomura, H. Imai, Evaluation of the oxidation behavior and strength of the graphite components in the VHTR (I): Normal operation condition, JAERI-M 87-056, Japan Atomic Energy Research Institute (1987).

[116] M. Eto, F. B. Growcock, Effect of oxidizing environment on the strength of H451, PGX and IG-11 graphites, *Carbon*, **21** (1983) 135–147.

[117] S. Yoda, M. Eto, T. Oku, T. Sogabe, Effects of oxidation on tensile and compressive deformation behavior for nuclear grade isotropic graphite, *Conference Internationale sur les Carbones* (Carbone 84), Bordeaux, France, July 2–6 (1984).

[118] S. Sato, K. Hirakawa, A. Kurumada, S. Kimura, E. Yasuda, Degradation of fracture mechanics properties of reactor graphite due to burn-off, *Nuclear Engineering and Design*, **118** (1990) 227–241.

[119] A. C. Matthews, J. J. Kane, W. D. Swank, W. E. Windes, Nuclear graphite strength degradation under varying oxidizing conditions, *Nuclear Engineering and Design*, **379** (2021) 111245.

[120] F. P. Knudsen, Dependence of mechanical strength of brittle polycrystalline specimens on porosity and grain size, *Journal of American Ceramic Society*, **42** (1959) 376–387.

[121] J. L. Wood, R. C. Bradt, P. L. Walker, Oxidation effects on toughness and slow crack growth in polycrystalline graphite, *Carbon*, **18** (1980) 179–189.

[122] R. W. Rice, Comparison of physical property–porosity behavior with minimum solid area models, *Journal of Materials Science*, **31** (1996) 1509–1528.

[123] E. S. Kim, C. H. Oh, H. C. No, B. J. Kim, Estimation of graphite density and mechanical strength of VHTR during air-ingress accident, INL/CON-07-12640, *12th International Topical Meeting on Nuclear Reactor Thermal Hydraulics* (NURETH-12), Pittsburgh, Pennsylvania, September 30–October 4 (2007).

[124] X. Zhou, C. I. Contescu, X. Zhao, Z. Lu, J. Zhang, Y. Katoh, Y. Wang, B. Liu, Y. Tang, C. Tang, Oxidation behavior of matrix graphite and its effect on compressive strength, *Science and Technology of Nuclear Installations* (2017) 4275375.

[125] B. H. Park, H. C. No, Strength degradation of oxidized graphite support column in VHTR, *Journal of Nuclear Science and Technology*, **47** (2010) 998–1004.

[126] J. E. Brocklerhurst, R. O. Brown, K. E. Gilchrist, Y. Y. Labaton, The effect of radiolytic oxidation on the physical properties of graphite, *Journal of Nuclear Materials*, **35** (1970) 183–194.

[127] B. T. Kelly, P. A. V. Johnson, P. Schofield, J. E. Broklerhurst, M. Birch, UKAEA Northern Division studies of the radiolytic oxidation of graphite in carbon dioxide, *Carbon*, **21** (1983) 441–449.

[128] M. Metcalfe, Everything changes but its color: The behavior of graphite in a nuclear environment, *4th BIT World Congress of Advanced Materials*, Chongqing Yuelai International Conference Center, Chongqing, China, May 27–29 (2015).

[129] S. Sato, K. Hirahawa, A. Kurumada, S. Kimura, E. Yasuda, Degradation of fracture mechanics properties of reactor graphite due to burn-off, *Nuclear Engineering and Design*, **118** (1990) 227–241.

[130] M. Eto, T. Oku, T. Konishi, High temperature Young's modulus of a fine-grained nuclear graphite oxidized or prestressed to various levels, *Carbon*, **29** (1991) 11–21.

[131] L. R. Olasov, F. W. Zeng, J. B. Spicer, N. C. Gallego, C. I. Contescu, Modeling the effects of oxidation-induced porosity on the elastic moduli of nuclear graphites, *Carbon*, **141** (2019) 304–315.

[132] M. S. El-Genk, J.-M. Tournier, Sherwood number correlation for nuclear graphite gasification at high temperature, *Progress in Nuclear Energy*, **62** (2013) 26–36.

[133] P. Hawtin, J. A. Gibson, R. Murdoch, J. B. Lewis, The effect of diffusion and bulk gas flow on the thermal oxidation of nuclear graphite; I Temperatures below 500 °C, *Carbon*, **2** (1964) 299–309.

[134] X. Wei, S. Lei, Z. Yanhua, Transient analysis of nuclear graphite oxidation for high temperature gas cooled reactor, *Nuclear Engineering and Design*, **306** (2016) 138–144.

[135] J. Skalyo, L. G. Epel, S. Sastre, An analysis of the methods utilized in OXIDE-3, BNL-NUREG-50810, Brookhaven National Laboratory (1978).

[136] F. Gelbard, Graphite oxidation modeling for application in MELCOR, SAND2008-7852, Sandia National Laboratories (2008).

[137] R. L. Moore, C. H. Oh, B. J. Merrill, D. A. Petti, Studies on air ingress for pebble bed reactors, *Proceedings of the Conference on High Temperature Reactors* (HTTR2002), Vienna, Austria, April 22–24 (2002).

[138] M. S. El-Genk, J.-M. Tournier, Development and validation of a graphite oxidation model, *Journal of Nuclear Materials*, **411** (2011) 193–207.

[139] M. S. El-Genk, J.-M. Tournier, Comparison of oxidation model predictions with gasification data of IG-110, IG-430 and NBG-25 nuclear graphite, *Journal of Nuclear Materials*, **420** (2012) 141–158.

[140] M. S. El-Genk, J.-M. Tournier, Comparison of gasification kinetics parameters of different types of nuclear graphite, *Proceedings International Congress on Advances in Nuclear power Plants* (ICAPP'12), Chicago, Illinois, paper 12023, June 24–28 (2012).

[141] M. S. El-Genk, J.-M. Tournier, B. Travis, Graphite oxidation simulation in HTR accident conditions, ISNPS-UNM-1-2012, Institute for Space and Nuclear Power Studies (2012).

[142] M. S. El-Genk, J.-M. Tournier, C. I. Contescu, Chemical kinetics parameters and model validation for the gasification of PCEA nuclear graphite, *Journal of Nuclear Materials*, **444** (2014) 112–128.

[143] M. S. El-Genk, J.-M. Tournier, Transient gasification in an NBG-18 coolant channel of a VHTR prismatic fuel element, *Progress in Nuclear Energy*, **64** (2013) 16–30.

[144] P. Hawtin, J. A. Gibson, The effect of diffusion and bulk gas flow on the thermal oxidation of nuclear graphite. II Diffusional effects in graphite at high temperatures, *Carbon,* **4** (1966) 489–500.

[145] P. Hawtin, R. A. Huber, The effects of non-uniform burn off on the kinetics of oxidation of large tubular specimens of graphite, *Carbon,* **6** (1968) 887–899.

[146] E. S. Kim, H. C. No, B. J. Kim, C. H. Oh, Estimation of graphite density and mechanical strength variation of VHTR during air-ingress accident, *Nuclear Engineering and Design,* **238** (2008) 837–847.

[147] C. H. Oh, C. Davis, L. Siefkin, R. Moore, H. C. No, J. Kim, G. C. Park, J. C. Lee, W. R. Martin, Development of safety analysis codes and experimental validation for a very high temperature gas-cooled reactor, Final report, INL/EXT-06-01362, Idaho National Laboratory (2006).

[148] E. S. Kim, H. C. No, Experimental study on the reaction between nuclear graphite IG-110 and carbon dioxide, *Journal of Nuclear Materials*, **350** (2006) 96–100.

[149] J. J. Kane, C. Kartik, R. Ubic, W. E. Windes, D. P. Butt, An oxygen transfer model for high purity graphite oxidation, *Carbon*, **59** (2013) 49–64.

[150] L. G. Giberson, J. P. Walker, Reaction of nuclear grade graphite with water vapor. I. Effect of hydrogen and water vapor partial pressures, *Carbon*, **2** (1966) 521–525.

[151] R. H. Hurt, J. M. Calo, Semi-global intrinsic kinetics for char combustion modelling, *Combustion and Flame*, **125** (2001) 1138–1149.

[152] R. H. Hurt, B. S. Haynes, On the origin of power-law kinetics in carbon oxidation, *Proceedings of Combustion Institute* **30** (2005) 2161–2168.

[153] M. M. Stempniewicz, Correlation for steam-graphite reaction, *Nuclear Engineering and Design*, **280** (2014) 285–293.

[154] H. C. No, E. S. Kim, H. S. Lim, Multidimensional multicomponent mixture air ingress analysis and air ingress experiment in an HTGR, *Sixth International Topical Meeting on Nuclear Thermal Hydraulics, Operation and Safety* (NUTHOS-6), paper KN-01, October 4–8 (2004).

[155] H. Haque, RAPHAEL ST WP3: Air Ingress Experiment NACOK. Pre-calculation: Input data, assumptions and preliminary results, Technical Note, Areva (2008).

[156] J. Roes, Experimentelle Untersuchungen zur Graphitkorrosion und Aerosolentstehung beim Lufteinbruch in das Core eines Kugelhaufen Hochtemperaturreaktors, Jul-2956, KfA (1994) (in German).

[157] R. L. Moore, C. H. Oh, B. J. Merrill, D. A. Petti, Studies on air ingress for pebble bed reactors, HTTR2002, *Proceedings of the Conference on High Temperature Reactors* (HTR2002), Vienna, Austria, April 22–24 (2002).

[158] W. Xu, Y. Zheng, L. Shi, P. Liu, Oxidation analyses of massive air ingress accident of HTR-PM, *Science and Technology of Nuclear Installations* (2016) 6419124.

[159] C. H. Oh, E. S. Kim, H. C. No, N. Z. Cho, Final report on experimental validation of stratified flow phenomena, graphite oxidation, and mitigation strategies of air ingress accidents, INL/EXT-10-20759, Idaho National Laboratory (2010).

[160] X. Wei, S. Lei, Z. Yanhua, Transient analysis of nuclear graphite oxidation for high temperature gas cooled reactor, *Nuclear Engineering and Design*, **306** (2016) 138–144.

[161] S. S. Penner, M. B. Richards, Oxidation of nuclear-reactor-grade graphite, *Energy*, **13** (1988) 461–468.

[162] S. W. Webb, Gas Transport Mechanisms, in *Gas Transport in Porous Media*, eds. C. Ho. S. Webb, Springer (2006), Chapter 2, pp. 5–26.

[163] R. J. Millington, J. M. Quirk, Permeability of porous solids, *Transactions of Faraday Society*, **57** (1961) 1200–1207.

[164] J. J. Kane, A. C. Matthews, C. J. Orme, C. I. Contescu, W. D. Swank, W. E. Windes, Effective gaseous diffusion coefficients of select ultra-fine and medium grain nuclear graphite, *Carbon*, **136** (2018) 369–379.

[165] G. F. Hewitt, K. W. Sharratt, The diffusion of oxygen in nitrogen in the pores of graphite: Preliminary results on the effect of oxidation on diffusivity, AERE–M 1080, Atomic Energy Research Establishment (1962).

[166] G. F. Hewitt, R. Murdoch, The role of in-pore mass transport resistance in the reaction of porous solids with gases, *Chemical Engineering Science*, **19** (1964) 819–834.

[167] G. F. Hewitt, M. J. C. Moore, K. W. Sharratt, The diffusion of oxygen in nitrogen in the pores of graphite: The effect of oxidation on diffusivity and permeability, *Carbon*, **8** (1970) 271–282.

[168] J. D. Clark, P. J. Robinson, Diffusion studies of porous materials. Part 2: Effects of thermal and radiolytic oxidation on pore structure of a "high-reactivity" nuclear graphite, *Journal of Materials Science*, **17** (1982) 2649–2656.

[169] M. Ogawa, Mass transfer of mixed gas flow crossing a high temperature graphite cylinder with chemical reactions and in-pore diffusion, *International Journal of Heat and Mass Transfer*, **30** (1987) 1017–1026.

[170] R. Moormann, H.-K. Hinssen, Advanced graphite oxidation models, in *Basic Studies in the Field of High-temperature Engineering*, 2nd Information Exchange Meeting, Paris, France, October 10–12 (2001) 243–254.

[171] H. Ohashi, H. Sato, Y. Tachibana, K. Kunitomi, M. Ogawa, Feasibility study on naturally safe HTGR (NSHTGR) for air ingress accident, *Nuclear Engineering and Design*, **271** (2014) 537–544.

[172] J. Liu, L. Dong, C. Wang, T. Liang, W. Lai, First principles study of oxidation behavior of irradiated graphite, *Nuclear Instruments and Methods in Physics Research*, **B352** (2015) 160–166.

[173] F. F. Zherdev, I. E. Komissarov, B. A. Gurovich, V. M. Markushev, The effect of neutron irradiation on the reactor graphite corrosion kinetics, *Journal of Nuclear Materials*, **189** (1992) 333–342.

[174] F. F. Zherdev, I. E. Komissarov, On the increase of the oxidation rate of irradiated reactor graphite with decreasing temperature, *Journal of Nuclear Materials*, **209** (1994) 47–51.

[175] D. G. Schweitzer, E. M. Singer, Oxidation rates of alternately irradiated and annealed graphite, *Journal of Nuclear Materials*, **16** (1965) 220–226.

[176] ASTM D7775-16, Standard guide for measurements on small graphite specimens, ASTM International.

[177] R. W. Smith, Comparison of oxidation performance of graphite samples in TGA versus vertical furnace, INL/EXT-19-54584, Idaho National Laboratory (2019).

[178] ASTM C695-21, Standard test method for compressive strength of carbon and graphite, ASTM International.

[179] ASTM C651-20, Standard test method for flexural strength of manufactured carbon and graphite articles using four-point loading at room temperature, ASTM International.

[180] ASTM D7972-14 (Reapproved 2020), Standard test method for flexural strength of manufacture carbon and graphite articles using three-point loading at room temperature, ASTM International.

[181] ASTM C747-16, Standard test method for moduli of elasticity and fundamental frequencies of carbon and graphite materials by sonic resonance, ASTM International.

[182] ASTM C749-15 (Reapproved 2020), Standard test method for tensile stress-strain of carbon and graphite, ASTM International.

[183] ASTM D8289-20 Standard test method for tensile strength estimate by disc compression of manufactured graphite, ASTM International.

[184] ASTM E228-17, Standard test method for linear thermal expansion of solid materials with a push-rod dilatometer, ASTM International.

[185] ASTM C714-17, Standard test method for thermal diffusivity of carbon and graphite by thermal pulse method, ASTM International.